



Provided by the author(s) and University of Galway in accordance with publisher policies. Please cite the published version when available.

Title	Incremental elastic surface waves and static wrinkles
Author(s)	Gower, Artur Lewis
Publication Date	2015-10-06
Item record	http://hdl.handle.net/10379/5303

Downloaded 2024-04-23T16:14:11Z

Some rights reserved. For more information, please see the item record link above.



INCREMENTAL ELASTIC
SURFACE WAVES
AND
STATIC WRINKLES

PhD Thesis

by

Artur L Gower

Supervisor: Professor Michel Destrade

School of Mathematics, Statistics and Applied Mathematics
National University of Ireland, Galway

September 2015



Dedicated to my friends who are far away,

and specially to Nerv.

Abstract

This *article-based thesis* comprises a collection of four articles, each of which constitutes a chapter written and formatted in manuscript form. The general aim underlying these articles is to understand and predict how incremental elastic surface waves propagate or static wrinkles form on a deformed elastic substrate. The formation of these small-amplitude disturbances can be the end goal, such as in sending signals or creating functional coatings, or they can be used to measure and characterise the underlying elastic substrate. This thesis focuses on using surface waves or static wrinkles to characterise soft solids, such as biological tissues.

Contents

Acknowledgement	1
Introduction	3
References	9
1 Looking for M. Biot's wrinkles	13
1.1 Introduction	13
1.2 Methods	15
1.2.1 Theoretical	15
1.2.2 Experimental	18
1.3 Results	18
1.4 Discussion and Conclusion	19
References	25
2 Shear Instability in Skin Tissue	27
2.1 Introduction	27
2.2 Shear instability for a neo-Hookean layer with surface tension . . .	29
2.3 Shear instability of a fibre-reinforced skin tissue	34
2.4 Discussion and Conclusion	39
References	40
Appendix	41
3 Counter-intuitive results in acousto-elasticity	45
3.1 Introduction	45
3.2 Governing equations	48
3.2.1 Incremental motions	48
3.2.2 Deformed materials	49
3.3 Results for body waves	51
3.4 The matrix Riccati method for surface waves	54
3.5 Results for surface waves	57
3.6 Conclusion	58
References	60
4 Connecting the Material Parameters of Soft Fibre Reinforced Solids with the Formation of Surface Wrinkles.	63
4.1 Introduction	64

4.2	The Model	66
4.2.1	Theoretical Setup	66
4.2.2	Incremental Equations	68
4.3	Shear-Box Wrinkling	71
4.3.1	The Shear-box	71
4.3.2	The Riccati Method	72
4.3.3	Predictions	74
4.3.4	Asymptotics	77
4.4	Conclusion	78
	References	79
	Conclusion	83
	References	84

Acknowledgment

Doing a PhD is an odd thing. Most enter it full of misconceptions and I was no different. I believed that to get a PhD required making a ground-breaking discovery; one that I would ultimately achieve after being locked in a room alone for a few years. Luckily my supervisor, Michel Destrade, showed me a less mysterious way to conduct a PhD. So I truly wish to thank Michel Destrade for his invaluable advice, friendship and for accompanying me into a variety of exciting research projects!

I am thankful to all those whose collaboration and friendship during the past four years made this thesis possible. A probably incomplete set of people I wish to thank is below.

I must thank Pasquale Ciarletta for inviting me to Paris and for willingly joining me in the pursuit to describe residually stressed solids.

I am indebted to Ray Ogden for his support and collaboration, for inviting me to Glasgow and for his kindness.

My collaborators from Engineering: David Nolan, Patrick McGarry, Peter McHugh and Anna Bobel. Working in a multi-disciplinary team was a fantastic experience.

The efforts of Tom Shearer and Giuseppe Zurlo in spotting errors and improving this thesis were valuable and I am thankful.

To those who organise the OCCAM graduate modelling camp, for introducing me to industrial mathematics which has now become one of my main interests. And to all those that organise the European Study Groups with Industry (ESGI) which also inspired me.

A special thanks to my family for their unquestioning support, including my collaborator and brother Robert Gower. Molly Aitken, for her love and companionship.

The National University of Ireland, Galway, for the excellent facilities, clubs and societies which truly contribute to the quality of life of many. Especially to the Table Tennis club and the post-grads from the Riverside Terrapin for the laughs and friendship.

Finally, these past years would not have been possible if it were not for the financial support from the Irish Research Council, the Hardiman scholarship, NUI-Galway college of Science and the School of Mathematics.

Introduction

About this thesis

This *article-based thesis* comprises a collection of four articles, each of which constitutes a chapter written and formatted in manuscript form. The general aim underlying these articles is to understand and predict how incremental elastic surface waves propagate or static wrinkles form on a deformed elastic substrate.

Three of the articles [1-3] have been peer-reviewed and published in international scientific journals, including two upon invitation to contribute to special issues. One is currently under review [6]. For the four papers presented here, I contributed to the results and redaction either 100% when sole author [3] or in equal proportion when co-author [1,2,6].

I have also completed other written works, including two peer-reviewed journal articles [4,5] and two submitted manuscripts [7,8], but they fall under other themes and were not included here. Here is a list of my peer-reviewed publications so far,

1. P. Ciarletta, M. Destrade, A.L. Gower.
Shear instability in skin tissue,
Quarterly Journal of Mechanics and Applied Mathematics,
66 (2013) 273–288.
2. A.L. Gower, M. Destrade, R.W. Ogden.
Counter-intuitive results in acousto-elasticity,
Wave Motion,
Special Issue in Honour of V.I. Alshits [invited contribution],
50 (2013) 1218–1228.
3. A.L. Gower.
Connecting the material parameters of soft fibre-reinforced solids with the formation of surface wrinkles,
Journal of Engineering Mathematics,
Special Issue on Fiber-Reinforced Materials [invited contribution]
(2014) 1–13.
4. D.R. Nolan, A.L. Gower, M. Destrade, R.W. Ogden, J.P. McGarry.
A robust anisotropic hyperelastic formulation for the modelling of soft tissue,
Journal of the Mechanical Behavior of Biomedical Materials,
39 (2014) 48-60.

5. R.M. Gower, A.L. Gower.
High order reverse automatic differentiation with emphasis on the third order,
Mathematical Programming SERIES A,
(2014) 1–23.

Below is a list of manuscripts under review.

6. A.L. Gower, M. Destrade.
Looking for M. Biot’s wrinkles,
(submitted).
7. A.L. Gower, P. Ciarletta, M. Destrade (2015),
Initial Stress Symmetry and its Applications in Elasticity,
ArXiv preprint, arXiv:1506.05038,
(submitted).
8. P. Ciarletta, M. Destrade, A.L. Gower ,
On residual stresses and homeostasis: an elastic theory of functional adaptation in living matter,
(submitted).

Background

In the study of incremental motions and deformations, the small-amplitude disturbances can be the end goal, such as in sending signals (Campbell 2012) or creating functional coatings (Genzer and Groenewold 2006), or they can be used to measure and characterise the underlying elastic substrate. Either way, these disturbances are dependent on the properties of the elastic solid. The solids considered in this dissertation can sustain large strains, and for this reason the thesis opens with a discussion about nonlinear elasticity and its applications.

Suppose we wanted to predict the mechanical behaviour of a copper pipe. What theoretical framework would we use? It could be argued that the behaviour of the pipe is dictated by that of the individual copper atoms, of which there are about 10^{22} per gramme of copper (*Atomic weight of Copper* 2015). However, to then use Schrödinger’s equation in order to predict the forces and displacements occurring in one gramme of this pipe for 1 second would be computationally infeasible at present, the state of the art of quantum calculations involves just hundreds of atoms over nanoseconds (Atkins et al. 2009).

The appropriate theoretical approach to model our copper pipe depends on what we wish to predict. If we wish to know how much this pipe will bend, compress and expand in response to applied forces and moments, then calculating the movement of each atom is unnecessary. Instead, we can try to calculate the average (macroscopic) values of the stress, strain, mass density, etc.; this approach is called *Continuum Mechanics* (Tadmor et al. 2012). Even for systems where the fundamental parts are much larger than atoms it can be useful, and even necessary, to resort to the continuum approach, such as when predicting the motion of sand

dunes (Sauermann et al. 2001) and the flow of traffic in big cities (Wong 1998) for example.

A good portion of the continuum around us is held together by solid materials. The main discerning feature of solids is their response to applied forces and moments, but there is no one-size-fits-all model in solid mechanics. In fact, there is not even a clear dividing line between what we call solids and what we call fluids. One way of differentiating the two is to assert that solids will move from their position of rest depending on the magnitude and direction of an applied force (Howell et al. 2009), while fluids have no special rest state and respond to applied forces via a velocity distribution.

The larger the applied forces, the greater the magnitude of internal stress of most solids. In general, when the forces are released solids tend to go back to their place of rest, providing they have not been deformed to the point of yielding or breaking. This feature of solids is due to their *elasticity* and is present in all solids at some scale ¹. Elasticity is essentially what holds a solid together and is the bedrock of solid mechanics in general, and of the work carried out in this dissertation in particular.

To clarify the discussion let \mathcal{B}_0 be the reference configuration of the solid, which is often the resting state, and let $\chi : \mathcal{B}_0 \times \mathbb{R} \rightarrow \mathcal{B}$ which at any given time t is a one-to-one map that takes points from their reference position $X \in \mathcal{B}_0$ to their current position in the material $\chi(X, t) = x \in \mathcal{B}$.

Solid mechanics makes use of standard physical assumptions: for instance, the total sum of certain quantities must increase in the material \mathcal{B} according to a supply on the boundary $\partial\mathcal{B}$. The corresponding conserved quantities include mass, momentum, angular momentum and energy.

The last crucial step is to describe how the material responds to being disturbed. This is called making a *constitutive choice*. For our purposes, it boils down to how we choose a function form for the Cauchy stress tensor $\boldsymbol{\sigma}$ in terms of the map χ . To refine the constitutive choice for $\boldsymbol{\sigma}$, a key inequality of thermodynamics is often used: the entropy production inequality (also known as the Clausius-Duhem inequality).

Then, to specialise to pure elasticity, only two further assumptions need to be made (Marsden and Hughes 1994),

- (i) *History independence*: the stress tensor $\boldsymbol{\sigma}$ is independent of the history of the deformation. That is, $\boldsymbol{\sigma}$ depends only on the map $\chi(\cdot, t)$ at each instant of time t , rather than on what happened (happens) to $\chi(\cdot, t)$ before (after) time t .
- (ii) *Local dependence*: the stress tensor $\boldsymbol{\sigma}$ depends only on local quantities. In other words, for any given point $X \in \mathcal{B}_0$, the stress $\boldsymbol{\sigma}$ at x depends on χ only through how χ maps a neighbourhood of X to a neighbourhood around x .

Together all the assumptions can be used to give a functional form for $\boldsymbol{\sigma}$, which

¹Otherwise the material would flow immediately when pushed, which is a feature of non-elastic fluids.

states that (Ogden 1997)

$$\boldsymbol{\sigma} = \rho \frac{\partial \Psi}{\partial \mathbf{F}} \mathbf{F}^T, \quad (1)$$

where Ψ is the free energy density, ρ is the mass density in \mathcal{B} , $\mathbf{F} = \partial \chi / \partial X$ is the deformation gradient, and \cdot^T is the transpose operator. Once Ψ is determined, the above equation serves as a constitutive choice.

Another noted way of reaching Equation (1) is to assume that (a) energy conservation is covariant, i.e. that energy is conserved under any superimposed motion, and that (b) the free energy Ψ can be uniquely determined at $x \in \mathcal{B}$ and time t from x , t and the Riemannian metric tensor \mathbf{g} . From Assumptions (a) and (b) it is possible to derive that (Marsden and Hughes 1994) Equation (1) holds, and that the standard balance laws of mass, momentum, etc., also hold.

Recently a more general framework for elasticity has emerged (Rajagopal 2007), where Assumption (i) above is replaced with the assumption that the material response does not dissipate energy. This approach leads to implicit equations for the stress $\boldsymbol{\sigma}$ in terms of \mathbf{F} , which should be useful in those applications where it is more convenient to give the strain as a function of the stress than the reverse, for example.

Where best to apply nonlinear elasticity?

Before a mathematical theory of elasticity was developed in earnest, deformable materials such as rubber, muscle fibres and silk were studied in isolation. The models and experiments for one material were considered unrelated to those of other materials. A leap forward was made around the 1930s when these diverse materials were characterised as being seen as part of the same class of materials (Treloar 1975; Mooney 1940; Timoshenko 1953). Researchers at the time recognized that all these materials were composed of long flexible chains, that would retract when stretched. This realisation led to the theory of rubber elasticity which later accurately predicted a number of phenomena and experiments (Ogden 1972). This initial success led to the formulation of a general theory of nonlinear elasticity.

A second wind came quite recently from the breakthroughs obtained when applying nonlinear elasticity to biomechanics. Almost all biological tissues are designed to stiffen as they are strained, thereby preventing large deformations that could threaten tissue integrity. When the strain or load is removed, the tissue contracts and mostly returns to its previous state of rest. Because biological tissues are quite soft the typical physiological strain is around 10% (Murphy and Saccomandi 2015), which warrants the need for nonlinear elasticity. The theory of nonlinear elasticity is now widely used to predict and understand the mechanics of a large range of biological materials, including among others the heart (Li et al. 2001), the arteries (Holzapfel et al. 2000), the brain (Rashid et al. 2012) and the muscles (Labeit and Kolmerer 1995).

Recently researchers have been further inspired by biology to design and build soft robots that can operate in unstructured and highly congested environments, i.e. situations in which conventional rigid robots often encounter difficulties (Xydas

and Kao 1999). The theory of nonlinear elasticity will be the ideal framework for designing optimal components and systems for soft robotics.

Even in situations where tissues do not undergo large deformations, elasticity theory has to be invoked. Hence, modelling tissues with residual internal stress has been a major challenge for a long time. Internal stress in soft tissue has mostly been modelled as the consequence of deforming a stress-free material. This same approach is applied to explain residual stresses by considering a highly abstract configuration, called the virtual-configuration, where the tissue is not residually stressed. Thus even if the material does not undergo a large deformation, the theory of nonlinear elasticity is often used to model residually stressed tissues (Hoger 1997).

Stress and strain are essential triggers for the growth of tissue, and in particular residual stress is an essential part of this interplay (Ambrosi et al. 2011, Jones and Chapman 2012). This connection between stress and growth is common knowledge to the legions of athletes who increase their muscle mass by stressing their muscles through physical exercise, and has been demonstrated experimentally time and again. Connecting growth and internal stress with elasticity has led to possible explanations of why the airway in patients with chronic asthma thickens (Moulton and Goriely 2011), or of the origin of hypertrophy of the cardiovascular system and of atherosclerosis (Taber 1995).

Incremental Elasticity

Surface waves and static surface wrinkles are used in a number of applications such as in sending signals (Campbell 2012) or creating functional coatings (Genzer and Groenewold 2006). For soft solids, such as biological tissues, one of the most promising application is to use surface waves or static wrinkles to characterise the underlying elastic solid.

When a soft solid is compressed it will eventually form *static wrinkles* on its surface. The orientation and wavelength of the wrinkles are linked to the material's elastic properties. This link is well known to surgeons, who pinch tissue before operating and use the appearing wrinkles to approximate where the tension is greatest, which in turn shows how best to make an incision. A more quantitative understanding of how surface wrinkles form could lead to a more sophisticated automated process, one that would allow exact measurements to be taken. Furthermore, understanding the formation of wrinkles during growth helps explain tissue morphology, such as how the villi forms in the intestine (Balbi and Ciarletta 2013) and how the human brain gets its folded shape (Bayly et al. 2013).

Similarly, elastic *surface waves* are also essentially connected to the elastic properties of the material. For small incremental waves, a major feature is the wave's velocity, which can be quite easily measured and used to characterise the solid. Such techniques are based on the idea that the speed of an elastic wave travelling in a soft solid depends on the composition of the tissue and the tension within the tissue, i.e. on its elastic properties. So, in effect, measuring the speed of an elastic wave is an indirect measurement of the tissue's elastic properties.

The chapters in this dissertation show patterns that connect wrinkles and waves to material properties, and explore what kind of incremental phenomena can be expected when a material is deformed.

Overview of the articles

My doctoral work began by investigating how static wrinkles form when homogeneously compressing an initially isotropic solid. In Chapter 1 we show that isotropic solids can form wrinkles that do not conform to the symmetry of the deformation. We call them *oblique wrinkles*. We attempted several table-top experiments with gelatine but did not observe these predicted oblique wrinkles. Another issue was that the predicted critical strain for surface wrinkles to appear was about 30% greater than the critical strain observed in experiments. This issue has been known for some time for other pre-deformations (Gent and Cho 1999). By exploring a range of materials, we noted that the critical strain is smaller for materials that present oblique wrinkles, making it difficult to reconcile the theory to experiments. To explain the measurements, we hypothesised that the over-estimated critical strain may be due to a stiff skin effect which is present in gelatine due to the surface drying out. By developing this hypothesis we show that the skin would have to be about twice as stiff as the rest of the gelatine for the critical strain to agree with our experiments. Our findings have been submitted and are currently under review.

A more challenging task is to predict how wrinkles can form on a soft *fibre-reinforced solid*, a problem which is covered by Chapter 2. Constitutive models for fibre-reinforced solids can account for the presence of fibres by only considering the fibre's orientation and overall resistance to extension and to compression. We call these features the fibre's elastic properties, which in practice are linked to a few key parameters. In Chapter 2 we proposed two models to predict and interpret the wrinkles that appear when skin is sheared, much like the wrinkles that appear when skin is pinched. The corresponding paper was published in the *Quarterly Journal of Mechanics and Applied Mathematics* (Ciarletta et al. 2013).

The numerical instabilities faced when calculating the static wrinkle threshold of fibre-reinforced tissues led me to implement a robust numerical method based on the *surface-impedance matrix* (Fu and Mielke 2002). Over the last few decades, numerical methods for studying propagating elastic surface waves have been steadily advancing and have culminated in a technique that is robust for general anisotropy. The method relies on the introduction of the surface impedance matrix, which turns out to be the solution of a differential Riccati equation. By allowing the surface wave speed to drop to zero, this method can also reliably calculate when static wrinkles form. The method has been successfully used in a number of different scenarios by others (Norris et al. 2013, Fu et al. 2013), including certain types of inhomogeneity. This method is currently considered to be one of the most advanced and robust numerical methods available for surface-waves and instability problems in incremental elasticity. In Chapter 3 I use this method to reveal that for a diverse range of nonlinear isotropic elastic solids the fastest waves

do not necessarily travel along the direction of greatest strain. This discovery runs counter to what is commonly accepted and was published in *Wave Motion* as an invited contribution (Gower et al. 2013).

In Chapter 4, I return to *surface wrinkles on fibre-reinforced solids*. This time I use two anisotropic invariants and investigate the feasibility of using surface-wrinkles to characterise such solids. To do so, instead of using the two standard anisotropic invariants I use one invariant that measures fibre extension and another invariant that measures fibre compression. These two new anisotropic invariants lead to distinct mechanical responses, making it easier to distinguish their contribution to the overall mechanical response and wrinkle formation. Chapter 4 concludes by showing that there is a simple relationship between a soft tissue’s parameters and how wrinkles form when it is quasi-statically deformed. The results show that wrinkles can be used to evaluate not only the direction of the fibres, but also the elastic properties of the fibres. A (sole-author) paper on the findings was published in *the Journal of Engineering Mathematics* as an invited contribution (Gower 2014).

References

- Ambrosi, D. et al. (2011). “Perspectives on biological growth and remodeling”. In: *Journal of the Mechanics and Physics of Solids* 59, 863–883.
- Atkins, P., De Paula, J., and Friedman, R. (2009). *Quanta, matter, and change: a molecular approach to physical chemistry*. Oxford University Press.
- Atomic weight of Copper* (2015). <https://en.wikipedia.org/wiki/Copper>. Accessed: 2015-10-29.
- Balbi, V. and Ciarletta, P. (2013). “Morpho-elasticity of intestinal villi”. In: *Journal of The Royal Society Interface* 10, 20130109.
- Bayly, P. et al. (2013). “A cortical folding model incorporating stress-dependent growth explains gyral wavelengths and stress patterns in the developing brain”. In: *Physical Biology* 10, 016005.
- Campbell, C. (2012). *Surface Acoustic Wave Devices and their Signal Processing Applications*. Elsevier.
- Ciarletta, P., Destrade, M., and Gower, A. L. (2013). “Shear instability in skin tissue”. In: *The Quarterly Journal of Mechanics and Applied Mathematics*, hbt007.
- Fu, Y. B. and Mielke, A. (2002). “A new identity for the surface-impedance matrix and its application to the determination of surface-wave speeds”. In: *Proceedings of the Royal Society of London A* 458, 2523–2543.
- Fu, Y., Rogerson, G., and Wang, W. (2013). “Surface waves guided by topography in an anisotropic elastic half-space”. In: *Proceedings of the Royal Society of London A* 469, 20120371.
- Gent, A. and Cho, I. (1999). “Surface instabilities in compressed or bent rubber blocks”. In: *Rubber Chemistry and Technology* 72, 253–262.
- Genzer, J. and Groenewold, J. (2006). “Soft matter with hard skin: From skin wrinkles to templating and material characterization”. In: *Soft Matter* 2, 310–323.

- Gower, A. (2014). “Connecting the material parameters of soft fibre-reinforced solids with the formation of surface wrinkles”. English. In: *Journal of Engineering Mathematics*, 1–13.
- Gower, A. L., Destrade, M., and Ogden, R. (2013). “Counter-intuitive results in acousto-elasticity”. In: *Wave Motion* 50, 1218–1228.
- Hoger, A. (1997). “Virtual configurations and constitutive equations for residually stressed bodies with material symmetry”. In: *Journal of Elasticity* 48, 125–144.
- Holzappel, G. A., Gasser, T. C., and Ogden, R. W. (2000). “A new constitutive framework for arterial wall mechanics and a comparative study of material models”. In: *Journal of Elasticity* 61, 1–48.
- Howell, P., Kozyreff, G., and Ockendon, J. (2009). *Applied Solid Mechanics*. Cambridge University Press.
- Jones, G. W. and Chapman, S. J. (2012). “Modeling growth in biological materials”. In: *SIAM Review* 54, 52–118.
- Labeit, S. and Kolmerer, B. (1995). “Titins: giant proteins in charge of muscle ultrastructure and elasticity”. In: *Science* 270, 293–296.
- Li, J., Luo, X., and Kuang, Z. (2001). “A nonlinear anisotropic model for porcine aortic heart valves”. In: *Journal of Biomechanics* 34, 1279–1289.
- Marsden, J. E. and Hughes, T. J. (1994). *Mathematical Foundations of Elasticity*. Dover publications.
- Mooney, M. (1940). “A theory of large elastic deformation”. In: *Journal of applied physics* 11, 582–592.
- Moulton, D. E. and Goriely, A. (2011). “Possible role of differential growth in airway wall remodeling in asthma”. In: *Journal of Applied Physiology* 110, 1003–1012.
- Murphy, J. G. and Saccomandi, G. (2015). “Exploitation of the linear theory in the non-linear modelling of soft tissue”. In: *Mathematics and Mechanics of Solids* 20, 190–203.
- Norris, A. N., Nagy, A. J., and Amirkulova, F. A. (2013). “Stable methods to solve the impedance matrix for radially inhomogeneous cylindrically anisotropic structures”. In: *Journal of Sound and Vibration* 332, 2520–2531.
- Ogden, R. W. (1972). “Large deformation isotropic elasticity-on the correlation of theory and experiment for incompressible rubberlike solids”. In: *Proceedings of the Royal Society of London A* 326, 565–584.
- Ogden, R. W. (1997). *Non-linear Elastic Deformations*. Courier Corporation.
- Rajagopal, K. (2007). “The elasticity of elasticity”. In: *Zeitschrift für angewandte Mathematik und Physik* 58, 309–317.
- Rashid, B., Destrade, M., and Gilchrist, M. D. (2012). “Mechanical characterization of brain tissue in compression at dynamic strain rates”. In: *Journal of the Mechanical Behavior of Biomedical Materials* 10, 23–38.
- Sauermann, G., Kroy, K., and Herrmann, H. J. (2001). “Continuum saltation model for sand dunes”. In: *Physical Review E* 64 (3), 031305.
- Taber, L. A. (1995). “Biomechanics of growth, remodeling, and morphogenesis”. In: *Applied Mechanics Reviews* 48, 487–545.

- Tadmor, E. B., Miller, R. E., and Elliott, R. S. (2012). *Continuum Mechanics and Thermodynamics: From Fundamental Concepts to Governing Equations*. Cambridge University Press.
- Timoshenko, S. (1953). *History of strength of materials: with a brief account of the history of theory of elasticity and theory of structures*. Courier Corporation.
- Treloar, L. R. G. (1975). *The Physics of Rubber Elasticity*. Oxford University Press.
- Wong, S. (1998). “Multi-commodity traffic assignment by continuum approximation of network flow with variable demand”. In: *Transportation Research Part B: Methodological* 32, 567–581.
- Xydas, N. and Kao, I. (1999). “Modeling of contact mechanics and friction limit surfaces for soft fingers in robotics, with experimental results”. In: *The International Journal of Robotics Research* 18, 941–950.

Chapter 1

Looking for M. Biot's wrinkles

Artur L Gower[†] and Michel Destrade^{†‡}

Abstract

We attempt to present experimental evidence of ‘genuine’ Biot surface wrinkles—genuine in the sense that they appear during the large homogeneous deformation of a soft solid. We rely on the so-called ‘shear-box deformation’ and use common gelatine. The theory predicts that if the soft solid is modelled by third-order non-linear elasticity, then under a sufficiently large deformation, small-amplitude wrinkles appear aligned with the main diagonal of the box (‘principal wrinkles’) or along oblique directions, depending on the values of the elastic constants. Experimentally we observed principal wrinkles only, occurring slightly earlier than predicted. This latter observation can be explained by the formation of a stiff layer on the top of the gelatine during the solidification process.

1.1 Introduction

Half a century ago, Biot (1963)* predicted that when a semi-infinite soft solid is subject to a large compression, its surface eventually buckles and witnesses the formation of small-amplitude wrinkles. The Biot surface instability phenomenon is the bedrock of countless stability analyses and has been linked in particular to the appearance of wrinkles in tissue growth, hydrogel swelling, tubular organs expansion or constriction, brain sulci, etc. see the recent comprehensive reviews (Dervaux and Ben Amar 2012; Li et al. 2012).

[†]School of Mathematics, Statistics and Applied Mathematics,
National University of Ireland Galway, University Road, Galway, Ireland

[‡]School of Mechanical & Materials Engineering,
University College Dublin, Belfield, Dublin 4, Ireland.

*Note that *stricto sensu*, surface instability can be traced back at least to A.E. Green & J.E. Adkins, Large Elastic Deformations (Oxford, 1960).

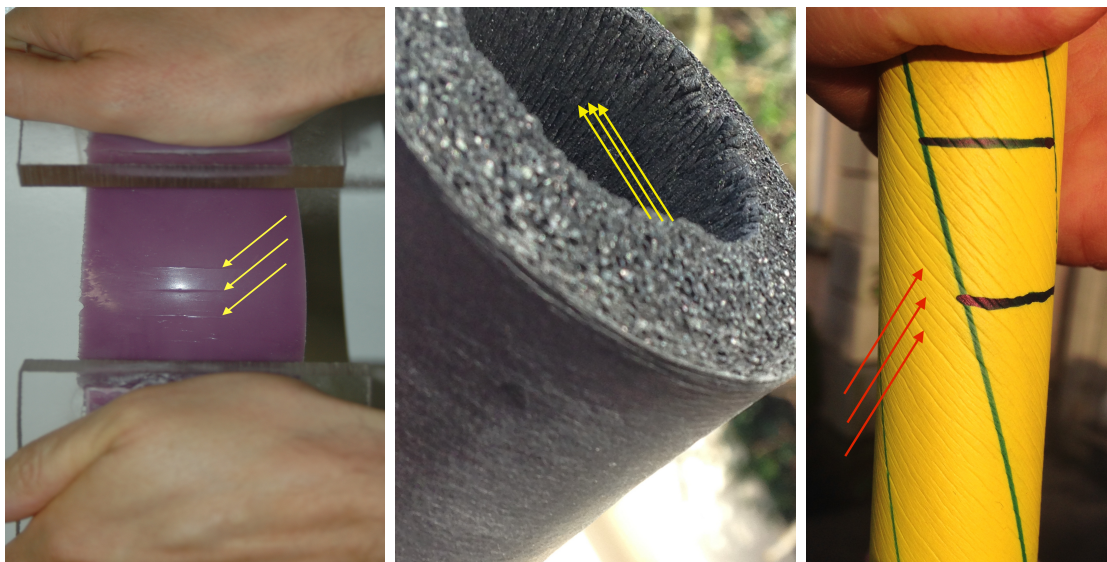


Figure 1.1: Small-amplitude wrinkles appearing in the large *non-homogeneous* deformation of soft matter, as indicated by arrows. Left: Large bending of a silicone block with two ends glued to plastic plates, on which a bending moment is applied; Middle: Everted tube of pipe insulation material; Right: Twisted cylinder, on which axial and circumferential lines were drawn prior to the twist.

Biot's modelling of the phenomenon relies on the assumptions of isotropy, homogeneity and incompressibility for the solid. He also assumes that the wrinkles are aligned with the principal directions of the large deformation, which itself is assumed to be *homogeneous* that is, such that parallel material lines remain parallel during the deformation (hence they are brought together in the direction of compression and pulled apart in the direction(s) of extension).

However, in practice it is difficult to achieve large homogeneous compressions of soft matter to the point of instability. In the compression of a sample, finite size effects take precedence and the solid buckles as a column or a plate, not as a half-space. For this reason, experimental surface wrinkling is usually observed in a localised, limiting sense: for instance, on the inner compressed side of bent blocks and sectors (see photographs in Gent and Cho 1999; Destrade et al. 2010c; Destrade et al. 2010a; Roccabianca et al. 2011); or on the inside face of an everted thick tube; or on the face of a twisted cylinder (Mora et al. 2011; Ciarletta and Destrade 2014). See Figure 1.1 for further photographic evidence. In those cases, the Biot instability corresponds to the small wavelength/large thickness limit, but is overshadowed by earlier buckling modes due to the finite size of the deformed samples.

In *simple shear* (a homogeneous deformation), it can be deduced from Biot's analysis that wrinkling occurs for a neo-Hookean material (Destrade et al. 2008) when the angle of shear is 71° . However, experimental simple shear is achieved by moving one face of a rectangular block parallel to the opposite face and at such a large angle, the slanted faces are bent and the deformation field is inhomogeneous, a well recognised problem in standard testing protocols (ISO 8013:2006).

Here we set out to generate a fully homogeneous shear-like deformation that can bring soft matter to the brink of the Biot surface instability phenomenon, and we compare theoretical predictions with experimental results. Specifically, we built a four-sided box with hinged edges. We half-filled it with a gelatine gel and then deformed that soft solid according to what we call the *shear-box deformation* Rajagopal and Wineman 1987; Stolz 2010; Gower 2014. The box’s walls support and accompany the gelatine’s sides during the deformation, and so the slanted sides do not bend and a (reasonably) homogeneous field is achieved, see Figure 1.2.

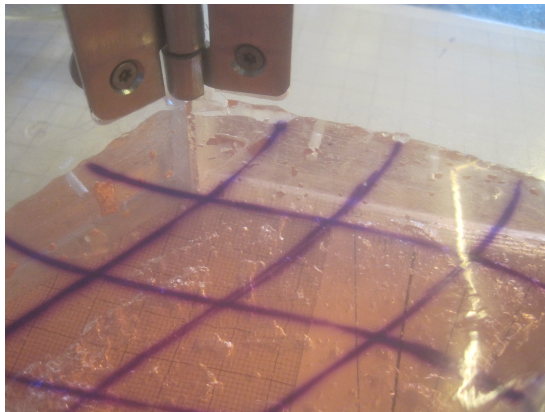


Figure 1.2: The shear-box generates an almost homogeneous deformation field, especially in the central region. Here we drew a grid of lines parallel to the box’s sides on the top face of the gelatine prior to the deformation.

At a certain critical angle of tilting, *small-amplitude wrinkles* appear on the surface. In all our experiments we found them to be aligned with the direction of greatest stretch, in this case the long diagonal of the shear-box. We also investigated what type of general third-order elastic material supports those ‘principal’ wrinkles, as opposed to ‘oblique’ wrinkles, which would appear at an angle with respect to the diagonal. Investigating whether such oblique buckling wrinkles exist is not simply an academic exercise as they have been observed in other settings, such as in thin plates under in-plane compression (Audoly et al. 2002), polymeric strips (Wang et al. 2011) or meta-sedimentary rocks (Meere et al. 2013). Similarly it has been predicted that surface seismic waves do not necessarily travel at their extreme speeds along the principal directions of deformation (Gower et al. 2013).

1.2 Methods

1.2.1 Theoretical

To model the large homogeneous strain of the material, we use the *shear-box deformation* (Stolz 2010). It brings a point with material coordinates (X_1, X_2, X_3) to the spatial position with coordinates (x_1, x_2, x_3) given by

$$x_1 = X_1 + X_2 \sin \theta, \quad x_2 = X_2 \cos \theta, \quad x_3 = X_3 / \cos \theta, \quad (1.1)$$

where θ is the *tilting angle*: at $\theta = 0$, the box is rectangular; at $\theta = 90^\circ$, it is flattened. We consider the material to original be a half-space defined by $X_3 \leq 0$. Figure 1.3 shows a sketch of the shear-box and shear-box deformation.

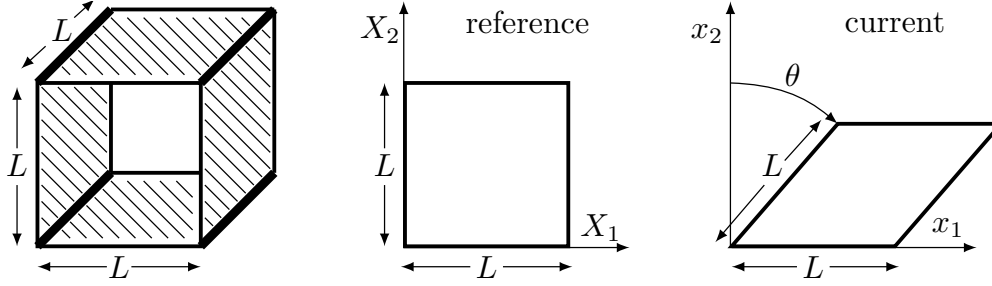


Figure 1.3: Shear-box and shear-box deformation.

The deformation gradient associated with Eq.(1.1) is $\mathbf{F} = \partial \mathbf{x} / \partial \mathbf{X}$. Calling $(\mathbf{E}_1, \mathbf{E}_2, \mathbf{E}_3)$ and $(\mathbf{e}_1, \mathbf{e}_2, \mathbf{e}_3)$ the orthonormal bases along the material and spatial axes, respectively, its components in the $\mathbf{e}_i \otimes \mathbf{E}_j$ basis are

$$\mathbf{F} = \begin{bmatrix} 1 & \sin \theta & 0 \\ 0 & \cos \theta & 0 \\ 0 & 0 & 1 / \cos \theta \end{bmatrix}. \quad (1.2)$$

Clearly, the shear-box deformation is isochoric ($\det \mathbf{F} = 1$) and homogeneous (\mathbf{F} is constant in \mathbf{X}). It is thus compatible with any model of isotropic nonlinear elasticity (Shield 1971). The corresponding principal stretches can be calculated by taking the square root of the eigenvalues of $\mathbf{F}\mathbf{F}^T$, which are

$$\lambda_{1,2} = \cos(\theta/2) \pm \sin(\theta/2), \quad \lambda_3 = 1 / \cos \theta, \quad (1.3)$$

and that they occur along the diagonals of the shear-box in the (x_1, x_2) plane and along the x_3 direction, respectively. Note that λ_1 is along the long diagonal and λ_2 is along the short diagonal.

For the modelling of the soft solid, we use the *Mooney-Rivlin material*, because it captures early non-linear (third-order) elastic effects. Its strain energy density W is linear in $I_1 = \text{tr}(\mathbf{C})$ and $I_2 = \text{tr}(\mathbf{C}^{-1})$, where $\mathbf{C} = \mathbf{F}^T \mathbf{F}$ is the right Cauchy-Green deformation tensor. It reads as

$$W = \frac{1}{4} \mu [(1 + \beta)(I_1 - 3) + (1 - \beta)(I_2 - 3)], \quad (1.4)$$

where $\mu > 0$ is the shear modulus and β is a scalar, such that $-1 \leq \beta \leq 1$. Note that these inequalities ensure the strong ellipticity of the incremental equations of equilibrium (Destrade and Scott 2004). At $\beta = 1$, W recovers the so-called neo-Hookean material (linear in I_1) and at $\beta = -1$, the so-called Extreme-Mooney (Shield 1971) material (linear in I_2).

At the same order of approximation in the Green strain $\mathbf{E} = (\mathbf{C} - \mathbf{I})/2$, it is equivalent to the most general model of isotropic, incompressible third-order elasticity,

$$W = \mu_0 \text{tr}(\mathbf{E}^2) + \frac{1}{3} A \text{tr}(\mathbf{E}^3), \quad (1.5)$$

where $\mu_0 > 0$ is the second-order Lamé coefficient and A is the third-order Landau constant. The connections between those constants are (Destrade et al. 2010b): $\mu_0 = \mu$, $A = \mu(\beta - 3)$, which puts bounds on A in order to ensure strong ellipticity of the incremental equations: $-4\mu_0 \leq A \leq -2\mu_0$. We also use a Mooney-Rivlin material (1.4) as it is the simplest model available that produces oblique wrinkles.

For the modelling of *surface wrinkles*, we use the bifurcation criterion of incremental non-linear elasticity. It gives the equation satisfied by the principal stretches when a small-amplitude perturbation is superposed onto a large pre-deformation (here, the shear-box deformation). We consider the perturbation to vary sinusoidally on the surface, with exponential decay of the amplitude with depth away from the surface. The *obliquity angle* is φ , the angle between the wavefront of the wrinkles and the direction of the largest stretch (the long diagonal of the shear-box): at $\varphi = 0$, the wrinkles are normal to the direction of greatest compression, at $\varphi \neq 0$, they are *oblique*, see Figure 1.4.

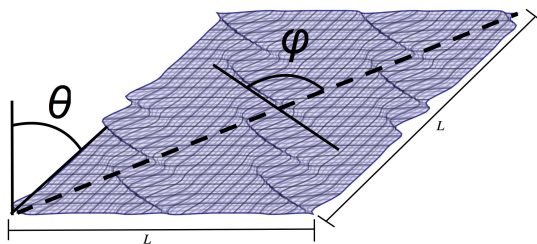


Figure 1.4: The shear-box deformation at a critical threshold of oblique surface instability, with tilting angle θ . The dashed line indicates the direction of greatest stretch (aligned with the long diagonal) and φ is the angle between that direction and the wrinkle orientation (critical angle of obliquity)

Destrade et al. (2005) found an explicit secular equation for surface waves in deformed Mooney-Rivlin materials, from which the bifurcation criterion here can be found by taking the wave speed to be zero. We used this explicit secular equation to model the formation of wrinkles (it is too long to reproduce here). Succinctly, the bifurcation criteria is calculate by super-imposing an incremental wrinkle in the form of $\mathbf{U}e^{i(a_1x_1+a_2x_2)}e^{ipx_3}$ on top of the shearbox deformation Eq. (1.1). Both a_1 and a_2 are real and are chosen so as to orient the wrinkles in the φ direction as described above; the vector \mathbf{U} gives the direction of motion; and the imaginary part of p is negative so that the wrinkle decays as $x_3 \rightarrow -\infty$.

There are three short expressions of that equation in special cases. For neo-Hookean materials ($f = 1$ or $A = -2\mu_0$), Flavin (1963) found the following bifurcation criterion

$$\lambda_1^2 \lambda_2^2 (\lambda_1^2 \sin^2 \varphi + \lambda_2^2 \cos^2 \varphi) = \sigma_0^2, \quad (1.6)$$

where here $\sigma_0 \simeq 0.2956$ is the real root of the cubic $\sigma^3 + \sigma^2 + 3\sigma - 1 = 0$. In other words, when λ_1 , λ_2 and φ are real and satisfy the above, then a surface wrinkle has formed. For the Extreme-Mooney material ($\beta = -1$ or $A = -4\mu_0$) we found the following explicit bifurcation criterion,

$$\sigma_0^4 + \sigma_0^3 + \lambda_1^2 \lambda_2^2 (\lambda_1^4 \lambda_2^4 - \lambda_2^2 - \lambda_1^2) \sigma_0 (\sigma_0 + 1) + 4\lambda_1^6 \lambda_2^6 = 0, \quad (1.7)$$

with σ_0 given by Eq.(1.6). Using a computer algebra system, the roots of the above for σ_0 can be obtained, and then substituted in Eq.(1.6) to get an explicit buckling criteria. This analytical solution is too long to reproduce here but its numerical values are shown in Figure 1.6 as the darkest blue curve ($\beta = -1$). Finally, for a wrinkle-front aligned with the long diagonal of the shear-box ($\varphi = 0$), we have so-called ‘principal’ wrinkles. For these, Flavin (1963) showed that the bifurcation criterion is independent of the material parameters μ , β for the whole Mooney-Rivlin class; it reads

$$\lambda_1 \lambda_2^2 = \sigma_0, \quad (1.8)$$

where again $\sigma_0 \simeq 0.2956$. We used these explicit equations as benchmarks for the more general case, where the bifurcation criterion depends only on one material parameter, β (or equivalently, on A/μ_0 only).

1.2.2 Experimental

We prepared 12 different gels, using commercial gelatine in several forms: solid leafs, powders, or concentrated cubes to be dissolved in water. We varied the concentrations, from that prescribed by the manufacturers to three times the normal concentration.

For the shear-box, we assembled four acrylic plates (1.0 cm \times 10 cm \times 10 cm) into a cube with four hinged edges.

We poured about 300 ml of gelatine gel into the shear-box and let it set into a solid phase, either at room or at refrigerated temperature, from 4 to 12 hours depending on the specimen.

The gelatine gel was then subjected to a shear-box deformation, simply by applying manual pressure on two opposite hinged edges of the box, until wrinkles first appeared to the naked eye, see Figure 1.5. The corresponding critical angle was recorded.

1.3 Results

Numerically, for each material (β given, or equivalently, A/μ_0), we implemented a procedure to find the critical tilting angle θ of the shear-box for each obliquity angle φ of the wrinkles, see results in Figure 1.6. Then we looked for the absolute minimum tilt θ^* and corresponding obliquity angle φ^* to identify the earliest onset of surface wrinkles. For $0 \leq \beta \leq 1$ ($-3\mu_0 \leq A \leq -2\mu_0$) we found that the minimum is at $\varphi^* = 0^\circ$, indicating principal wrinkles, aligned with the long diagonal of the sheared box. Moreover, these solids should all buckle at the same critical tilting angle $\theta^* \simeq 51.1^\circ$, independent of the material constants (θ^* is found with best precision by solving the explicit bifurcation criterion Eq.(1.8), with λ_1 and λ_2 given by Eq.(1.3).) It corresponds to a critical compressive stretch of $\lambda_2^* = 0.47$, i.e. a compressive nominal strain $\varepsilon = 100(1 - \lambda_2) = 53\%$. For $-1 \leq \beta \leq 0$ ($-4\mu_0 \leq A \leq -3\mu_0$), the point with coordinates $(\varphi, \theta) = (0^\circ, 51.1^\circ)$ becomes a relative maximum whilst the minimum now occurs for oblique wrinkles, at values

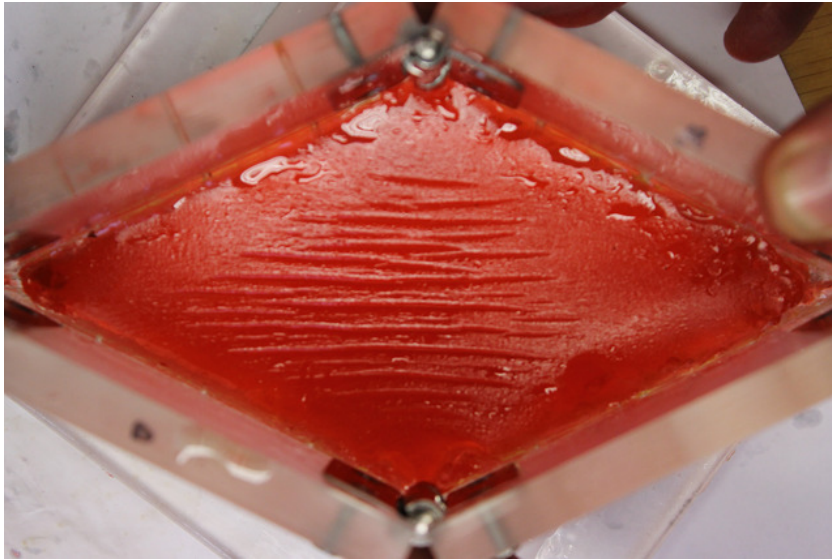


Figure 1.5: Deforming (almost) homogeneously a block of strawberry-flavoured jelly using a shear-box, until small-amplitude wrinkles appear on its surface. The critical angle of tilting is $\theta \simeq 38^\circ$ and the wrinkles are aligned with the long diagonal (principal wrinkles).

dependent on the value of β . The earliest onset of surface instability occurs for the Extreme-Mooney material, where $(\varphi^*, \theta^*) = (33.2^\circ, 45.2^\circ)$.

Experimentally, we noted that the first wrinkles to appear were always principal wrinkles ($\varphi^* = 0$), aligned with the long diagonal of the shear-box. We found that $\theta^* = 38 \pm 2^\circ$, irrespective of the concentration and type of gelatine used for the gel sample.

1.4 Discussion and Conclusion

Our first observation is that oblique wrinkles do not appear for gelatine gels, indicating that, should they be modelled by the Mooney-Rivlin or third-order elasticity models, their material parameters must satisfy the following inequalities

$$0 \leq \beta \leq 1, \quad \text{or} \quad -3 \leq A/\mu_0 \leq -2. \quad (1.9)$$

Second, we recorded that *all* gels experienced surface instability at the same level of compression, when $\theta^* = 38^\circ$, corresponding to $\lambda_2^* = 0.62$ (*i.e.* a compression $\varepsilon = 38\%$). In that respect, the Mooney-Rivlin and third-order elasticity models are adequate, as their predictions of the appearance of principal wrinkles are independent of the material parameters.

Finally, it remains to explain why the experiments yielded a measured critical threshold of instability lower than the one predicted by the models ($\theta^* = 38^\circ$ instead of 51° , $\varepsilon = 38\%$ instead of 47%). We noted that when the gelatine was left to solidify for the shortest possible time, regularly-spaced creases formed on the free surface instead of sinusoidal wrinkles, see arrows in Figure 1.1(a,c) and Figure

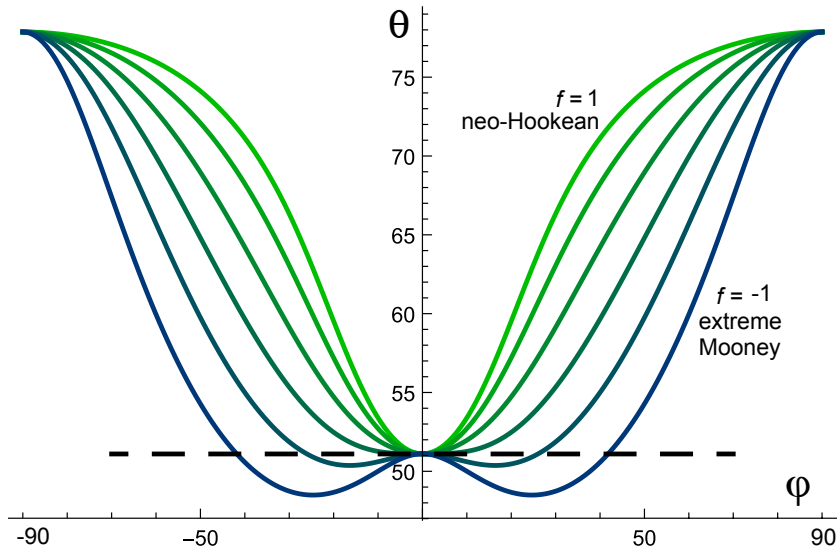


Figure 1.6: Plot showing the variations of the critical angle of tilting θ of the shear-box as a function of the obliquity angle φ of the wrinkles, for different values of the elastic constants ($-1 \leq \beta \leq 1$ or $-4 \leq A/\mu_0 \leq -2$) where β takes the values $-1.0, -0.6, -0.28, 0.04, 0.36, 0.68$ and 1.0 , from the blue to the green curve. The absolute minimum θ^* of each curve and corresponding φ^* predict the critical angles of tilting and obliquity, respectively.

1.7. These subcritical nonlinear perturbations are known to appear earlier than Biot's wrinkles, see numerical simulations in (Hong et al. 2009; Cao and Hutchinson 2011). These creases are difficult to calculate as they require a nonlinear perturbation analysis. They are subcritical in the sense that they are energetically favourable to wrinkles and appear before wrinkles do for homogeneous neo-hookean solids (Cao and Hutchinson 2011).

However, if the gelatine was left to solidify overnight then regular, sinusoidal wrinkles appeared. We suggest that a *stiffer film* formed on the top of the gelatine block, due to surface dehydration during the longer cooling process.

We may thus investigate how much stiffer the film was compared to the substrate: we use Figure 1.8, in which we plot the critical quantity $\lambda_a \lambda_b^{-1}$ against Γ , the stiffness contrast ratio, see the appendix for details. Here λ_a, λ_b are the principal stretch ratios in the directions normal to the wrinkles and to the free surface, respectively. Hence for the shear-box deformation Eq.(1.1), $\lambda_a = \lambda_2$ and $\lambda_b = (\lambda_1 \lambda_2)^{-1}$. When $\Gamma = 1$, the film has the same stiffness as the substrate and the criterion Eq.(1.8) applies. In our experiments we recorded $\theta^* = 38^\circ$, giving $\lambda_2 = 0.620$ and $\lambda_1 = 1.271$ by Eq.(1.3). Then $\lambda_a \lambda_b^{-1} \simeq 0.49$, indicating that $\Gamma \simeq 2.0$, according to Figure 1.8, see dotted lines.

Our overall conclusion is that in our experimental search for Biot's wrinkles we produced mixed results: (i) We were able to produce a large homogeneous pre-strain using gelatine in a shear-box; (ii) We found under which conditions the wrinkles should be principal (aligned with the direction of greatest stretch) or

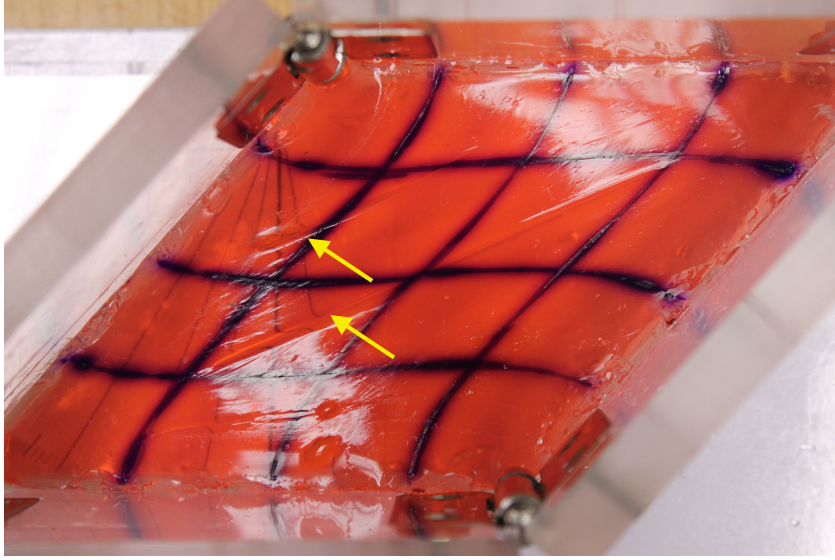


Figure 1.7: Freshly solidified gelatine tends to exhibit surface creases instead of sinusoidal wrinkles. Compare with Figure 1.5, where the gelatine was left overnight to solidify.

oblique; (iv) Experimentally, we obtained principal sinusoidal wrinkles; (v) But they were earlier than expected, which we ascribe to the formation of a film over the block, which was estimated to be twice as stiff as the underlying substrate. However, our conclusions only show that a stiff thin film is one possible explanation. Alternative explanations are that we are observing creases and not wrinkles or that the gelatine is not well described by a third-order expansion of the strain-energy in terms of the Green strain.

Appendix

Here we consider the possibility that the top surface of the gelatine block (in contact with air) has dried out and stiffened faster than the rest of the enclosed block during the solidification process. We model the resulting heterogeneous structure as a composite material: a thin film of thickness $2h$, say, in the region $-h \leq x_3 \leq h$, in rigid contact with a substrate in the region $h \leq x_3 \leq \infty$. The strain energy of each solid is expanded up to third order of Green strain as

$$\begin{aligned} W_f &= \mu_{0f} \operatorname{tr}(\mathbf{E}^2) + \frac{1}{3} A_f \operatorname{tr}(\mathbf{E}^3), \\ W_s &= \mu_{0s} \operatorname{tr}(\mathbf{E}^2) + \frac{1}{3} A_s \operatorname{tr}(\mathbf{E}^3), \end{aligned} \quad (\text{A.1})$$

respectively.

Now consider the mechanical response of these two solids to common modes of deformation such as uni-axial tension under Cauchy tensile stress T and simple shear under Cauchy shear stress S . Then, up to second order in the strain, we

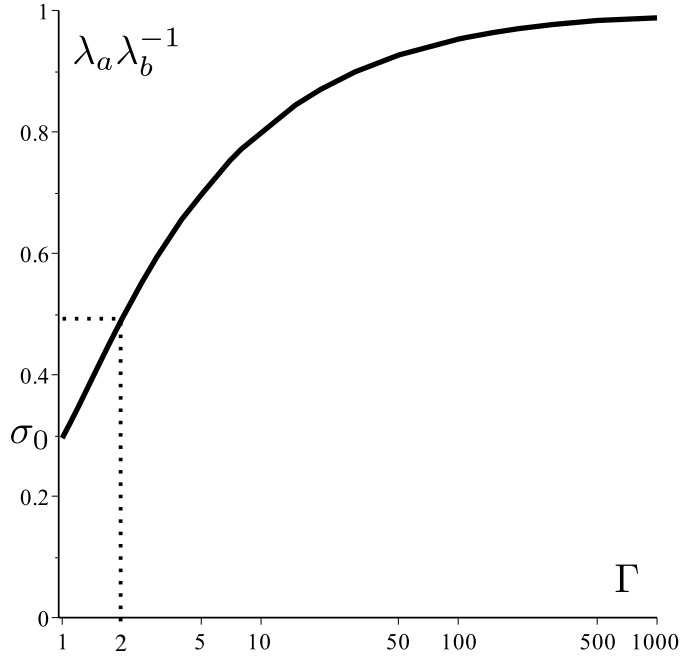


Figure 1.8: Critical measure of deformation $\lambda_a \lambda_b^{-1}$ in terms of the stiffness contrast Γ for a deformed film/substrate block.

have for the film and for the substrate

$$\begin{aligned} T_f &= 3\mu_{0f} \varepsilon + 3(\mu_{0f} + A_f/4)\varepsilon^2, & S_f &= \mu_{0f} \varepsilon, \\ T_s &= 3\mu_{0s} \varepsilon + 3(\mu_{0s} + A_s/4)\varepsilon^2, & S_s &= \mu_{0s} \varepsilon, \end{aligned} \quad (\text{A.2})$$

respectively, and similarly for other modes of deformation. (Here, the measure of strain ε is in turn the elongation and the amount of shear.) A consistent way to ensure that the response of the film is always ‘stiffer’ than that of the substrate is to take

$$\mu_{0f} = \Gamma \mu_{0s}, \quad A_f = \Gamma A_s, \quad \text{where } \Gamma > 1 \quad (\text{A.3})$$

is defined as the coefficient of stiffness contrast. For the constants of the Mooney-Rivlin material Eq.(1.4), this translates as

$$\mu_f = \Gamma \mu_s, \quad \beta_f = \beta_s. \quad (\text{A.4})$$

Then the film is always stiffer than the substrate, in the sense that the magnitude of its stress response to any mechanical strain is Γ times that of the substrate.

The formulas we present below can readily be deduced by specialising the results of (Shuvalov and Every 2002; Destrade 2007) to the present context. For our type of layered structure, we may write the bifurcation criterion for principal wrinkles as

$$\det(\Gamma \mathbf{z}_f - \mathbf{z}_s) = 0, \quad (\text{A.5})$$

where \mathbf{z}_f , \mathbf{z}_s are non-dimensionalised surface impedance matrices for the film and the substrate, respectively. Explicitly, $\mathbf{z}_s = -i\mathbf{B}\mathbf{A}^{-1}$, where

$$\mathbf{A} = \begin{bmatrix} 1 & \lambda_a^2 \lambda_b^{-2} \\ i & i\lambda_a \lambda_b^{-1} \end{bmatrix}, \quad \mathbf{B} = \begin{bmatrix} 2i & i\lambda_a \lambda_b^{-1}(1 + \lambda_a^2 \lambda_b^{-2}) \\ -1 - \lambda_a^2 \lambda_b^{-2} & -2\lambda_a^2 \lambda_b^{-2} \end{bmatrix}, \quad (\text{A.6})$$

and $\mathbf{z}_f = -i\mathbf{M}_3\mathbf{M}_1^{-1}$, where \mathbf{M}_1 , \mathbf{M}_3 are the respective top-left and bottom-left 2×2 sub-matrices of the matricant $\mathcal{N}\boldsymbol{\varepsilon}\mathcal{N}^{-1}$. Here,

$$\mathcal{N} = \begin{bmatrix} \mathbf{A} & \overline{\mathbf{A}} \\ \mathbf{B} & \overline{\mathbf{B}} \end{bmatrix}, \quad \boldsymbol{\varepsilon} = \text{Diag} \left(e^{-2kh}, e^{-2(\lambda_a \lambda_b^{-1})kh}, e^{2kh}, e^{2(\lambda_a \lambda_b^{-1})kh} \right), \quad (\text{A.7})$$

the overbar denotes the complex conjugate and k is the wavenumber of the wrinkle. Also, $\lambda_a < 1$ is the principal stretch in the direction normal to the wavefront and λ_b is the principal stretch along the normal to the boundaries.

We may then follow the same strategy as Cao and Hutchinson (2012) to find the critical amount of deformation signalling the onset of sinusoidal wrinkles. When $\Gamma = 1$, the system is homogeneous and non-dispersive: the wrinkles appear when $\lambda_a \lambda_b^{-1} = 0.2956$, see Eq.(1.8). For example, plane strain was considered in (Cao and Hutchinson 2012), where $\lambda_a = \lambda$, $\lambda_b = 1/\lambda$ and thus $\lambda = (0.2956)^{1/2} = 0.544$, the Biot value (Biot 1963). When $\Gamma > 1$, the film/substrate structure is dispersive and to each value of kh corresponds a value of $\lambda_a \lambda_b^{-1}$ where Eq.(A.5) is satisfied. By varying kh we can find the maximal value for $\lambda_a \lambda_b^{-1}$, which will be the critical value at which the structure wrinkles. Then by varying Γ , we can plot Figure 1.8, which yields Figure 2 of (Cao and Hutchinson 2012) when the film and the substrate are both neo-Hookean and the deformation is plane strain.

Acknowledgements

The financial support of the Hardiman Foundation (NUI Galway) and of the Government of Ireland Postgraduate Scholarship Scheme (Irish Research Council) is gratefully acknowledged. We also thank Molly Aitken, Jorge Bruno, Juliet Destrade, Lucille Destrade, Sean Leen, Joanne McCarthy and Deirdre McGowan Smyth for their technical input.

References

- Audoly, B., Roman, B., and Pocheau, A. (2002). ‘‘Secondary buckling patterns of a thin plate under in-plane compression’’. In: *The European Physical Journal B-Condensed Matter and Complex Systems* 27, 7–10.
- Biot, M. (1963). ‘‘Surface instability of rubber in compression’’. In: *Appl. Sc. Res.* 12, 168–182.
- Cao, Y. and Hutchinson, J. W. (2011). ‘‘From wrinkles to creases in elastomers: the instability and imperfection-sensitivity of wrinkling’’. In: *Proceedings of the Royal Society of London A: Mathematical, Physical and Engineering Sciences* 468, 94–115.

- Cao, Y. and Hutchinson, J. W. (2012). “Wrinkling phenomena in neo-Hookean film/substrate bilayers”. In: *Journal of Applied Mechanics* 79, 031019.
- Ciarletta, P. and Destrade, M. (2014). “Torsion instability of soft solid cylinders”. In: *IMA Journal of Applied Mathematics* 79, 804–819.
- Dervaux, J. and Ben Amar, M. (2012). “Mechanical instabilities of gels”. In: *Annual Review of Condensed Matter Physics* 3, 311–332.
- Destrade, M., Murphy, J. G., and Ogden, R. W. (2010a). “On deforming a sector of a circular cylindrical tube into an intact tube: existence, uniqueness, and stability”. In: *International Journal of Engineering Science* 48, 1212–1224.
- Destrade, M. (2007). “Interface Waves in Pre-Stressed Incompressible Solids”. In: *Waves in Nonlinear Pre-Stressed Materials*. Ed. by M. Destrade and G. Saccomandi. Vol. 495. CISM Courses and Lectures. Springer Vienna, 63–102.
- Destrade, M., Gilchrist, M. D., and Murphy, J. G. (2010b). “Onset of nonlinearity in the elastic bending of blocks”. In: *Journal of Applied Mechanics* 77, 061015.
- Destrade, M. and Scott, N. H. (2004). “Surface waves in a deformed isotropic hyperelastic material subject to an isotropic internal constraint”. In: *Wave Motion* 40, 347–357.
- Destrade, M. et al. (2005). “Non-principal surface waves in deformed incompressible materials”. In: *International Journal of Engineering Science* 43, 1092–1106.
- Destrade, M. et al. (2008). “Surface instability of sheared soft tissues”. In: *Journal of Biomechanical Engineering* 130, 061007.
- Destrade, M. et al. (2010c). “Bimodular rubber buckles early in bending”. In: *Mechanics of Materials* 42, 469–476.
- Flavin, J. (1963). “Surface waves in pre-stressed Mooney material”. In: *The Quarterly Journal of Mechanics and Applied Mathematics* 16, 441–449.
- Gent, A. and Cho, I. (1999). “Surface instabilities in compressed or bent rubber blocks”. In: *Rubber Chemistry and Technology* 72, 253–262.
- Gower, A. (2014). “Connecting the material parameters of soft fibre-reinforced solids with the formation of surface wrinkles”. English. In: *Journal of Engineering Mathematics*, 1–13.
- Gower, A. L., Destrade, M., and Ogden, R. (2013). “Counter-intuitive results in acousto-elasticity”. In: *Wave Motion* 50, 1218–1228.
- Hong, W., Zhao, X., and Suo, Z. (2009). “Formation of creases on the surfaces of elastomers and gels”. In: *Applied Physics Letters* 95, 111901.
- ISO 8013:2006 (2006). *Rubber, vulcanized — Determination of creep in compression or shear*.
- Li, B. et al. (2012). “Mechanics of morphological instabilities and surface wrinkling in soft materials: a review”. In: *Soft Matter* 8, 5728–5745.
- Meere, P. A., Mulchrone, K. F., and Timmerman, M. (2013). “Shear folding in low-grade metasedimentary rocks: Reverse shear along cleavage at a high angle to the maximum compressive stress”. In: *Geology* 41, 879–882.
- Mora, S. et al. (2011). “Surface instability of soft solids under strain”. In: *Soft Matter* 7, 10612–10619.
- Rajagopal, K. and Wineman, A. S. (1987). “New universal relations for nonlinear isotropic elastic materials”. In: *Journal of elasticity* 17, 75–83.

- Roccabianca, S., Bigoni, D., and Gei, M. (2011). “Long wavelength bifurcations and multiple neutral axes of elastic layered structures subject to finite bending”. In: *Journal of Mechanics of Materials and Structures* 6, 511–527.
- Shield, R. (1971). “Deformations possible in every compressible, isotropic, perfectly elastic material”. In: *Journal of Elasticity* 1, 91–92.
- Shuvalov, A. and Every, A. (2002). “Some properties of surface acoustic waves in anisotropic-coated solids, studied by the impedance method”. In: *Wave Motion* 36, 257–273.
- Stolz, C. (2010). *Milieux Continus en Transformations Finies*. Palaiseau: Editions de l’Ecole Polytechnique.
- Wang, Q. et al. (2011). “Buckling modes of polymer membranes restricted by metal wires”. In: *Soft Matter* 7, 2888–2894.

Chapter 2

Shear Instability in Skin Tissue

Pasquale Ciarletta*, Michel Destrade^{†‡} and Artur L. Gower[‡]

Abstract

We propose two toy-models to describe, predict, and interpret the wrinkles appearing on the surface of skin when it is sheared. With the first model, we account for the lines of greatest tension present in human skin by subjecting a layer of soft tissue to a pre-stretch, and for the epidermis by endowing one of the layer's faces with a surface tension. For the second model, we consider an anisotropic model for the skin, to reflect the presence of stiff collagen fibres in a softer elastic matrix. In both cases, we find an explicit bifurcation criterion, linking geometrical and material parameters to a critical shear deformation accompanied by small static wrinkles, with decaying amplitudes normal to the free surface of the skin.

2.1 Introduction

When the skin is pinched, wrinkles appear quite early on its surface. The same phenomenon occurs when the skin is sheared, i.e. pinched with one finger moving in one direction and the other fixed or moving in the opposite direction. In fact, pinching is one of the tests performed by dermatologists and surgeons (Waldorf et al. 2002) when trying to assess the direction of greatest tension (Kraissl 1951) in the neighborhood of a site of interest. Sometimes called *lines of cleavage* (Cox 1941), the orientations of the lines of greatest tension are crucial to the way a scar

*CNRS and Université Pierre et Marie Curie - Paris 6,
Institut Jean le Rond d'Alembert, UMR CNRS 7190,
4 place Jussieu, Case 162, 75005 Paris, France

[†]School of Mathematics, Statistics and Applied Mathematics,
National University of Ireland Galway, University Road, Galway, Ireland

heals. For a cut across the lines, the lips of a wound will be pulled away from one another during the healing process, while they will be drawn together if the cut has occurred parallel to the lines. In one case the resulting scar can be quite unsightly, in the other it is almost invisible. In this paper we investigate the mechanical stability of two toy models of human skin under shear in its plane, and view the onset of small-amplitude, unstable solutions as a prototype for skin wrinkling.

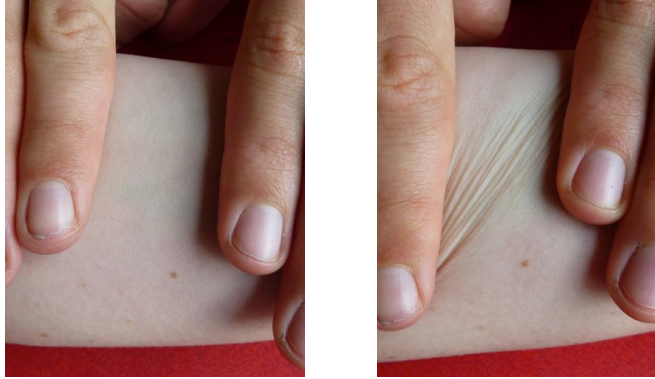


Figure 2.1: Shearing the forearm skin across the lines of cleavage (which run along the length of the arm) results in early onset of small-amplitude wrinkles.

Of course, skin is a complex, multi-faceted organ, and it is not easily, nor perhaps realistically, modelled. In Section 2.2, we view it as an initially isotropic, neo-Hookean layer of finite thickness. We let it be subject to a surface tension on one face, in order to model an epidermis of vanishing thickness on top of a highly elastic dermis. In other words we let one of the layer's faces be a material curve endowed with intrinsic elastic properties associated with extensibility, but no bending stiffness (see Steigmann and Ogden (1997) for a rigorous exposition of such elastic coatings). We account for the lines of greatest tension by imposing a finite plane pre-stretch in a given direction; in other words, we simulate those lines through *strain-induced anisotropy*. Then we investigate whether surface tension and pre-stretch promote or attenuate the appearance of wrinkles when the layer is subject to simple shear in the direction of the cleavage lines.

In Section 2.3, we view skin as being intrinsically *anisotropic* that is, we switch to the point of view that lines of greatest tension are due to the presence of families of parallel bundles of stiff collagen fibres embedded in a softer elastin matrix. The introduction of even the simplest anisotropy – transverse isotropy due to a single privileged direction – complicates the equations of incremental instability greatly, and we thus restrict attention to a homogeneous solid without surface tension. We also omit finite-size effects by considering a half-space instead of a layer, and thus by focusing on the Biot surface instability phenomenon (Biot 1963). Here, the anisotropic contribution to the stored energy is that recently proposed by Ciarletta et al. (2011). Its polyconvexity ensures good properties from the physical point of view, such as strong ellipticity in compression, in contrast to the standard reinforcing model used recently by Destrad et al. (2008) for the same stability study.

2.2 Shear instability for a neo-Hookean layer with surface tension

First we consider an isotropic elastic material of finite thickness H , undergoing an homogeneous shear. In order to mimic the response of human skin, we incorporate the presence of a residual stretch λ_{res} along the main cleavage lines, so that the base deformation field reads

$$x = \lambda_{\text{res}}X + (K/\lambda_{\text{res}})Y, \quad y = Y/\lambda_{\text{res}}, \quad z = Z, \quad (2.1)$$

where \mathbf{x} is the current position of a material point which was at \mathbf{X} in the reference configuration, and K is a constant. Hence, we see that the deformation can be decomposed as a plane stretch of amount λ_{res} followed by a simple shear of amount K , with deformation gradient \mathbf{F} written as

$$\mathbf{F} = \begin{bmatrix} \lambda_{\text{res}} & K/\lambda_{\text{res}} & 0 \\ 0 & 1/\lambda_{\text{res}} & 0 \\ 0 & 0 & 1 \end{bmatrix} = \begin{bmatrix} 1 & K & 0 \\ 0 & 1 & 0 \\ 0 & 0 & 1 \end{bmatrix} \begin{bmatrix} \lambda_{\text{res}} & 0 & 0 \\ 0 & 1/\lambda_{\text{res}} & 0 \\ 0 & 0 & 1 \end{bmatrix}. \quad (2.2)$$

We note that the layer's thickness H remains unchanged through the deformation. For simplicity, we take the layer to be made of an isotropic neo-Hookean incompressible material with a surface energy at the free boundary $z = 0$, so that its total strain energy W reads

$$W = \frac{\mu}{2} \iiint (\text{tr } \mathbf{B} - 3) dX dY dZ + \gamma \iint |\mathbf{x}_{,X} \times \mathbf{x}_{,Y}| dX dY, \quad (2.3)$$

where μ is the shear modulus, $\mathbf{B} = \mathbf{F}\mathbf{F}^T$ is the left Cauchy-Green deformation tensor, γ is the surface energy density, and the comma denotes partial differentiation. This is akin to endowing one of the material boundaries of the layer with a surface energy that is proportional to changes in area, as is often done in fluid mechanics (Lautrup 2005) and has recently been developed for solid mechanics (Steigmann and Ogden 1999a). Effectively, the term in the second integral in Eq.(2.3) takes into account the current area of the material boundary $z = 0$. Now from the constitutive assumptions in Eq.(2.3), we find that $\boldsymbol{\sigma}$, the Cauchy stress tensor corresponding to the large deformation in Eq.(2.1) is given by

$$\boldsymbol{\sigma} = \mu\mathbf{B} - p\mathbf{I}, \quad (2.4)$$

Applying the condition that the boundary at $z = 0$ is traction-free fixes the value of the hydrostatic pressure as $p = \mu$.

Straightforward calculations reveal that the principal stretches of the deformation field in Eq.(2.1) are λ_k ($k = 1, 2, 3$) given by (Destrade and Ogden 2005)

$$\lambda_1 \pm \lambda_2 = \sqrt{(\lambda_{\text{res}} \pm \lambda_{\text{res}}^{-1})^2 + K^2\lambda_{\text{res}}^{-2}}, \quad \lambda_3 = 1, \quad (2.5)$$

and that the Eulerian principal axes (x_1, x_2) are obtained after an anti-clockwise rotation of angle ϕ of the in-plane coordinate axes about the z axis, where

$$\tan(2\phi) = \frac{2\lambda_{\text{res}}^{-2}K}{\lambda_{\text{res}}^2 - \lambda_{\text{res}}^{-2}(1 - K^2)}. \quad (2.6)$$

Using Eq.(2.5), we note that

$$\lambda_2 = \lambda_1^{-1} \implies K = \lambda_{\text{res}} \sqrt{(\lambda_1 - \lambda_1^{-1})^2 - (\lambda_{\text{res}} - \lambda_{\text{res}}^{-1})^2}. \quad (2.7)$$

We now look for a perturbation solution in the neighbourhood of the large deformation (2.1), using the theory of incremental deformations (Ogden 1997). Hence we call $\mathbf{u} = \mathbf{u}(x_1, x_2, x_3)$ the incremental displacement field, for which the incremental incompressibility condition imposes that

$$u_{i,i} = 0. \quad (2.8)$$

The constitutive equation for the components of the incremental nominal stress $\dot{\mathbf{S}}$ reads in general as (Ogden 1997),

$$\dot{S}_{ji} = L_{jikl} u_{k,l} + p u_{i,j} - \dot{p} \delta_{ji}, \quad (2.9)$$

where \dot{p} is the increment in p , and \mathbf{L} is the fourth-order tensor of instantaneous moduli, defined by

$$L_{jikl} = \frac{\partial^2 W_V}{\partial F_{ja} \partial F_{kb}} F_{ia} F_{lb}, \quad (2.10)$$

where W_V is the strain-energy per unit volume.

In the absence of body forces, we can therefore write the equilibrium equation of the incremental nominal stress $\dot{\mathbf{S}}$ as

$$(\text{div } \dot{\mathbf{S}})_i = \dot{S}_{ji,j} = 0. \quad (2.11)$$

In the case of a neo-Hookean material $W_V = \mu/2(\text{tr } \mathbf{B} - 3)$, Eq. (2.10) becomes $L_{jikl} = \mu \delta_{jk} B_{il}$ so that Eq.(2.11) in the coordinate system aligned with the Eulerian principal axes takes the following simplified form

$$-\dot{p}_{,1} + \mu \lambda_1^2 u_{1,ii} = 0, \quad -\dot{p}_{,2} + \mu \lambda_2^2 u_{2,ii} = 0, \quad -\dot{p}_{,3} + \mu \lambda_3^2 u_{3,ii} = 0, \quad (2.12)$$

Differentiating these incremental equilibrium equations with respect to x_1 , x_2 , and x_3 , respectively, and using the incremental incompressibility condition in Eq.(2.8), we find that

$$\nabla^2 \dot{p} = 0, \quad (2.13)$$

that is, the incremental Lagrange multiplier is a Laplacian field (Flavin 1963).

Now, for the incremental *boundary conditions*, we consider that the bottom $z = x_3 = -H$ of the layer is fixed (clamped condition):

$$u_i(x_1, x_2, -H) = 0, \quad (2.14)$$

while the top face $z = x_3 = 0$ remains free of incremental traction (which can be derived from Eq. (4.21)₃ or Eq. (4.34) in Steigmann and Ogden 1999b):

$$u_{1,3} + u_{3,1} = 0, \quad u_{2,3} + u_{3,2} = 0, \quad -\dot{p} + 2\mu u_{3,3} - \gamma(u_{3,11} + u_{3,22}) = 0. \quad (2.15)$$

We search for solutions to Eqs.(2.8,2.12,2.13) in the following form:

$$\{u_1, u_2, u_3, \dot{p}\} = \{U_1(x_3), U_2(x_3), U_3(x_3), ikP(x_3)\} e^{ik(\cos\theta x_1 + \sin\theta x_2)}, \quad (2.16)$$

corresponding to the occurrence of plane wrinkles with wavenumber k , forming an angle θ with the direction of maximum extension, which is the principal direction associated with λ_1 . It is easy to show that a solution in the form of Eq.(2.16) is given by (Flavin 1963)

$$\begin{aligned} U_1(x_3) &= \cos\theta (a_1 e^{-kx_3} + a_2 e^{-qkx_3} + a_3 e^{kx_3} + a_4 e^{qkx_3}), \\ U_2(x_3) &= \sin\theta (a_1 e^{-kx_3} + a_2 e^{-qkx_3} + a_3 e^{kx_3} + a_4 e^{qkx_3}), \\ U_3(x_3) &= i (a_1 e^{-kx_3} + a_2 e^{-qkx_3}/q - a_3 e^{kx_3} - a_4 e^{qkx_3}/q), \\ P(x_3) &= -\mu(1 - q^2) (a_1 e^{-kx_3} + a_3 e^{kx_3}), \end{aligned} \quad (2.17)$$

where a_1, a_2, a_3, a_4 are constants, and q is fixed by imposing Eqs.(2.12), as

$$q = \sqrt{\lambda_1^2 \cos^2\theta + \lambda_1^{-2} \sin^2\theta}. \quad (2.18)$$

Using Eqs.(2.17), it is easy to check that only four independent boundary conditions result from Eqs.(2.14) and (2.15). Setting $\mathbf{a} = [a_1, a_2, a_3, a_4]^T$ they can be written in the following matrix form:

$$\mathbf{Q}\mathbf{a} = \mathbf{0}, \quad (2.19)$$

where the matrix \mathbf{Q} reads :

$$\mathbf{Q} = \begin{bmatrix} 2q & 1 + q^2 & -2q & -1 - q^2 \\ q(-1 - q^2 + kL_{\text{cap}}) & -2q + kL_{\text{cap}} & q(-1 - q^2 - kL_{\text{cap}}) & -2q - kL_{\text{cap}} \\ e^{kH} & e^{qkH} & e^{-kH} & e^{-qkH} \\ e^{kH} & e^{qkH}/q & -e^{-kH} & -e^{-qkH}/q \end{bmatrix}. \quad (2.20)$$

Here $L_{\text{cap}} := \gamma/\mu$ is the *characteristic capillary length* of the material. The resulting condition for the wrinkling instability is $\det \mathbf{Q} = 0$. After lengthy manipulations not reproduced here, it is possible to show that the earliest onset of instability occurs at $\theta = 0$ that is, when the wrinkles are aligned with the direction where the greatest stretch, λ_1 , occurs. There, $q = \lambda_1$, and the *dispersion relation* reduces to

$$\begin{aligned} kL_{\text{cap}}(\lambda_1^2 - 1) [\cosh(kH) \sinh(\lambda_1 kH) - \lambda_1 \sinh(kH) \cosh(\lambda_1 kH)] \\ + 4\lambda_1(\lambda_1^2 + 1) - \lambda_1(5 + 2\lambda_1^2 + \lambda_1^4) \cosh(kH) \cosh(\lambda_1 kH) \\ + (1 + 6\lambda_1^2 + \lambda_1^4) \sinh(kH) \sinh(\lambda_1 kH) = 0. \end{aligned} \quad (2.21)$$

This dispersive bifurcation criterion is the main result of this section, linking the material (L_{cap}) and geometrical (λ_{res} and K appearing inside the expression for λ_1 in Eq.(2.5)) parameters describing the sheared layer, to the wavelength of the expected wrinkles (through the non-dimensional quantity $kH = 2\pi H/\ell$, where ℓ is the wrinkles' wavelength).



Figure 2.2: Anecdotal evidence suggests that shearing the forearm skin along the lines of cleavage (which run along the length of the arm) results in later onset of small-amplitude wrinkles than when shearing across, compare with Figure 2.1.

In Figure 2.3 we show the separate influences of the pre-stretch and of the surface tension. We plot the critical amount of shear K^* , at which wrinkles occur, against H/ℓ , the ratio of the layer's thickness to the wrinkles' wavelength. We find that as H/ℓ becomes small, K^* increases rapidly, showing that the layer is more and more stable: that is because for a thin slab, the clamped boundary condition at the bottom takes precedence and prevents the appearance of wrinkles. As soon as the layer's thickness becomes comparable to the wrinkles' wavelength ($H/\ell > 1$), the value of the critical amount of shear tends rapidly to its value for a semi-infinite solid (surface instability). On Figure 2.3 (left), we study the influence of λ_{res} in the absence of surface tension ($L_{\text{cap}} = 0$). We see that K^* is increased when $\lambda_{\text{res}} > 1$ and decreased when $\lambda_{\text{res}} < 1$. In other words, shearing along the direction of tension requires a greater amount of shear than shearing along the direction of compression, consistent with experimental observations, see Figure 2.2. On Figure 2.3 (right), we investigate the influence of surface tension ($L_{\text{cap}} > 0$) in the absence of pre-stretch ($\lambda_{\text{res}} = 1$). We see that as L_{cap} increases, K^* also increases, indicating that surface tension makes the layer more stable. This would be consistent with the observation that young skin does not wrinkle as early as older skin when sheared, because it is tauter.

Owing to the rapid settling of the dispersion curves to their half-space (Biot) instability limit, we now take $kH \gg 1$ in Eq.(2.21), while keeping $kL_{\text{cap}} = 2\pi L_{\text{cap}}/\ell$ finite. It then reduces to

$$2\pi(L_{\text{cap}}/\ell)(\lambda_1 + 1) + (\lambda_1^3 + \lambda_1^2 + 3\lambda_1 - 1) = 0. \quad (2.22)$$

To check for consistency, we make the link with known results. For instance, when we neglect the capillary energy in Eq.(2.22) by taking $L_{\text{cap}} = 0$, we recover the surface instability criterion of plane strain (Destradé et al. 2008),

$$\lambda_2 = \frac{3(13+3\sqrt{33})^{1/3}}{2^{1/3}(13+3\sqrt{33})^{2/3}-2^{8/3}-(13+3\sqrt{33})^{1/3}} \simeq 3.3830. \quad (2.23)$$

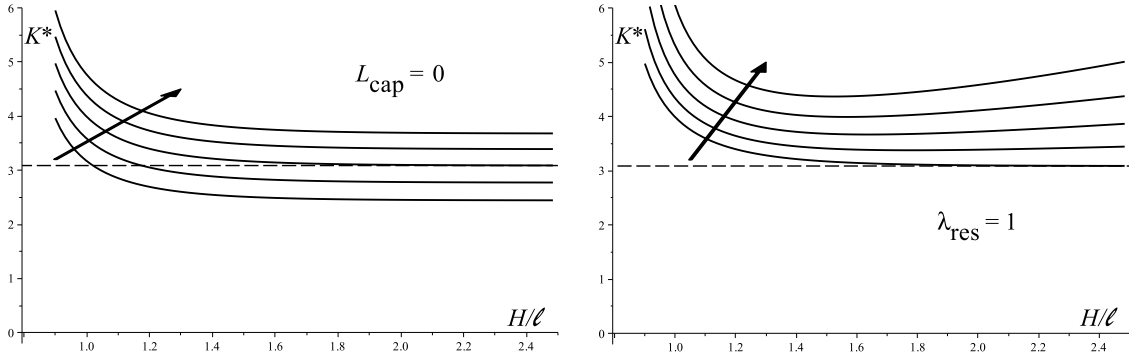


Figure 2.3: Left: In the absence of surface tension ($L_{\text{cap}} = 0$), the layer becomes more (less) stable when sheared in the direction of tension (compression). Here $\lambda_{\text{res}} = 0.8, 0.9, 1.0, 1.1, 1.2$. Right: In the absence of pre-stretch ($\lambda_{\text{res}} = 1$), the layer becomes more stable in shear when its top surface is endowed with a surface tension. Here $L_{\text{cap}}/H = 0.0, 0.005, 0.01, 0.015, 0.02, 0.025$. The horizontal line indicates the shear threshold of surface instability $K^* = 3.0873$ in an unstretched half-space without surface tension.

The corresponding *shear threshold* K^* is found by using Eq.(2.7), as

$$K^* = \lambda_{\text{res}} \sqrt{\frac{2^{11/3} 3^{2/3}}{3(9+\sqrt{33})^{1/3}} + \frac{4(45+6\sqrt{33})^{1/3}}{3} - (\lambda_{\text{res}} - \lambda_{\text{res}}^{-1})^2} \simeq \lambda_{\text{res}} \sqrt{(3.0873)^2 - (\lambda_{\text{res}} - \lambda_{\text{res}}^{-1})^2}. \quad (2.24)$$

Here the value $K^* = 3.0873$, obtained in the absence of a pre-stretch ($\lambda_{\text{res}} = 1$), corresponds to the shear threshold of surface instability for a neo-Hookean half-space as found both theoretically by Destrade et al. 2008 and experimentally by Mora et al. 2011. Figure 2.4 confirms the trends found from the exact dispersion equation. Hence the left figure (based on Eq.(2.24)) shows that the shear threshold K^* is enhanced (half-space is more stable) by the presence of a tensile pre-stretch and vice-versa for a compressive pre-stretch (in tension, K^* eventually reaches a maximum of 5.68 at $\lambda_{\text{rs}} \simeq 2.40$, but this is way beyond the elastic limit of skin). Similarly, the effect of surface tension is to increase the stretchability of the half-space before it becomes unstable, as shown by the right figure (based on Eq.(2.22)).

In the presence of surface tension the critical shear K^* is maintained larger than the critical shear for an unstretched halfspace, as already discussed for the surface instability of compressed skin tissues (Ciarletta and Ben Amar 2012). If $L_{\text{cap}}/H \ll 1$, in particular, a logarithmic correction can be calculated via a series expansion of Eq.(2.21)

$$K = K^* + \beta(\lambda_{\text{res}}) \frac{L_{\text{cap}}}{H} \log \left[\alpha(\lambda_{\text{res}}) \frac{H}{L_{\text{cap}}} \right], \quad kH = \frac{1}{2} \log \left[\alpha(\lambda_{\text{res}}) \frac{H}{L_{\text{cap}}} \right], \quad (2.25)$$

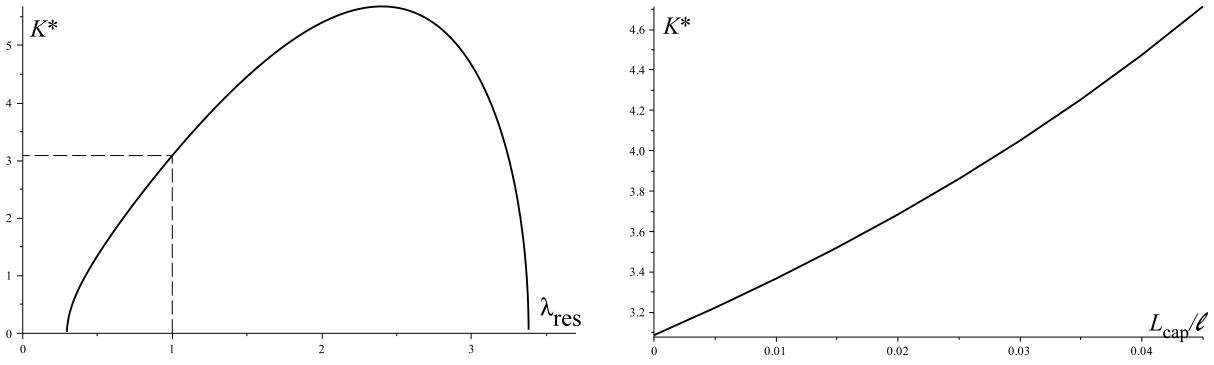


Figure 2.4: Stability of a semi-infinite neo-Hookean half-space subject to a pre-stretch followed by a simple shear. Left: In the absence of surface tension $L_{\text{cap}} = 0$, the stability under shear is enhanced by a tensile pre-stretch ($\lambda_{\text{res}} > 1$) and decreased by a compressive pre-stretch ($\lambda_{\text{res}} < 1$). The dotted lines correspond to the shear threshold with no pre-stretch ($\lambda_{\text{res}} = 1$, $K^* = 3.0873$). Right: The presence of surface tension ($L_{\text{cap}} > 0$) leads to a larger shear being required before the instability criterion is met.

with

$$\alpha(\lambda_{\text{res}}) = \lambda_{\text{res}}(-0.0289 + 0.0025(\lambda_{\text{res}} + \lambda_{\text{res}}^{-2})), \quad (2.26)$$

$$\beta(\lambda_{\text{res}}) = 0.388\lambda_{\text{res}}\sqrt{9.351 - (\lambda_{\text{res}} + \lambda_{\text{res}}^{-2})^2}. \quad (2.27)$$

Finally, we have found that the presence of a surface tension, or capillary energy, always stabilizes the free surface in the sense that a large critical shear is necessary to form wrinkles.

2.3 Shear instability of a fibre-reinforced skin tissue

The dermis of human skin is characterised by a structural arrangement of elastin and collagen type I fibres in the extracellular matrix, leading to an anisotropic stiffening of the tissue. The aim of this section is to investigate how such material anisotropy affects the stability of sheared skin.

Let us consider a single family of fibres oriented, in the reference configuration, in the direction of the unit vector $\mathbf{M} = [\cos \alpha, \sin \alpha, 0]^T$, defining the structural tensor $\widehat{\mathbf{M}} = \mathbf{M} \otimes \mathbf{M}$ so that $\lambda_\alpha := (\mathbf{C} : \widehat{\mathbf{M}})^{\frac{1}{2}}$ represents the fibre stretch. In order to build a strain measure for the fibres, we introduce the structural invariant I_α , defined as follows:

$$I_\alpha = [\mathbf{C} + \mathbf{C}^{-1} - 2\mathbf{I}] : \widehat{\mathbf{M}}. \quad (2.28)$$

As discussed by Ciarletta et al. (2011), this choice provides a physically consistent deformation measure when $\lambda_\alpha \rightarrow +\infty$ and when $\lambda_\alpha \rightarrow 0$, thereby accounting for both compression and extension of the fibres. Accordingly, the strain energy

density of the skin tissue is defined as:

$$w = \frac{\mu}{2}(I_1 - 3) + \beta I_\alpha, \quad (2.29)$$

where $\beta > 0$ is the anisotropic elastic modulus of the fibres. The constitutive relation Eq.(2.29) ensures strong-ellipticity of the tissue in planar deformations, a characteristic which is not met for example for the so-called standard model of fibre reinforcement chosen by Destrade et al. (2008). It is a simple exercise to show that for a small tensile strain along the direction of the fibres, we have $\lambda_1 = \lambda_\alpha = 1 + \epsilon$, where $|\epsilon| \ll 1$ for the tensile stretch and $\lambda_2 = \lambda_3 = 1 - \epsilon/2$ for the lateral stretches; then, the resulting infinitesimal stress is $\sigma_1 = 4\mu\epsilon + 8\beta\epsilon$, showing that (at least in the linear regime) the ratio $2\beta/\mu$ is a measure of the stiffness of the fibres compared to the stiffness of the matrix.

We set $\lambda_{\text{res}} = 1$ in this section for the sake of simplicity, so that the half-space is subject to *simple shear* only,

$$x = X + KY, \quad y = Y, \quad z = Z, \quad (2.30)$$

with deformation gradient and principal stretches

$$\mathbf{F} = \begin{bmatrix} 1 & K & 0 \\ 0 & 1 & 0 \\ 0 & 0 & 1 \end{bmatrix}, \quad \lambda_{1,2} = \pm \frac{K}{2} + \sqrt{1 + \frac{K^2}{4}}, \quad \lambda_3 = 1, \quad (2.31)$$

respectively. Substituting \mathbf{F} in Eq.(2.28) we see that $I_\alpha = K^2$, which means that the strain-energy w is independent of the fibre orientation. The corresponding Cauchy stress tensor does depend on fibre orientation, as follows

$$\boldsymbol{\sigma} = \mu(\mathbf{B} - \mathbf{I}) + 2\beta(\mathbf{F}\mathbf{M} \otimes \mathbf{F}\mathbf{M} - \mathbf{F}^{-T}\mathbf{M} \otimes \mathbf{F}^{-T}\mathbf{M}). \quad (2.32)$$

Let us look for a perturbed surface wave in the form of Eq.(2.16); to do so we need the components of the instantaneous moduli tensor L in Eq.(2.9). For the anisotropic strain energy density w defined in Eq.(2.29) and \mathbf{F} given in Eq.(2.31) we find the components

$$L_{jikl} = \mu\delta_{jk}B_{il} + 2\beta \left(M_p M_q \delta_{jk} F_{lp} F_{iq} + M_p M_q \delta_{jl} F_{pk}^{-1} F_{qi}^{-1} + M_p M_q \delta_{il} F_{pk}^{-1} F_{qj}^{-1} + M_p M_q \delta_{ik} F_{pj}^{-1} F_{ql}^{-1} \right), \quad (2.33)$$

in the coordinate system aligned with the directions of simple shear x , y , z (see Appendix for explicit expressions). Then we take the incremental quantities to be of the form

$$\{u_j, \dot{S}_{3j}, \dot{p}\} = \{U_j(kz), ik S_{3j}(kz), ik P(kz)\} e^{ik(\cos\theta x + \sin\theta y)}, \quad (2.34)$$

where the amplitudes are functions of only (kz) . By a well established procedure we can use Eqs.(2.8-2.11) to eliminate P and write the incremental equations as a first-order differential system known as the *Stroh formulation*,

$$\boldsymbol{\eta}' = i\mathbf{N}\boldsymbol{\eta} = i \begin{bmatrix} \mathbf{N}_1 & \mathbf{N}_2 \\ \mathbf{N}_3 & \mathbf{N}_1^T \end{bmatrix} \boldsymbol{\eta}, \quad \text{with } \boldsymbol{\eta} := [U_1, U_2, U_3, S_{31}, S_{32}, S_{33}]^T, \quad (2.35)$$

where the prime denotes differentiation with respect to the function argument. Here it transpires that the blocks \mathbf{N}_1 , \mathbf{N}_2 and \mathbf{N}_3 are symmetric (explicit expressions are given in the Appendix).

All is in place now for a complete resolution of the surface instability problem. There exist many strategies for this resolution, see a partial list and references in Destrade et al. (2008). Here we adopted a straightforward approach, because it turned out to be tractable numerically. Noticing that the Stroh matrix \mathbf{N} is constant, a solution of the system Eq.(2.35) has the form

$$\boldsymbol{\eta} = \boldsymbol{\eta}_0 e^{ikqz} \quad \text{with} \quad \boldsymbol{\eta}_0 := [\mathbf{U}_0, \mathbf{S}_0]^T, \quad (2.36)$$

where $\boldsymbol{\eta}_0$ is a constant vector and q are the eigenvalues of \mathbf{N} . In order for the wrinkles' amplitude to decay with depth, we retain the three roots q_1 , q_2 , q_3 with positive imaginary part (i.e. $\text{Im}(q) > 0$). This gives the following general solution,

$$\boldsymbol{\eta}(kz) = c_1 \boldsymbol{\eta}_1 e^{ikq_1 z} + c_2 \boldsymbol{\eta}_2 e^{ikq_2 z} + c_3 \boldsymbol{\eta}_3 e^{ikq_3 z} = \begin{bmatrix} \mathbf{A} \\ \mathbf{B} \end{bmatrix} \begin{bmatrix} c_1 \\ c_2 \\ c_3 \end{bmatrix}, \quad (2.37)$$

where c_1 , c_2 , c_3 are constants, and \mathbf{A} , \mathbf{B} are square (3×3) matrices built from the eigenvectors $\boldsymbol{\eta}_i$ ($i = 1, 2, 3$), taken proportional to any column vector of the matrix adjoint to $(\mathbf{N} - q_i \mathbf{I})$. Now, the traction-free boundary condition at $z = 0$ can be written as :

$$\mathbf{S}_0 = \begin{bmatrix} S_{31}(0) \\ S_{32}(0) \\ S_{33}(0) \end{bmatrix} = \mathbf{Z} \begin{bmatrix} U_1(0) \\ U_2(0) \\ U_3(0) \end{bmatrix} = \mathbf{Z} \mathbf{U}_0 = \mathbf{0}, \quad (2.38)$$

where $\mathbf{Z} := -i\mathbf{B}\mathbf{A}^{-1}$ is the surface impedance matrix. The condition for the onset of a surface instability is thus

$$\det \mathbf{Z} = 0. \quad (2.39)$$

As we do not know *a priori* in which directions the wrinkles are to appear for a given angle α of the fibres with respect to the direction of shear, we need to span the entire plane and find the angle θ^* for which the corresponding amount of shear K^* is minimal, indicating the earliest onset of wrinkling. This is the main difference of instability behaviour between an isotropic material (such as the material in the previous section), where the wrinkles appear *aligned* with a principal direction of pre-deformation, and an anisotropic material, where the wrinkles may be *oblique* with respect to the direction of least stretch.

For our simulations, we chose material constants such that $2\beta/\mu = 0$ (matrix alone), 0.5 (matrix stiffer than fibres), 1.0 (matrix as stiff as fibres), and 2.0 (matrix softer than fibres). For each choice of $2\beta/\mu$ we found K^* and θ^* as functions of α . Varying the angle α can be interpreted as either varying orientation of the fibres for a shear that occurs along a fixed axis, such as the y -axis in Eq.(2.30), or as varying the axis along which shear is taking place for a fixed fibre direction α . For illustrative purposes, a typical surface buckling solution is depicted in Figure 2.6, where we chose $2\beta/\mu = 1$ (fibres are twice as stiff as the matrix in the linear

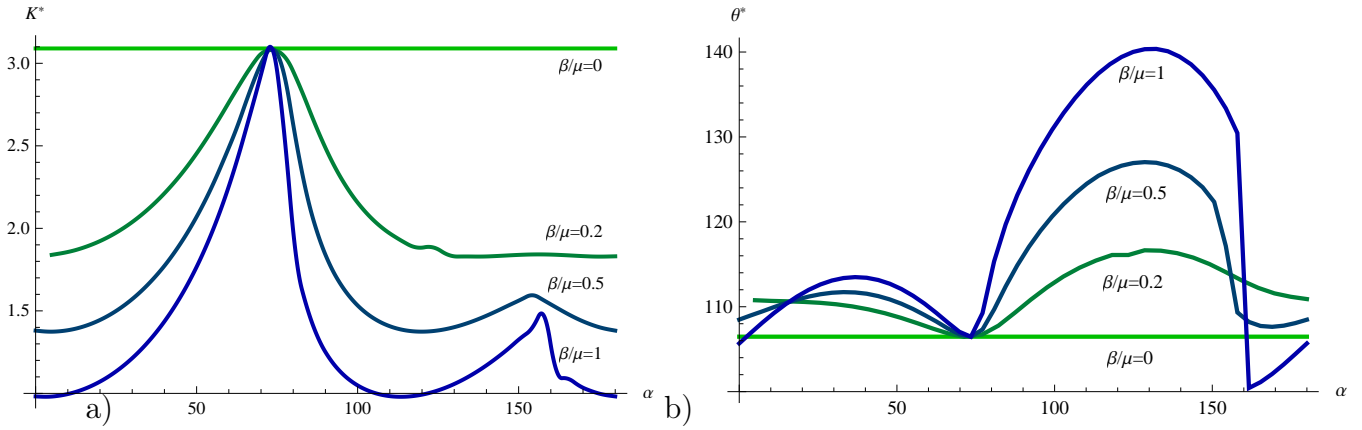


Figure 2.5: (a) The critical shear strain K^* as a function of the reference fibre angle α : The presence of fibres clearly leads to earlier surface instability in shear. (b) The critical instability angle θ^* as a function of the reference fibre angle α : These results are harder to interpret because θ^* is defined in the current configuration and α in the reference configuration. A remapping of the variations of K^* and θ^* with the current fibre angle is shown in Figure 2.8.

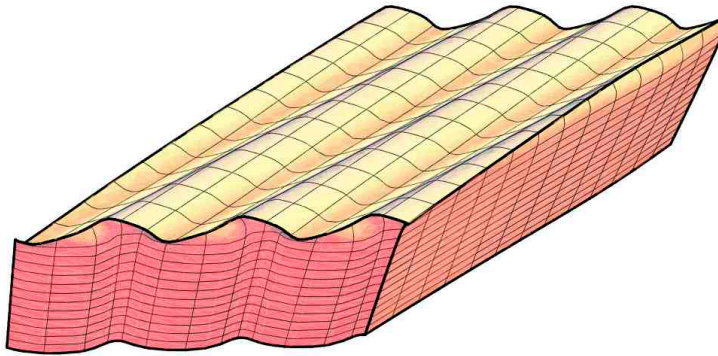


Figure 2.6: When $2\beta/\mu = 2.0$ (fibres are twice as stiff as the matrix in the linear regime) and $\alpha = 84.5^\circ$ (fibres are almost at a right angle to the direction of shear), the first wrinkles appear when the amount of shear reaches $K^* = 1.51$, and the corresponding angle of the wrinkles with respect to the direction of shear is $\theta^* = 115.2^\circ$. Note the decay of the wrinkles' amplitude with depth.

regime) and $\alpha = 84.5^\circ$ (fibres are originally almost at a right angle to the direction of shear): there, according to Figure 2.5, we have $K^* = 1.51$ and $\theta^* = 115.2^\circ$.

To set the stage for analyzing the results in Figure 2.5, we note that the first wrinkles to appear will be those that require the least energy. When the half-space is sheared, line elements are compressed in certain directions and elongated in oth-

ers. The effect of superposing a small-amplitude wrinkle is to elongate the material along the direction of the wrinkle front incrementally, i.e. in the direction θ given by Eq.(2.34), while there is no incremental stretch in the direction orthogonal to the wavefront, see Figure 2.7(a). In the neo-Hookean isotropic case ($\beta = 0$), the

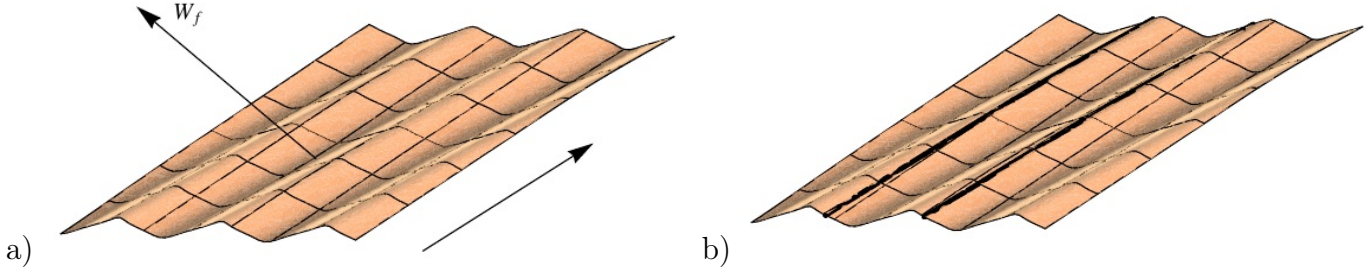


Figure 2.7: a) The wavefront of the wrinkle is indicated by the vector \mathbf{W}_f . Along the wavefront the material is elongated incrementally, orthogonal to it the material is neither elongated nor compressed. b) The fibres are shown by bold black lines.

wavefront is aligned with the direction of greatest compression: hence, wrinkling always elongates the material in a direction that was under compression due to the shear, and thus allows the material to release some potential energy. In the anisotropic case ($\beta \neq 0$), the presence of fibres alters the direction θ^* of the least energy wavefront, because elongating or compressing fibres greatly increases the potential energy, and thus wrinkles aligned with the fibre direction can substantially decrease the potential energy. For instance, Figure 2.7(b) depicts the fibre orientation for the solution in the previous figures, showing that the wrinkles produce an incremental elongation in a direction which was under compression in the simple shear configuration, while they leave the fibres almost unstretched.

Clearly, the *current* direction of the fibres (in the deformed state of finite simple shear) is closely linked to the value to the wavefront orientation θ^* . To study this relationship we re-examine the data in Figure 2.5 by mapping α to the fibre orientation in the deformed body α^* , that is the angle between the spatial vector \mathbf{FM} of the current fibre orientation and the x -axis, from which θ^* is also measured. The results of this remapping are shown in Figure 2.8.

We first turn our attention to the plots of K^* against α^* , see Figure 2.8(a). On the dashed lines, the fibres are neither compressed or stretched. The (almost straight) continuous black lines S_α and C_α indicate when the fibres are aligned with the directions of greatest stretch and greatest compression, respectively. They are given by the equations

$$\alpha^* = \tan^{-1}(\lambda_1), \quad \alpha^* = \tan^{-1}(\lambda_2), \quad (2.40)$$

respectively, where the λ s are given in Eq.(2.31) and evaluated at $K = K^*$. The S_α curve helps us elucidate why there exists a point (denoted p_C) where all anisotropic materials become unstable in shear at the same threshold shear $K^* \simeq 3.0873$ as in an isotropic neo-Hookean material (where $\beta = 0$): clearly, this phenomenon occurs when the shear is such that the fibres become aligned with the direction of

greatest stretch. Then, it turns out that great simplifications occur in the Stroh formulation of the instability problem, and that the buckling criterion coincides with that of the neo-Hookean model, see proof in the Appendix. This is an artefact of our specific choice of strain energy density in Eq.(2.29).

In Figure 2.8(b), which shows plots of θ^* against α^* , we drew the line $\theta^* = \alpha^* - 90^\circ$. Clearly, in a region close to p_C , the wavefront is almost aligned with the direction of greatest stretch, as is the case in an isotropic neo-Hookean material. As β/μ increases, the neighborhood of this alignment widens, indicating that the stiffer the fibres are, the closer the instability curves in Figure 2.8(b) will be to the line $\theta^* = \alpha^* - 90^\circ$ so as not to further stretch the already extended fibres.

The overall general conclusion is that stiffer fibres lead to earlier onset of instability, notwithstanding the punctual fixing of all curves at point p_C , due to our specific choice of a neo-Hookean isotropic matrix. This result is in agreement with the casual observation that old skin (presumably with stiffer collagen bundles) wrinkles earlier than young skin when pinched.

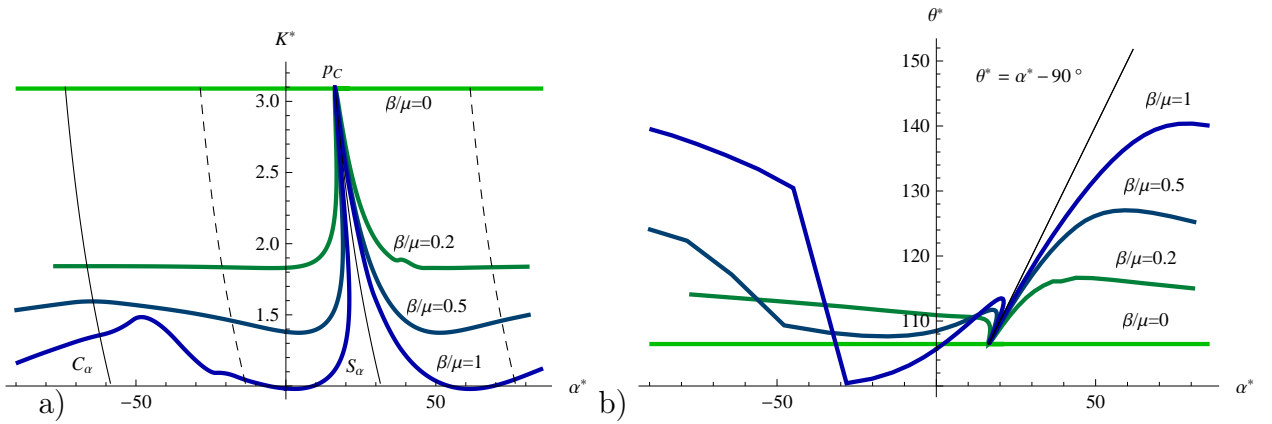


Figure 2.8: (a) The critical shear strain K^* as a function of the current angle α^* the fibres make with respect to the direction of shear. (b) The critical instability angle θ^* as a function of α^* . The point p_C indicates a surface instability state common to all materials (independent of the material parameters).

2.4 Discussion and Conclusion

In this work we have investigated the occurrence of shear instability in skin tissue within the framework of nonlinear elastic theories.

In Section 2.2, we have considered the skin tissue as a neo-Hookean layer of finite thickness, whilst the epidermis is modelled as a surface tension. Moreover, we have taken into account the presence of the cleavage lines of skin as preferred direction of residual stretches inside the tissue. Under these assumptions, a linear stability analysis has been performed using the method of incremental elastic deformations, and an analytical form of the dispersion relation has been reported in Eq.(2.21). The results demonstrate that the presence of surface tension makes the layer more

stable, in the sense that it needs to be sheared more for wrinkles to develop than when surface tension is absent (Figure 2.3(a)). Furthermore, the capillary energy fixes the surface instability wavelength at threshold at a finite value, as depicted in Figure 2.3(b). We have also found that wrinkles appear earlier when the shear takes place perpendicular to the direction of pre-stretch than when it occurs along that direction, as confirmed by the anecdotal evidence shown in Figures 2.1 and 2.2.

In Section 2.3, we have investigated the effect of fibre reinforcement in the dermis layer on the shear instability characteristics. For this purpose, we have used the polyconvex strain energy function in Eq.(2.29) for modeling the transverse isotropic reinforcement along a preferential fibre direction. A Stroh formulation of the incremental elastic equations has been derived in Eq.(2.35), and solved numerically using an iterative technique. As shown in Figures 2.5 and 2.8, we have found that the presence of fibres always lowers the shear threshold at which geometrical instability happens: the stiffer the fibres, the earlier the wrinkles appear in shear. Given that anisotropic stiffness of skin greatly increase with ageing (Agache et al. 1980), our results are in agreement with the fact that older skin wrinkles earlier when pinched.

In conclusion, this mathematical study of wrinkle formation in sheared skin confirms that pinching experiments in dermatology are useful tools to evaluate the local mechanical properties of the tissue.

Acknowledgements

Partial funding by the European Community grant ERG-256605, FP7 program, and by the Hardiman Scholarship programme at the National University of Ireland Galway, are gratefully acknowledged by the first and third authors, respectively. We thank R.W. Ogden (Glasgow) for helpful comments and insights, A. Ní Anaidh (Dublin) for pointers in the literature on skin, and J. & E. Guillemette (Galway) for technical assistance.

References

- Agache, P. et al. (1980). “Mechanical properties and Young’s modulus of human skin in vivo”. In: *Archives of dermatological research* 269, 221–232.
- Biot, M. (1963). “Surface instability of rubber in compression”. In: *Appl. Sc. Res.* 12, 168–182.
- Ciarletta, P. and Ben Amar, M. (2012). “Papillary networks in the dermal–epidermal junction of skin: a biomechanical model”. In: *Mechanics Research Communications* 42, 68–76.
- Ciarletta, P. et al. (2011). “Stiffening by fiber reinforcement in soft materials: a hyperelastic theory at large strains and its application”. In: *Journal of the mechanical behavior of biomedical materials* 4, 1359–1368.

- Cox, H. (1941). “The cleavage lines of the skin”. In: *British Journal of Surgery* 29, 234–240.
- Destrade, M. and Ogden, R. W. (2005). “Surface waves in a stretched and sheared incompressible elastic material”. In: *International Journal of Non-Linear Mechanics* 40, 241–253.
- Destrade, M. et al. (2008). “Surface instability of sheared soft tissues”. In: *Journal of biomechanical engineering* 130, 061007.
- Flavin, J. (1963). “Surface waves in pre-stressed Mooney material”. In: *The Quarterly Journal of Mechanics and Applied Mathematics* 16, 441–449.
- Kraissl, C. J. (1951). “The selection of appropriate lines for elective surgical incisions.” In: *Plastic and Reconstructive Surgery* 8, 1–28.
- Lautrup, B. (2005). “Physics of continuous matter”. In: *Bristol, UK: Institute of Physics Publishing*.
- Mora, S. et al. (2011). “Surface instability of soft solids under strain”. In: *Soft Matter* 7, 10612–10619.
- Ogden, R. W. (1997). *Non-linear elastic deformations*. Dover.
- Steigmann, D. J. and Ogden, R. W. (1999a). “Elastic surface—substrate interactions”. In: *Proceedings of the Royal Society of London A: Mathematical, Physical and Engineering Sciences* 455, 437–474.
- Steigmann, D. and Ogden, R. (1997). “Plane deformations of elastic solids with intrinsic boundary elasticity”. In: *Proc. R. Soc. A* 453, 853–877.
- (1999b). “Elastic surface—substrate interactions”. In: *Proceedings of the Royal Society of London A: Mathematical, Physical and Engineering Sciences* 455, 437–474.
- Waldorf, J. C., Perdakis, G., and Terkonda, S. P. (2002). “Planning incisions”. In: *Operative Techniques in General Surgery* 4, 199–206.

Appendix

For an incompressible anisotropic material with strain energy density w given in Eq.(2.29), there are 31 non-zero instantaneous moduli in the coordinate system aligned with the directions of simple shear x , y , z in Eq.(2.30). They are found

from Eq.(2.33) as follows.

$$\begin{aligned}
L_{1111} &= \mu(1 + K^2) + 2\beta(4 \cos^2 \alpha + 2K \cos \alpha \sin \alpha + K^2 \sin^2 \alpha), \\
L_{1112} &= L_{1211} = L_{2122} = L_{2221} = 4\beta \cos \alpha(\sin \alpha - K \cos \alpha), \\
L_{1121} &= L_{1222} = L_{2111} = L_{2212} = \mu K + 2\beta(\sin 2\alpha - K \cos 2\alpha), \\
L_{1212} &= (\mu + 2\beta)(1 + K^2), \\
L_{1221} &= L_{2112} = 2\beta(1 - 2K \cos \alpha \sin \alpha + K^2 \cos^2 \alpha), \\
L_{1313} &= \mu(1 + K^2) + 2\beta(\cos \alpha + K \sin \alpha)^2, \\
L_{1323} &= L_{2313} = \mu K + 2\beta \sin \alpha(\cos \alpha + K \sin \alpha)^2, \\
L_{1331} &= L_{3113} = 2\beta \cos^2 \alpha, \\
L_{1332} &= L_{2331} = L_{3123} = L_{3132} = L_{3213} = L_{3231} = 2\beta \cos \alpha(\sin \alpha - K \cos \alpha), \\
L_{2121} &= \mu + 2\beta, \\
L_{2222} &= \mu + 2\beta(4 \sin^2 \alpha - 6K \cos \alpha \sin \alpha + 3K^2 \cos^2 \alpha), \\
L_{2323} &= \mu + 2\beta \sin^2 \alpha, \\
L_{2332} &= L_{3223} = 2\beta(\sin \alpha - K \cos \alpha)^2, \\
L_{3131} &= \mu + 2\beta \cos^2 \alpha, \\
L_{3232} &= \mu + 2\beta(\sin \alpha - K \cos \alpha)^2, \\
L_{3333} &= \mu.
\end{aligned}$$

The symmetric blocks \mathbf{N}_1 , \mathbf{N}_2 , and \mathbf{N}_3 of the corresponding Stroh matrix \mathbf{N} are given by

$$-\mathbf{N}_1 = \begin{bmatrix} 0 & 0 & \cos \theta \\ 0 & 0 & \sin \theta \\ \cos \theta & \sin \theta & 0 \end{bmatrix}, \quad \mathbf{N}_2 = \frac{1}{\Delta} \begin{bmatrix} L_{3232} & -L_{1332} & 0 \\ -L_{1332} & L_{3131} & 0 \\ 0 & 0 & 0 \end{bmatrix}, \quad -\mathbf{N}_3 = \begin{bmatrix} \eta & \kappa & 0 \\ \kappa & \nu & 0 \\ 0 & 0 & \chi \end{bmatrix},$$

respectively, with

$$\begin{aligned}
\Delta &= L_{3232}L_{3131} - L_{1332}^2 = \mu [\mu + 2\beta(1 - 2K \cos \alpha \sin \alpha + K^2 \cos^2 \alpha)], \\
\eta &= (3\mu + L_{1111}) \cos^2 \theta + 2L_{1121} \cos \theta \sin \theta + L_{2121} \sin^2 \theta, \\
\kappa &= L_{1112} + (3\mu + L_{1221}) \cos \theta \sin \theta, \\
\nu &= L_{1212} \cos^2 \theta + 2L_{1121} \cos \theta \sin \theta + (3\mu + L_{2222}) \sin^2 \theta, \\
\chi &= [\mu \sin 2\alpha + 2\beta(\sin 2\alpha + \sin 2\theta)] K + [\mu \cos^2 \theta + 2\beta(\cos^2 \theta - \cos^2 \alpha)] K^2.
\end{aligned}$$

Tremendous simplifications occur when L and \mathbf{N} are expressed in the coordinate system aligned with the Lagrangian principal axes and the fibres are aligned with the direction of greatest stretch λ_1 . Then, for wrinkles aligned with that direction,

we find that the Stroh matrix reads

$$\mathbf{N} = \begin{bmatrix} 0 & 0 & 0 & \frac{\lambda_1^2}{\mu\lambda_1^2 + 2\beta} & 0 & 0 \\ 0 & 0 & -1 & 0 & \frac{1}{\mu} & 0 \\ 0 & -1 & 0 & 0 & 0 & 0 \\ -\frac{\mu + 2\beta}{\lambda_1^2} & 0 & 0 & 0 & 0 & 0 \\ 0 & -\frac{\mu(1 + 3\lambda_1^2)}{\lambda_1^2} & 0 & 0 & 0 & -1 \\ 0 & 0 & \frac{\mu(\lambda_1^2 - 1)}{\lambda_1^2} & 0 & -1 & 0 \end{bmatrix}.$$

It clearly shows that the incremental deformation in the plane of shear is uncoupled from the out-of-plane component. Further, the in-plane components do not involve β and are identical to the components of the Stroh matrix for an isotropic neo-Hookean material. It follows that these wrinkles appear at the critical amount of shear $K_{\text{cr}} \simeq 3.0873$ found by Destrade et al. (2008), independently of the value of β . The corresponding value for the largest stretch is $\lambda_1 = K_{\text{cr}}/2 + \sqrt{1 + K_{\text{cr}}^2/4} \simeq 3.3830$ and the angle of the fibres in the reference configuration is $\alpha_{\text{cr}} = \tan^{-1}(\lambda_1) \simeq 1.283 \text{ rad} = 73.53^\circ$.

Chapter 3

Counter-intuitive results in acousto-elasticity

Artur L. Gower^{*}, Michel Destrade^{*†} and R. W. Ogden[‡]

Abstract

We present examples of body wave and surface wave propagation in deformed solids where the slowest and the fastest waves do not travel along the directions of least and greatest stretch, respectively. These results run counter to commonly accepted theory, practice, and implementation of the principles of acousto-elasticity in initially isotropic solids. For instance, we find that in nickel and steel the fastest waves are along the direction of greatest compression, not greatest extension (and vice-versa for the slowest waves), as soon as those solids are deformed. Further, we find that when some materials are subject to a small-but-finite deformation, other extrema of wave speeds appear in non-principal directions. Examples include nickel, steel, polystyrene, and a certain hydrogel. The existence of these “oblique”, non-principal extremal waves complicates the protocols for the non-destructive determination of the directions of extreme strains.

3.1 Introduction

The determination of the direction of greatest tension in a deformed solid is one of the main goals of acoustic non-destructive evaluation because, for isotropic solids, this direction coincides with the direction of greatest stress. Consider for instance

[‡]School of Mathematics and Statistics, University of Glasgow, Scotland

[†]School of Mechanical & Materials Engineering,
University College Dublin, Belfield, Dublin 4, Ireland

^{*}School of Mathematics, Statistics and Applied Mathematics,
National University of Ireland Galway, University Road, Galway, Ireland

cutting through a membrane under uniaxial tension: cutting parallel to the direction of the tensile force produces a thin cut, while cutting across produces a gaping cut (see Figure 3.1), which can have serious consequences in scarring outcomes after stabbing incidents or surgery. Finding the direction of greatest stress is also important in geophysics, oil prospecting (Guyer and Johnson 2009) and structural health monitoring and evaluation (Pao 1984; Kim and Sachse 2000).



Figure 3.1: Cutting through pig skin: a clamped sample of pig skin is put under tension, after 3 cuts have been performed, parallel (top), oblique (center) and perpendicular (bottom) to the tensile force.

In this paper we investigate the propagation of small-amplitude elastic waves in the body (body acoustic waves – BAWs) and on the surface (surface acoustic waves – SAWs) of a deformed solid, and determine the dependence of their speeds on the angle of propagation with respect to the principal directions of pre-strain. It is widely thought that surface waves propagate at their fastest in the direction of greatest stretch and at their slowest in a perpendicular direction, along the direction of least stretch. This view is supported by intuition and often forms the basis of a non-destructive determination of these directions.

However, the coupling of acoustics and elasticity is a *non-linear phenomenon* even at its lowest order, and it can thus generate counter-intuitive results. The first such result is that for some materials, the fastest wave travels along the direction of greatest compression (and conversely, the slowest wave along the direction of greatest extension). It has been known for some time that a compression in one direction could indeed result in an increase in the speed of a principal wave instead of the intuitively expected decrease, and Hughes and Kelly (1953) showed experimentally that body wave speeds increase with hydrostatic pressure for polystyrene (see their Figure 3); similar experimental results exist for body waves in railroad steel and surface waves in mild steel; see Kim and Sachse (2000) for a review. Here we extend those results to the consideration of non-principal waves in deformed steel and nickel, and to pre-strains resulting in turn from the application of a uniaxial

stress and of a pure shear stress.

The other counter-intuitive result is that the following statement by Kim and Sachse (2000) is not necessarily true: “The principal stress direction is found where the variations of the SAW speeds show symmetry about the direction”. Indeed, Tanuma et al. (2012) recently showed that for a small-amplitude SAW traveling in the symmetry plane of a transversely isotropic solid, subject to a small pre-strain, the correction to the wave speed due to the pre-stress has sinusoidal variations with respect to the angle of propagation, in line with that statement. Explicitly, Tanuma et al. (2012) established the following expression for the correction to the Rayleigh wave speed v_R^0 when the solid is subject to a pre-stress with principal components σ_1, σ_2 in the plane boundary:

$$v_R = v_R^0 + A(\sigma_1 + \sigma_2) + B(\sigma_1 - \sigma_2) \cos 2\psi,$$

where A and B are acousto-elastic coefficients, and ψ is the angle between the direction of propagation and one of the principal directions of pre-stress. However, their result is only true when the pre-stress and accompanying pre-strain are infinitesimal. Here we show that the variations can rapidly lose their sinusoidal regularity beyond that regime, even when a solid is deformed by as little as 1%. Since in non-destructive evaluation and structural health monitoring, the order of magnitude of the pre-stress is not known *a priori*, we conclude that a complete theoretical and numerical investigation needs to be conducted (as here) prior to the determination of the sought-after principal directions. They will not be found simply by measuring the wave speed in all directions until a symmetry in variation is found.

The paper is organized as follows. In the next section we recall the equations governing the propagation of small-amplitude waves in solids subject to a pre-strain of arbitrary magnitude. For the constitutive modelling, we focus on isotropic solids with a strain-energy density expressed as a polynomial expansion up to third order in terms of invariants of the Green strain tensor. Historically, this is the framework in which the equations of *acousto-elasticity* have often been written in considering elastic wave propagation in a slightly pre-deformed, initially isotropic solid. We refer to, for example, Pao (1984) and Kim and Sachse (2000) for an exposition of the practical and theoretical aspects of this technique, which can be dated back to the early efforts of Brillouin (1925) and Hughes and Kelly (1953); see also Destradre and Ogden (2012) for a review of acousto-elasticity in solids subject to a general homogeneous pre-strain (not necessarily of infinitesimal amplitude). In Sections 3.3 and 3.5, we study body wave and surface wave propagation, respectively (the latter is more complicated than the former, and we thus devote Section 3.4 to a description of our numerical strategy). For both types of waves we uncover examples of solids (steel, Pyrex glass, polystyrene, nickel, hydrogel with a hard core) where the wave speed does not have its greatest value along the direction of greatest stretch, and/or can be extremal along directions which are *oblique* to the directions of the principal stretches. These counter-intuitive results seem to have gone unnoticed before.

3.2 Governing equations

3.2.1 Incremental motions

In this paper we are concerned with the propagation of small-amplitude waves in deformed materials. The equations governing their motion are now well established. Consider a homogeneous elastic solid, held in a state of static homogeneous deformation, which has brought a material point which was at \mathbf{X} in the reference configuration to position $\mathbf{x} = \mathbf{x}(\mathbf{X}, t)$ in the current configuration.

Let (X'_1, X'_2, X'_3) be the coordinates of \mathbf{X} with respect to fixed rectangular Cartesian unit basis vectors $(\mathbf{e}'_1, \mathbf{e}'_2, \mathbf{e}'_3)$, and let a pure homogeneous strain be defined by

$$x'_1 = \lambda_1 X'_1, \quad x'_2 = \lambda_2 X'_2, \quad x'_3 = \lambda_3 X'_3, \quad (3.1)$$

with respect to the same basis, where the positive constants $\lambda_1, \lambda_2, \lambda_3$ are the *principal stretches* of the deformation. Now consider the material to be a half-space occupying the region $x'_2 \geq 0$ so that the boundary $x'_2 = 0$ is a principal plane of deformation, which we take to be free of traction. Now choose a second set of unit basis vectors $(\mathbf{e}_1, \mathbf{e}_2, \mathbf{e}_3)$, say, with coordinates (x_1, x_2, x_3) , so that $x_2 = x'_2$ and the direction of \mathbf{e}_1 makes an angle θ with the direction of \mathbf{e}'_1 . Then

$$\begin{bmatrix} x_1 \\ x_2 \\ x_3 \end{bmatrix} = \begin{bmatrix} \cos \theta & 0 & \sin \theta \\ 0 & 1 & 0 \\ -\sin \theta & 0 & \cos \theta \end{bmatrix} \begin{bmatrix} x'_1 \\ x'_2 \\ x'_3 \end{bmatrix}. \quad (3.2)$$

A small-amplitude wave traveling in this material is described by the associated mechanical displacement field $\mathbf{u} = \mathbf{u}(\mathbf{x}, t)$, satisfying, in the coordinate system (x_1, x_2, x_3) , the incremental equations of motion (Ogden 1997),

$$\rho u_{i,tt} = s_{pi,p} = \mathcal{A}_{0piqj} u_{j,pq}, \quad (3.3)$$

where $s_{pi} = \mathcal{A}_{0piqj} u_{j,q}$ are the components of the incremental nominal stress tensor, and \mathcal{A}_{0piqj} are components of the fourth-order tensor of instantaneous moduli \mathcal{A}_0 (to be detailed later), a comma followed by an index i (or t) denotes partial differentiation with respect to x_i , $i = 1, 2, 3$, (or t) and ρ is the current mass density. We specialise the analysis to waves that propagate in the x_1 direction, with amplitude variations in the x_2 direction. Hence we seek solutions of the form

$$\mathbf{u} = \mathbf{U}(x_2) e^{ik(x_1 - vt)}, \quad (3.4)$$

where \mathbf{U} , the amplitude, is a function of x_2 only, k is the wavenumber, and v is the wave speed. Then the equations of motion reduce to

$$\mathbf{T}\mathbf{U}''(x_2) + ik(\mathbf{R} + \mathbf{R}^T)\mathbf{U}'(x_2) - k^2(\mathbf{Q} - \rho v^2 \mathbf{I})\mathbf{U}(x_2) = \mathbf{0}, \quad (3.5)$$

where the constant tensors \mathbf{T} , \mathbf{R} , \mathbf{Q} are defined in terms of their components with respect to the basis $(\mathbf{e}_1, \mathbf{e}_2, \mathbf{e}_3)$ by

$$T_{ij} = T_{ji} = \mathcal{A}_{02i2j}, \quad R_{ij} = \mathcal{A}_{02i1j}, \quad Q_{ij} = Q_{ji} = \mathcal{A}_{01i1j}, \quad (3.6)$$

\mathbf{I} is the identity tensor, and the exponent T denotes the transpose.

Without loss of generality, we take $\lambda_1 < \lambda_2 < \lambda_3$, so that $\theta = 0^\circ$ corresponds to the direction of greatest compression and $\theta = 90^\circ$ to the direction of greatest stretch. In the coordinate system (x'_1, x'_2, x'_3) aligned with the principal axes of deformation, there are only 15 non-zero components of \mathcal{A}_0 , given by (Ogden 1997)

$$\begin{aligned} \mathcal{A}'_{0iijj} &= J^{-1} \lambda_i \lambda_j W_{ij}, \\ \mathcal{A}'_{0ijji} &= J^{-1} (\lambda_i W_i - \lambda_j W_j) \lambda_i^2 / (\lambda_i^2 - \lambda_j^2), & i \neq j, \lambda_i \neq \lambda_j, \\ \mathcal{A}'_{0ijji} &= J^{-1} (\lambda_j W_i - \lambda_i W_j) \lambda_i \lambda_j / (\lambda_i^2 - \lambda_j^2), & i \neq j, \lambda_i \neq \lambda_j, \\ \mathcal{A}'_{0ijji} &= J^{-1} (\lambda_i^2 W_{ii} - \lambda_i \lambda_j W_{ij} + \lambda_i W_i) / 2, & i \neq j, \lambda_i = \lambda_j, \\ \mathcal{A}'_{0ijji} &= J^{-1} (\lambda_i^2 W_{ii} - \lambda_i \lambda_j W_{ij} - \lambda_i W_i) / 2, & i \neq j, \lambda_i = \lambda_j, \end{aligned} \quad (3.7)$$

where $J = \lambda_1 \lambda_2 \lambda_3$ is the dilatation, W is the strain energy density, $W_i = \partial W / \partial \lambda_i$, $W_{ij} = \partial^2 W / \partial \lambda_i \partial \lambda_j$ and there is no sum on repeated indices. In the coordinate system (x_1, x_2, x_3) , the components of \mathcal{A}_0 , required to compute the tensors in (4.22), are given by

$$\mathcal{A}_{0ijkl} = \Omega_{ip} \Omega_{jq} \Omega_{kr} \Omega_{ls} \mathcal{A}'_{0pqrs}, \quad (3.8)$$

where Ω_{ij} is the rotation matrix corresponding to a rotation through the angle θ about $x_2 = x'_2$.

We say that \mathcal{A}_0 satisfies the *strong-convexity* condition (S-C) when

$$\mathcal{A}_{0ijkl} \xi_{ij} \xi_{kl} > 0 \quad \text{for all non-zero tensors } \boldsymbol{\xi}, \quad (3.9)$$

but we remark that this condition does not hold in general, only in the region of deformation space corresponding to dead-load stability (see, for example, Ogden (1997)). The *strong-ellipticity* condition (S-E) reads

$$\mathcal{A}_{0ijkl} n_i n_k m_j m_l > 0 \quad \text{for all non-zero vectors } \mathbf{n} \text{ and } \mathbf{m}, \quad (3.10)$$

and is implied by strong convexity.

3.2.2 Deformed materials

For the constitutive modelling of the pre-deformed materials, we focus on general isotropic compressible elastic solids, with a third-order expansion of the strain-energy density in powers of the Green strain tensor \mathbf{E} , specifically

$$W = \frac{\lambda_0}{2} i_1^2 + \mu_0 i_2 + \frac{A}{3} i_3 + B i_1 i_2 + \frac{C}{3} i_1^3, \quad (3.11)$$

where

$$i_k = \text{tr}(\mathbf{E}^k) = \frac{1}{2^k} \left[(\lambda_1^2 - 1)^k + (\lambda_2^2 - 1)^k + (\lambda_3^2 - 1)^k \right], \quad k = 1, 2, 3. \quad (3.12)$$

Here, λ_0 and μ_0 are the Lamé coefficients of second-order elasticity and A, B, C are the Landau coefficients of third-order elasticity (Landau et al. 1986).

Material	Units	λ_0	μ_0	A	B	C
Nickel	10^5 bars	7.8	6.12857	-73	-22.5	17.9
Steel	10^5 bars	8.1	5.4	-76	-25	-9
Polystyrene	10^5 bars	0.2889	1.381	-1.00	-0.830	-1.06
Pyrex Glass	10^5 bars	2.75	5.583	42	71	-69.6
Hydrogel	NkT	4595	1184	-2737	-1682.5	-3762.5

Table 3.1: Second- and third-order elastic constants for six different materials.

For our examples, we use material parameters taken from the literature for nickel (Lurie and Belyaev 2005), steel (Lurie and Belyaev 2005), polystyrene (Hughes and Kelly 1953), Pyrex glass (Lurie and Belyaev 2005), and a certain hydrogel with a hard core (Wu and Kirchner 2010), all summarised in Table 1.

We look at two types of pre-deformations: first, that due to a uniaxial stress and second that due to a pure shear stress. A *uniaxial pre-stress* in the \mathbf{e}'_1 direction is due to a Cauchy stress for which the only non-zero component is $\sigma_{11} = T$, say. It leads to an equibiaxial pre-deformation, with corresponding principal stretches

$$\lambda_1 = \lambda, \quad \lambda_2 = \lambda_3. \quad (3.13)$$

Here λ is linked to the compressive stress T through the equation $T = J^{-1}\lambda_1\partial W/\partial\lambda_1$, whilst λ_2 is found in terms of λ by solving

$$0 = \partial W/\partial\lambda_2. \quad (3.14)$$

With our choice (3.11) of strain energy density, this turns out to be a quadratic in λ_2^2 .

A *pure shear stress* is applied parallel to the plane of the boundary so that the only non-zero Cauchy stress component is $\sigma_{13} = S$, say. The corresponding pre-deformation is a combination of simple shear in the x_3 direction and a triaxial stretch (Mihai and Goriely 2011; Destrade et al. 2012). Here it is a simple exercise to check (see, for example, Lurie and Belyaev (2005)) that the principal stresses are $S, 0, -S$, and that the corresponding principal directions of stress are along $(1, 0, 1), (0, 1, 0), (1, 0, -1)$, respectively. The principal directions of strain are aligned with these directions, and the principal stretches are found by solving the system

$$S = J^{-1}\lambda_1\partial W/\partial\lambda_1, \quad 0 = \partial W/\partial\lambda_2, \quad -S = J^{-1}\lambda_3\partial W/\partial\lambda_3, \quad (3.15)$$

for $\lambda_1 = \lambda, \lambda_2$ and λ_3 .

The range of realistic values for λ is restricted by the existence of a solution of the system of equations (3.13) and (3.14) for uniaxial compression, and of the equations in (3.15) for pure shear stress. There is a great variability of this feasible range for λ from one material to another. For example, steel can only be sheared for λ from 1 down to 0.935, below which value there are no real solutions, while for the hydrogel there exists a pure shear stress solution for deformations of at least 40%. We further restrict our range of admissible λ 's by assuming that the

materials are subject to uniaxial compressive stresses or pure shear stresses only within the region where S and T are monotonic functions of λ . This ensures that our results belong to a physically valid regime.

3.3 Results for body waves

For homogeneous *body* waves, there are no boundary conditions to satisfy and no amplitude variation to consider. Hence we take

$$\mathbf{U}(x_2) = \mathbf{U}_0, \quad (3.16)$$

a constant vector, in the governing equation (3.5), resulting in the eigenvalue problem

$$(\mathbf{Q} - \rho v^2 \mathbf{I})\mathbf{U}_0 = \mathbf{0}, \quad (3.17)$$

with associated characteristic equation $\det(\mathbf{Q} - \rho v^2 \mathbf{I}) = 0$, a cubic in ρv^2 .

For the body waves traveling along the principal direction corresponding to the least principal stretch λ_1 , i.e. $\theta = 0^\circ$, we find the three roots

$$\rho v^2 = \mathcal{A}'_{01111}, \mathcal{A}'_{01212}, \mathcal{A}'_{01313}, \quad (3.18)$$

and similarly for the body waves along the principal direction corresponding to the largest stretch ratio λ_3 , i.e. $\theta = 90^\circ$,

$$\rho v^2 = \mathcal{A}'_{03333}, \mathcal{A}'_{03131}, \mathcal{A}'_{03232}. \quad (3.19)$$

In each set of three roots for ρv^2 , the first root corresponds to a pure longitudinal wave and the next two to pure transverse waves.

In general ($\theta \neq 0, 90^\circ$), the characteristic equation factorizes into the product of a term linear in ρv^2 (corresponding to a pure transverse wave polarized along the x_2 direction) and a term quadratic in ρv^2 (with one root corresponding to a pseudo-longitudinal wave and the other to a pseudo-transverse wave); see (Norris 1983) for details.

Figure 3.2 depicts the variations of the three body wave speeds (in this and all subsequent plots it is $v\sqrt{\rho}$ that is plotted) in deformed *nickel* with respect to the angle θ between the direction of greatest compression and the direction of propagation, for different values of compressive stretch under uniaxial and pure shear stresses. The variations of the wave traveling with the intermediate speed meet intuitive expectations: this wave travels at its slowest when $\theta = 0^\circ$ and at its fastest when $\theta = 90^\circ$. However, this scenario is reversed for the fastest and slowest waves, as soon as the solid is deformed: they travel at their fastest along the direction of greatest compression ($\theta = 0^\circ$) and slowest in the orthogonal direction. Moreover, when a pure shear stress induces a compression of more than 3%, we notice that the profile for the slowest body wave develops a new minimum; in effect this wave travels at its slowest in a direction which is *oblique* with respect to the principal directions of strain ($\theta \simeq 50^\circ$).

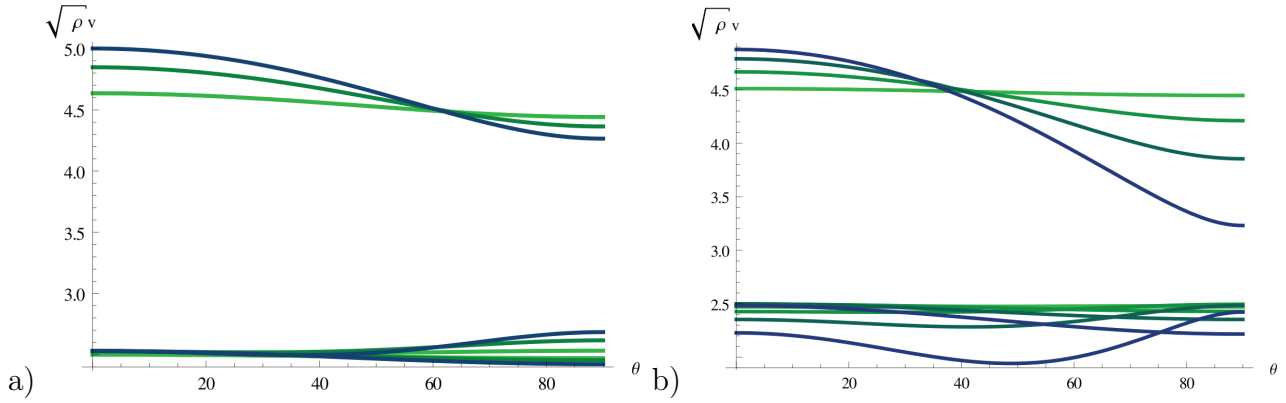


Figure 3.2: The three body-wave speed profiles (plotted as $v\sqrt{\rho}$) for nickel under (a) uniaxial compressive stress with principal compression stretch ratio $\lambda = 0.99$ (light green curve), 0.973 (blue-green curve), 0.956 (blue curve); (b) pure shear stress with $\lambda = 0.99$ (light green curve), 0.978 (blue-green curve) and 0.967 (blue curve). The curves at the top of the graph are the longitudinal waves while the other curves are transverse waves.

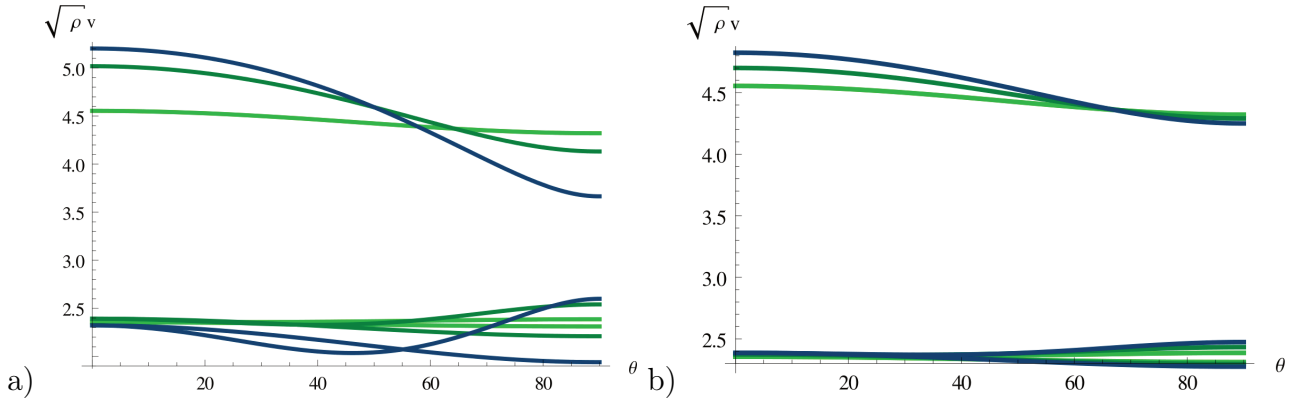


Figure 3.3: The three body-wave speed profiles (plotted as $v\sqrt{\rho}$) for steel under (a) uniaxial compressive stress with $\lambda = 0.99$ (light green curve), 0.956 (blue-green curve), 0.922 (blue curve); (b) pure shear stress with $\lambda = 0.99$ (light green curve), 0.981 (blue-green curve), 0.973 (blue curve). The curves at the top of the graph are the longitudinal waves while the other curves are transverse waves.

Figure 3.3 shows the corresponding results for deformed *steel*. They are similar to those for deformed nickel, with the difference that the secondary minimum phenomenon occurs under uniaxial compression instead of pure shear stress.

In Figures 3.4 and 3.5, we study body wave propagation in deformed *polystyrene* and *hydrogel*. Here the waves all travel at their fastest along the direction of greatest stretch ($\theta = 90^\circ$) and two of the three waves travel at their slowest in the direction of greatest compression ($\theta = 0^\circ$). There is, however, one wave which travels at its slowest in an oblique direction, for both types of pre-deformations (due to uniaxial stress: figures on the left; due to pure shear stress: figures on the right). They appear at quite large compressions (31% for polystyrene, 39% for

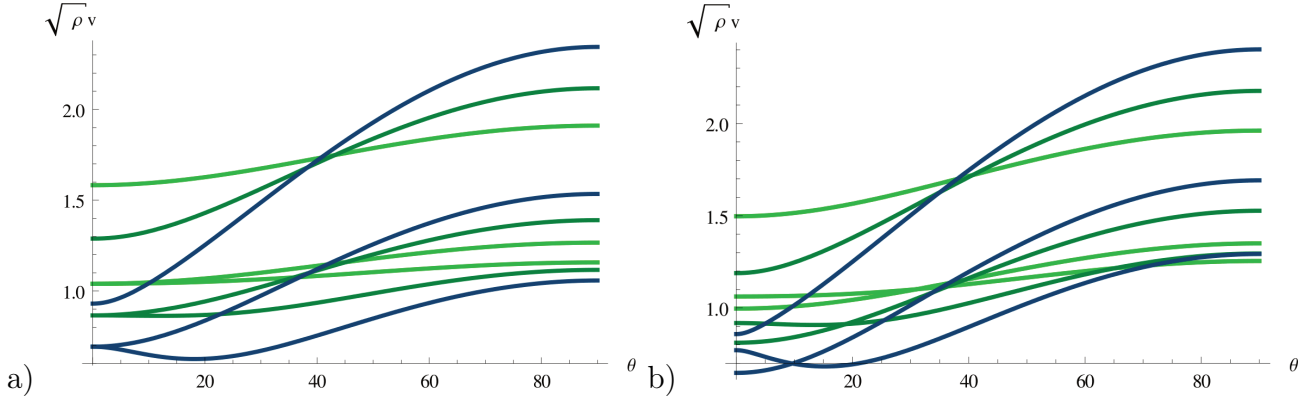


Figure 3.4: The three body-wave speed profiles (plotted as $v\sqrt{\rho}$) for polystyrene under (a) uniaxial compressive stress; (b) pure shear stress. The light green curves correspond to $\lambda = 0.91$, the blue-green curves to $\lambda = 0.8$, and the blue curves to $\lambda = 0.69$. The curves at the top of the graph are the longitudinal waves while the other curves are transverse waves.

hydrogel), which are nonetheless compatible with the soft nature of these solids and with a physically acceptable material response (i.e. the tension and the shear stress are monotonic functions of the stretch).

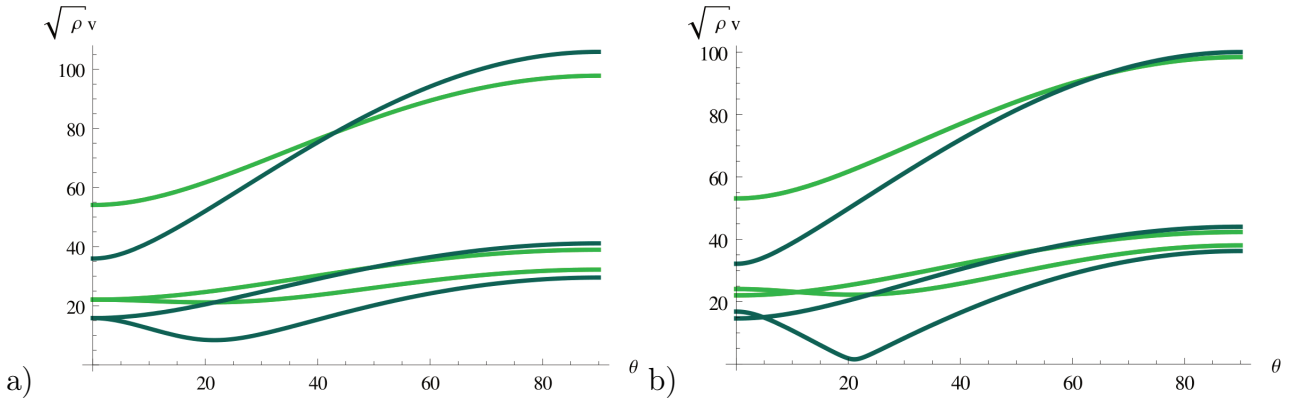


Figure 3.5: The three body-wave speed profiles (plotted as $v\sqrt{\rho}$) for hydrogel under (a) uniaxial compressive stress; (b) pure shear stress. The light green curves correspond to $\lambda = 0.75$ (i.e. 25% maximum compression) and the dark green curves to $\lambda = 0.61$ (i.e. 39% maximum compression). The curves at the top of the graph are the longitudinal waves while the other curves are transverse waves.

Now we investigate non-principal *surface* wave propagation in a deformed homogeneous half-space. There are several methods of resolution available for these problems (Rogerson and Sandiford 1999; Destrade et al. 2005; Kayestha et al. 2011; Gandhi et al. 2012). Here we adopt a formulation in terms of the surface impedance matrix. In the next section we detail the steps involved in implementing this method, based on the analysis of Fu and Mielke (2002).

3.4 The matrix Riccati method for surface waves

In the following, we replace the tensors \mathbf{T} , \mathbf{R} , \mathbf{Q} , etc., introduced in the previous section by their matrix representations with respect to the Cartesian coordinates (x_1, x_2, x_3) . In a nutshell, surface wave propagation is governed by the *algebraic matrix Riccati equation* (Biryukov 1985; Barnett and Lothe 1985; Fu and Mielke 2002; Norris and Shuvalov 2010)

$$\mathbf{0} = [\mathbf{Z}(v) - i\mathbf{R}^T]\mathbf{T}^{-1}[\mathbf{Z}(v) + i\mathbf{R}] - \mathbf{Q} + \rho v^2 \mathbf{1}, \quad (3.20)$$

the radiation condition,

$$\text{Im Spec } \mathbf{T}^{-1}[i\mathbf{Z}(v) - \mathbf{R}] > 0, \quad (3.21)$$

and the boundary condition of zero incremental traction on $x_2 = 0$, which is equivalent to

$$\det \mathbf{Z}(v) = 0. \quad (3.22)$$

Here, the constant 3×3 matrix $\mathbf{Z}(v)$ is the so-called *surface impedance matrix*. For a given v , $\mathbf{Z}(v)$ is a constant Hermitian matrix, of the form

$$\mathbf{Z} = \begin{bmatrix} Z_1 & Z_4 + iZ_5 & Z_6 - iZ_7 \\ Z_4 - iZ_5 & Z_2 & Z_8 + iZ_9 \\ Z_6 + iZ_7 & Z_8 - iZ_9 & Z_3 \end{bmatrix}, \quad (3.23)$$

say, where the Z_k are real constants ($k = 1, \dots, 9$). The algebraic matrix Riccati equation (3.20) is itself Hermitian, and thus corresponds to 9 real equations. Coupling it to (3.22) gives a system of 10 equations for the 10 unknowns Z_k and v , and uniqueness of the solution comes from further requiring that $\mathbf{Z}(v)$ be *positive definite*, as discussed below.

The surface impedance matrix $\mathbf{Z}(v)$ in a half-space relates the incremental displacement \mathbf{u} to the incremental traction \mathbf{t} on the surface $x_2 = \text{constant}$ through the relationship,

$$\mathbf{t} = -k\mathbf{Z}(v)\mathbf{u}. \quad (3.24)$$

We may rewrite this by noting that the general solution of the homogeneous system of second-order ordinary differential equations with constant coefficients (3.5) for the half-space, is of the form $\mathbf{U} = e^{ik\mathbf{E}(v)x_2}\mathbf{U}_0$, where $\mathbf{E}(v)$ is a constant 3×3 matrix (not to be confused with the Green strain) and \mathbf{U}_0 is a constant vector. Then the traction is given by

$$t_i = s_{2i} = \mathcal{A}_{02iqj}u_{j,q}, \quad \text{or} \quad \mathbf{t} = ik[\mathbf{R} + \mathbf{TE}(v)]\mathbf{u}. \quad (3.25)$$

Now write $\mathbf{t} = -ik\mathbf{V}e^{i(kx_1 - vt)}$, where $\mathbf{V} = -[\mathbf{R} + \mathbf{TE}(v)]\mathbf{U}$, so that the impedance relation (3.25) reads

$$\mathbf{V} = -i\mathbf{Z}(v)\mathbf{U}, \quad \text{with} \quad \mathbf{Z}(v) = -i[\mathbf{R} + \mathbf{TE}(v)], \quad (3.26)$$

showing that $\mathbf{Z}(v)$ is indeed a constant matrix for a half-space. The matrix $\mathbf{Z}(v)$ corresponding to the existence of a surface wave is the one that satisfies the Riccati equation (3.20), the boundary condition (3.22), and

$$\text{Im Spec } \mathbf{E}(v) > 0,$$

or, equivalently, (3.21). This condition guarantees the correct decay for $\mathbf{U}(x_2) = e^{ik\mathbf{E}(v)x_2}\mathbf{U}_0$ as x_2 increases with distance away from the free surface.

In the matrix Riccati method, at least two remarkable properties emerge: $\mathbf{Z}(0)$ is positive definite in the region of stability and $\partial\mathbf{Z}(v)/\partial v$ is negative definite as long as $\text{Im Spec } \mathbf{T}^{-1}[\mathbf{i}\mathbf{Z}(v) - \mathbf{R}] > 0$. Hence, $\det \mathbf{Z}(v)$ is positive at $v = 0$ and monotonically decreasing as v increases, which means that it is simple to find \tilde{v} numerically such that $\det \mathbf{Z}(\tilde{v}) = 0$. Moreover uniqueness of the surface velocity, calculated by this procedure, is guaranteed. Barnett and Lothe (1985), Fu and Mielke (2002) and Mielke and Fu (2004) have shown these properties, and here we present a somewhat simpler alternative demonstration (see also Shuvalov et al. (2004) and Alshits and Maugin (2005) for further impedance formulations).

Recall that the incremental nominal stress has components $s_{pi} = \mathcal{A}_{0piqj}u_{j,q}$ (with respect to the non-principal axes) and that the balance of momentum (4.14) reads

$$\rho u_{i,tt} = s_{pi,p}. \quad (3.27)$$

Now multiply both sides of this by u_i^* , the complex conjugate of u_i :

$$\rho u_i^* u_{i,tt} = u_i^* s_{ji,j} = (u_i^* s_{ji})_{,j} - u_{i,j}^* s_{ji} \quad \text{with summation over } i \text{ and } j. \quad (3.28)$$

Then integrate over the region $\mathcal{U} = [x_1, x_1 + \Delta x_1] \times [0, \infty] \times [x_3, x_3 + \Delta x_3]$ in the body, to obtain

$$\int_{\mathcal{U}} \rho u_i^* u_{i,tt} dx_1 dx_2 dx_3 = \int_{\partial\mathcal{U}} u_i^* s_{ji} n_j da - \int_{\mathcal{U}} u_{i,j}^* s_{ji} dx_1 dx_2 dx_3, \quad (3.29)$$

where \mathbf{n} is the outward unit normal vector to the boundary $\partial\mathcal{U}$ and da the associated area element. Now substitute $\mathbf{u}(x_1, x_2, x_3) = \mathbf{U}(x_2)e^{ik(x_1-vt)}$ to arrive at*

$$-k^2 v^2 \int_0^\infty \rho \mathbf{U}^*(y) \cdot \mathbf{U}(y) dy = u_i^* t_i \Big|_{y=0}^{y=\infty} - \int_0^\infty \mathcal{A}_{0jilk} u_{i,j}^* u_{k,l} dy, \quad (3.30)$$

where we have introduced the components t_i , defined in (3.25), of the traction \mathbf{t} on planes normal to the x_2 -axis. Observe that the above equation is independent of x_1 and x_3 . Finally, assume that the wave amplitude decays away from the free surface, so that $\mathbf{U}(\infty) = \mathbf{0}$. Then substitute for t_i from (4.26) and rearrange to obtain

$$k \mathbf{U}^*(0) \cdot \mathbf{Z}(v) \mathbf{U}(0) = \int_0^\infty \mathcal{A}_{0jilk} u_{i,j}^* u_{k,l} dx_2 - k^2 v^2 \int_0^\infty \rho \mathbf{U}^*(x_2) \cdot \mathbf{U}(x_2) dx_2. \quad (3.31)$$

*Here and in the following we write the scalar product of two vectors as $\mathbf{a} \cdot \mathbf{b}$ rather than in the matrix form $\mathbf{a}^T \mathbf{b}$.

Here, only \mathbf{Z} depends on v because (i) \mathbf{U} can be chosen independently of v since for any choice of displacement field \mathbf{U} , a traction field \mathbf{V} can be determined by equation (3.26) such that momentum is balanced, and (ii) v cancels out in the products $u_{i,j}^* u_{l,k}$. Therefore, by differentiating with respect to v , we obtain

$$\mathbf{U}^*(0) \cdot \frac{d\mathbf{Z}(v)}{dv} \mathbf{U}(0) = -2kv \int_0^\infty \rho \mathbf{U}^*(x_2) \cdot \mathbf{U}(x_2) dx_2 < 0, \quad (3.32)$$

while writing equation (3.31) at $v = 0$ gives

$$k \mathbf{U}^*(0) \cdot \mathbf{Z}(0) \mathbf{U}(0) = \int_0^\infty \mathcal{A}_{0jilk} u_{i,j}^* u_{k,l} dx_2, \quad (3.33)$$

for any choice of $\mathbf{U}(0)$. Clearly $d\mathbf{Z}/dv$ is negative definite by (3.32) and, from the strong-convexity condition (3.9) and (3.33), $\mathbf{Z}(0)$ is positive definite if at least one of the components of $u_{i,j}$ is non-zero. Below we show that $\mathbf{Z}(0)$ is positive definite when the deformation is within the region of (dead-load) stability.

For a *material in the reference configuration*, strong convexity is considered to be a necessary physical requirement, and it implies that $\mathbf{Z}(0)$ is positive definite and that the decay condition (3.21) holds at $v = 0$. For a *pre-stressed material*, strong-convexity is not expected in general. However, $\mathbf{Z}(0)$ is positive definite for a deformation in the region of dead-load stability. Let the magnitude of the finite deformation be parameterized by α , with $\alpha = 0$ corresponding to no deformation (for instance, α can be the amount of shear in a simple shear pre-deformation, or the elongation $\lambda - 1$ in a uniaxial stretch). Then the surface-impedance \mathbf{Z} depends on α as well as on v and the boundary condition of no incremental surface-traction (the secular equation) takes the form

$$\det \mathbf{Z}(v, \alpha) = 0. \quad (3.34)$$

Assume that for $\alpha = 0$ the strong-convexity condition (3.9) is satisfied, so that $\mathbf{Z}(0, 0)$ is positive definite. As α is increased and the deformation moves into the region of dead-load stability consider the change in the eigenvalues of $\mathbf{Z}(0, \alpha)$; these eigenvalues are positive until α reaches a critical value α^* , say, when at least one eigenvalue becomes zero and $\det \mathbf{Z}(0, \alpha^*) = 0$. At this point the half-space supports a standing-wave solution given by (3.4) with $v = 0$ (at the boundary of the dead-load stability region), and the material has buckled (that is, it is unstable, at least in the linearized sense). For waves along the principal direction, this buckling criterion can be shown to be the same as found in Dowaikh and Ogden (1991). For $\alpha > \alpha^*$ we say that the half-space is unstable with respect to surface-wave perturbations (Fu and Mielke 2002).

We are only interested in surface waves in the stable region $0 < \alpha < \alpha^*$ where $\mathbf{Z}(0, \alpha)$ is positive definite, and we define an implicit curve $v \rightarrow \mathbf{Z}(v, \alpha)$ by using the Riccati equation (3.20). As long as $\text{Im Spec } \mathbf{T}^{-1}(i\mathbf{Z}(v, \alpha) - \mathbf{R}) > 0$ holds, we increase v until $\det \mathbf{Z}(v, \alpha) = 0$. If along this curve $\text{Im Spec } \mathbf{T}^{-1}(i\mathbf{Z}(v, \alpha) - \mathbf{R}) \leq 0$ before $\det \mathbf{Z}(v, \alpha)$ reaches zero, then there is no surface-wave.

3.5 Results for surface waves

We transform the above analysis into a numerical method by choosing \mathcal{A}_0 for which there is a positive definite $Z(0)$ satisfying equation (3.20). Then, as v is increased, we calculate the implicit curve for $Z(v)$ from $Z(0)$ up to $Z(\hat{v})$ where $\det Z(\hat{v}) = 0$, all the while verifying that $\text{Im Spec } T^{-1}(iZ - R) > 0$. From that point on, we calculate another implicit curve that satisfies equations (3.20) and (3.22) by varying \mathcal{A}_0 (for instance, by varying the angle of propagation with respect to the principal axes or by varying the amplitude of the pre-deformation). If at some point $\text{Im Spec } T^{-1}(iZ - R) \leq 0$, then to confirm that there is no surface-wave calculate the implicit curve for $v \mapsto Z(v)$ that departs from $Z(0)$ and if, for some v , $\text{Im Spec } T^{-1}(iZ(v) - R) \leq 0$, then no surface-wave exists; if not, then varying \mathcal{A}_0 has caused a discontinuous jump in the velocity, which may indeed be possible.

Using this method we now present Surface Acoustic Wave (SAW) velocity profiles in several materials subject to either a uniaxial compressive stress or a pure shear stress, applied in the plane parallel to the free surface $x_2 = 0$.

Figure 3.6 depicts the variations of the surface wave speed with the angle of propagation with respect to the principal directions of strain in *nickel* subject to a uniaxial compressive stress. In the early stages of compression, from 1% to 3% compressive stretch say, “the variations of the SAW speeds show symmetry about the [principal] direction[s]” as stated by Kim and Sachse (2000), with the proviso that the SAW travels at its fastest along the direction of greatest compression $\theta = 0^\circ$ and at its slowest along the direction of greatest stretch $\theta = 90^\circ$ (in line with the behaviour of the body waves in nickel, as shown in the previous section). However, as the material is further compressed (compression beyond 10%), secondary extrema develop: for $\lambda \leq 0.895$, the fastest SAW travels in the $\theta \simeq 65^\circ$ direction and the slowest SAW travels in the $\theta \simeq 45^\circ$ direction. A similar phenomenon occurs when nickel is subject to a pure shear stress, as shown in Figure 3.7: then the slowest wave travels at the oblique angle $\theta \simeq 50^\circ$ when the material is compressed by as little as 3.6%; see figure on the right.

For deformed *steel*, we observe similar characteristics for the SAW velocity profile under uniaxial compression and pure shear stress as for deformed nickel, as shown in Figure 3.8. *Pyrex glass* also exhibits a local minimum under pure shear stress, when $\lambda \simeq 0.975$, which then becomes a global minimum when $\lambda = 0.97$, i.e. under a compression of 3% (figures not shown to save space).

SAWs in deformed *polystyrene* behave in a more orderly way, as they travel at their fastest along the direction of greatest stretch $\theta = 90^\circ$ and at their slowest along $\theta = 0^\circ$, see Figure 3.9. Although the first derivative of the velocity profile is not a monotonic function of the angle, no secondary extremum develops, in contrast to the behaviour of the body waves in the same material (see previous section).

Finally, SAW propagation in deformed *hydrogel* is also almost regular under uniaxial compression even at a relatively large strain (up to 40%); see Figure 3.10(a). However, two secondary extrema develop under pure shear stress, with the secondary minimum in an oblique direction, eventually becoming an absolute mini-

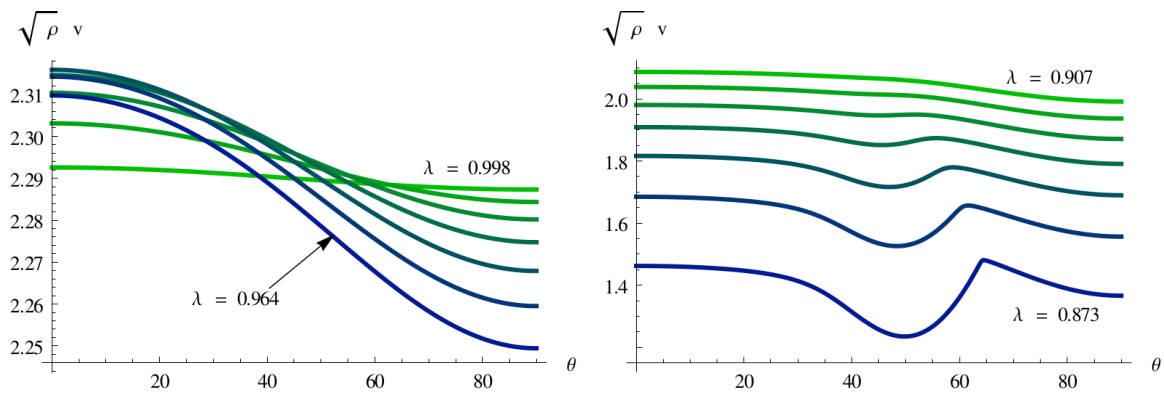


Figure 3.6: Speed profiles for surface waves (plotted as $v\sqrt{\rho}$) in nickel subject to uniaxial compressive stress, with pre-stretch λ decreasing from 0.998 to 0.964 (on the left) and from 0.907 to 0.873 (on the right). As the color of the curves changes from green to blue, λ is decreased by regular increments of 0.0057 from one curve to the next.

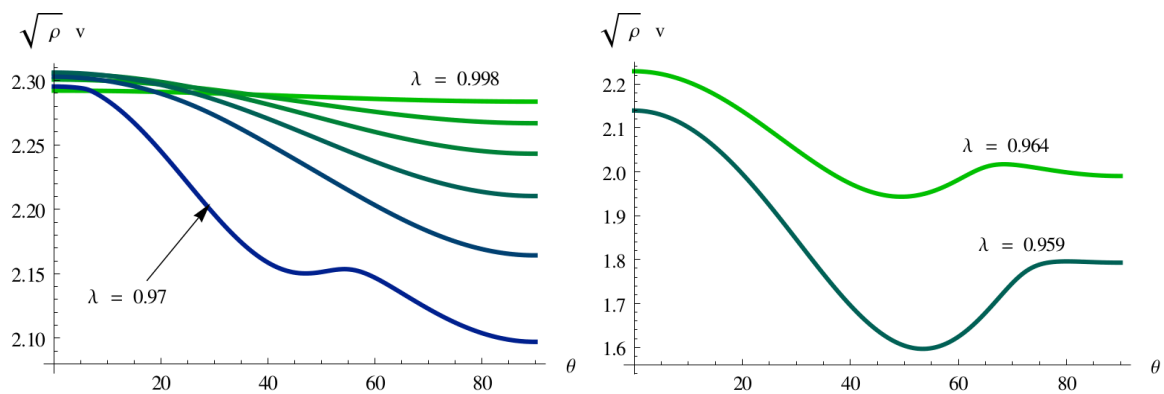


Figure 3.7: Speed profiles for surface waves (plotted as $v\sqrt{\rho}$) in nickel subject to pure shear stress, with pre-stretch λ decreasing from 0.998 to 0.970 (on the left) and from 0.964 to 0.959 (on the right). As the color of the curves changes from green to blue, λ is decreased by regular increments of 0.0057 from one curve to the next.

mum; see Figure 3.10(b).

3.6 Conclusion

Clearly, the existence of oblique slowest waves greatly complicates the determination of the principal directions of strain in a deformed body. Finding the direction where a wave travels at its slowest or fastest is not a guarantee of having determined the direction of greatest compression or tension, or that it is indeed a principal direction. In our examples, we have found that the slowest body wave can sometimes be along an oblique direction and similarly for surface waves. However, we found that the fastest body waves do indeed travel along a principal direction,

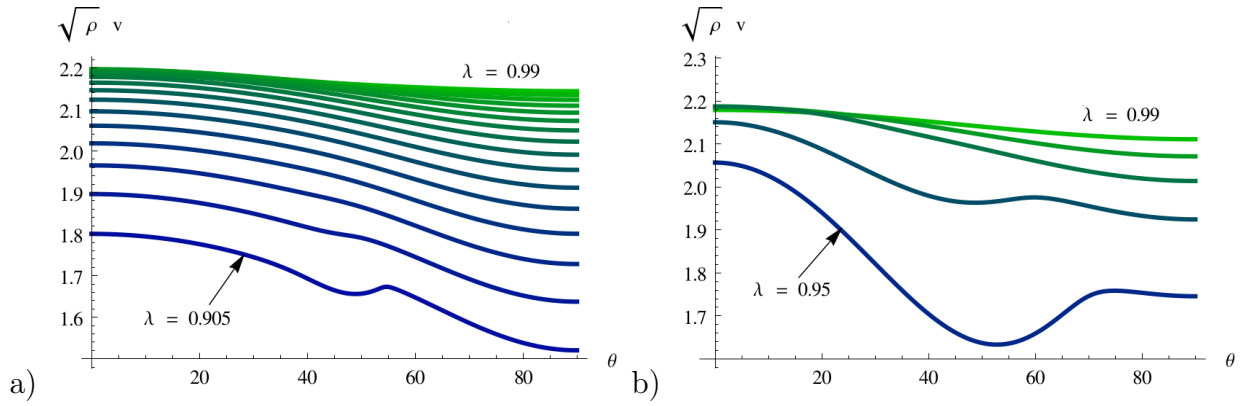


Figure 3.8: Speed profiles for surface waves (plotted as $v\sqrt{\rho}$) in steel subject to (a) uniaxial compressive stress, with pre-stretch λ decreasing from 0.990 to 0.905 (on the left) and (b) pure shear stress, with pre-stretch λ decreasing from 0.99 to 0.95 (on the right). As the color of the curves changes from green to blue, λ is decreased by regular increments of 0.0056 from one curve to the next.

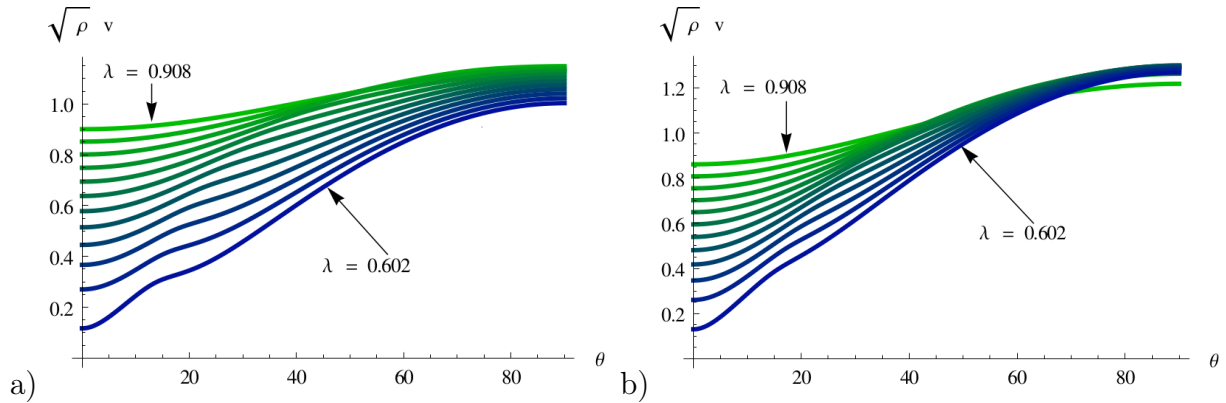


Figure 3.9: Speed profiles for surface waves (plotted as $v\sqrt{\rho}$) in polystyrene subject for (a) uniaxial compressive stress, with pre-stretch λ decreasing from 0.908 to 0.602 (on the left) and (b) pure shear stress, with pre-stretch λ decreasing from 0.908 to 0.602 (on the right). As the color of the curves changes from green to blue, λ is decreased by regular increments of 0.028 from one curve to the next.

a criterion which can thus be used to determine principal directions, at least in deformed nickel, steel, polystyrene and hydrogel. Unfortunately, this characteristic does not carry over to the case of surface waves, as the example of nickel subject to pure shear stress shows, where the fastest surface wave is oblique. The overall conclusion is that, for a given solid, a full analysis of wave speed variation with angle of propagation, such as that conducted in this paper, is required.

Acknowledgements

Partial funding from a Royal Society International Joint Project grant and from the Hardiman Scholarship programme at the National University of Ireland Galway

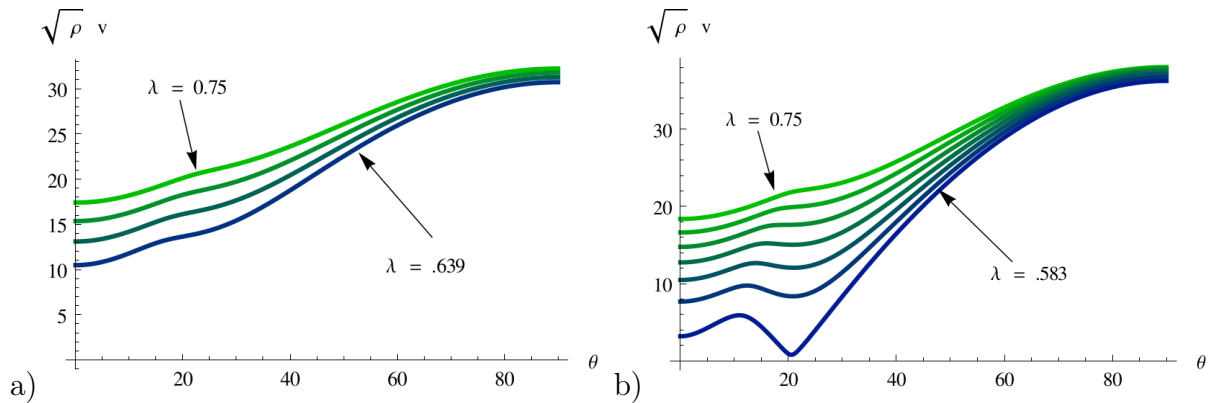


Figure 3.10: Speed profiles for surface waves (plotted as $v\sqrt{\rho}$) in hydrogel subject to (a) uniaxial compressive stress, with pre-stretch λ decreasing from 0.750 to 0.639 (on the left) and (b) pure shear stress, with pre-stretch λ decreasing from 0.750 to 0.583 (on the right). As the color of the curves changes from green to blue, λ is decreased by regular increments of 0.028 from one curve to the next.

are gratefully acknowledged. Helpful discussions with Alexander Shuvalov are also acknowledged.

References

- Alshits, V. and Maugin, G. (2005). “Dynamics of multilayers: elastic waves in an anisotropic graded or stratified plate”. In: *Wave Motion* 41, 357–394.
- Barnett, D. and Lothe, J. (1985). “Free surface (Rayleigh) waves in anisotropic elastic half-spaces: the surface impedance method”. In: *Proceedings of the Royal Society of London A: Mathematical, Physical and Engineering Sciences* 402, 135–152.
- Biryukov, S. (1985). “Impedance method in the theory of elastic surface waves”. In: *Sov. Phys. Acoust.*
- Brillouin, L. (1925). “Les tensions de radiation; leur interprétation en mécanique classique et en relativité”. In: *Journal de Physique et le Radium* 6, 337–353.
- Destrade, M., Murphy, J. G., and Saccomandi, G. (2012). “Simple shear is not so simple”. In: *International Journal of Non-Linear Mechanics* 47, 210–214.
- Destrade, M. and Ogden, R. W. (2012). “On stress-dependent elastic moduli and wave speeds”. In: *IMA Journal of Applied Mathematics*, hxs003.
- Destrade, M. et al. (2005). “Non-principal surface waves in deformed incompressible materials”. In: *International Journal of Engineering Science* 43, 1092–1106.
- Dowdikh, M. and Ogden, R. (1991). “On surface waves and deformations in a compressible elastic half-space”. In: *Stability and Applied Analysis of Continuous Media* 1, 27–45.
- Fu, Y. B. and Mielke, A. (2002). “A new identity for the surface-impedance matrix and its application to the determination of surface-wave speeds”. In: *Proceedings*

- of the Royal Society of London A: *Mathematical, Physical and Engineering Sciences* 458, 2523–2543.
- Gandhi, N., Michaels, J. E., and Lee, S. J. (2012). “Acoustoelastic Lamb wave propagation in biaxially stressed plates”. In: *The Journal of the Acoustical Society of America* 132, 1284–1293.
- Guyer, R. A. and Johnson, P. A. (2009). *Nonlinear mesoscopic elasticity*. Wiley.
- Hughes, D. S. and Kelly, J. (1953). “Second-order elastic deformation of solids”. In: *Physical review* 92, 1145.
- Kayestha, P., Wijeyewickrema, A. C., and Kishimoto, K. (2011). “Wave propagation along a non-principal direction in a compressible pre-stressed elastic layer”. In: *International Journal of Solids and Structures* 48, 2141–2153.
- Kim, K. Y. and Sachse, W. (2000). “Acoustoelasticity of elastic solids”. In: *Handbook of Elastic Properties of Solids, Liquids, and Gases, Four-Volume Set*. Ed. by M. Levy, H. Bass, and R. Stern. New York: Academic Press, 441–468.
- Landau, L. D. et al. (1986). *Course of Theoretical Physics: Theory of Elasticity*. Butterworth-Heinemann.
- Lurie, A. and Belyaev, A. (2005). *Theory of Elasticity. Foundations of Engineering Mechanics*. Berlin: Springer.
- Mielke, A. and Fu, Y. B. (2004). “Uniqueness of the surface-wave speed: A proof that is independent of the Stroh formalism”. In: *Mathematics and Mechanics of Solids* 9, 5–15.
- Mihai, L. A. and Goriely, A. (2011). “Positive or negative Poynting effect? The role of adscititious inequalities in hyperelastic materials”. In: *Proceedings of the Royal Society of London A: Mathematical, Physical and Engineering Sciences* 467, 3633–3646.
- Norris, A. N. (1983). “Propagation of plane waves in a pre-stressed elastic medium”. In: *The Journal of the Acoustical Society of America* 74, 1642–1643.
- Norris, A. N. and Shuvalov, A. (2010). “Wave impedance matrices for cylindrically anisotropic radially inhomogeneous elastic solids”. In: *Q. J. Mech. Appl. Math.* hbq010.
- Ogden, R. W. (1997). *Non-linear elastic deformations*. Dover.
- Pao, Y. (1984). “Acoustoelasticity and ultrasonic measurements of residual stresses”. In: *Physical Acoustics*, 61–143.
- Rogerson, G. and Sandiford, K. (1999). “Harmonic wave propagation along a non-principal direction in a pre-stressed elastic plate”. In: *International Journal of Engineering Science* 37, 1663–1691.
- Shuvalov, A., Poncelet, O., and Deschamps, M. (2004). “General formalism for plane guided waves in transversely inhomogeneous anisotropic plates”. In: *Wave Motion* 40, 413–426.
- Tanuma, K., Man, C.-S., and Du, W. (2012). “Perturbation of phase velocity of Rayleigh waves in pre-stressed anisotropic media with orthorhombic principal part”. In: *Mathematics and Mechanics of Solids*, 1081286512438882.
- Wu, M. and Kirchner, H. (2010). “Nonlinear elasticity modeling of biogels”. In: *Journal of the Mechanics and Physics of Solids* 58, 300–310.

Chapter 4

Connecting the Material Parameters of Soft Fibre Reinforced Solids with the Formation of Surface Wrinkles.

Artur L. Gower*

Abstract

There is a need for more complete models of fibre reinforced solids that use both anisotropic invariants. However, these models offer major challenges. Two of these challenges are how to combine these anisotropic invariants, and how to reliably determine the model's parameters from experiments. We present an intuitive way to account for both anisotropic invariants through a measure of the fibre's extension and a measure of the fibre's compression. We suggest that a possible remedy to help characterise the material is to use experiments that cause wrinkles to appear on the surface of the material. We call these wrinkles surface-wrinkles. A soft solid, when compressed, will often develop surface wrinkles within its elastic regime. Much like when we pinch our skin. Here we use the theory of elasticity to effectively model these large deformations and predict the formation of small superimposed wrinkles. Hence we work through the conditions for small surface-wrinkles to appear, and apply these conditions to a simple model that uses both the measures of fibre extension and compression. It turns out that the angle between the fibres and the surface wrinkle's orientation can be used to distinguish whether the fibres resist only extension, compression, or a mixture of both. We also uncover a striking tendency of this angle between the fibres and the wrinkle orientation to alternate between only three or four fixed quanta. This trend increases as the fibres strength is increased.

*School of Mathematics, Statistics and Applied Mathematics,
National University of Ireland Galway, University Road, Galway, Ireland

4.1 Introduction

Many biological tissues are composed of a soft matrix reinforced by stiffer fibres approximately aligned in one direction at any given point. A most prevalent example is fibres made of collagen embedded in a soft matrix of elastin (Criscione et al. 1999; Donzelli et al. 1999). If we wish to explore phenomena on a larger scale than the distance between the fibres, then the investigation can be simplified by assuming that the material is homogeneous yet anisotropic with a preferred direction (Spencer 1984).

Much work has been done along this line, with models motivated by specific applications (Holzapfel and Ogden 2010), easy to fit to measurements (Lu and Zhang 2005), conserving strong-ellipticity (Ciarletta et al. 2011), and many more. In this work we introduce two anisotropic invariants related to the compression and extension of the fibres, and justify how a simple model based on these invariants addresses a few issues raised in the literature.

The majority of models for the sake of simplicity use only the anisotropic invariant $I_4 = \mathbf{M}^T \mathbf{C} \mathbf{M}$ (which is equivalent to $\mathbf{C} : \mathbf{M} \otimes \mathbf{M}$), and leave out the second anisotropic invariant $I_5 = \mathbf{M}^T \mathbf{C}^2 \mathbf{M}$, where $\mathbf{C} = \mathbf{F} \mathbf{F}^T$, \mathbf{F} is the deformation gradient and \mathbf{M} is a unit vector aligned with the fibres. It turns out that for these models two of the three shearing modes are identical and infinitesimal shear moduli are all identical, which is not supported by experiments (Murphy 2013). They are also unlikely to reproduce a certain range of tensile experiments (Destrade et al. 2013), and not allowing an independent contribution from both I_4 and I_5 creates new unrealistic universal relations (Pucci and Saccomandi 2014). We therefore advocate using both anisotropic invariants.

Most models have focused on how the fibres resist extension. However, Ciarletta et al. (2011) notes that there is evidence that the presence of fibres alters the mechanical response when under compression, both at the macroscopic (Van Loocke et al. 2006) and the microscopic levels (Brangwynne et al. 2006). To systematically incorporate the fibres' resistance to compression Ciarletta et al. (2011) introduced the structural invariant $\mathbf{M}^T (\mathbf{C} + \mathbf{C}^{-1}) \mathbf{M}$. However, this structural invariant does not separate the contributions from both anisotropic invariants. One advantage is that building a strain-energy density from $\mathbf{M}^T (\mathbf{C} + \mathbf{C}^{-1}) \mathbf{M}$ guarantees the condition of *strong-ellipticity* (SE) in planar deformations. However, a loss of SE can signal the occurrence of several physical phenomena (Merodio and Ogden 2003).

To avoid the above limitations, we propose that both anisotropic invariants be included through an invariant that measures the fibres' extension $I_4^S = I_4 = \mathbf{M}^T \mathbf{C} \mathbf{M}$ and another that measures the fibres compression $I_4^C = \mathbf{M}^T \mathbf{C}^{-1} \mathbf{M}$. A simple model with these measures has the following anisotropic strain-energy density part

$$W_A = \frac{A_S}{4} (I_4^S - 1)^2 + \frac{A_C}{4} (I_4^C - 1)^2, \quad (4.1)$$

where $A_S > 0$ and $A_C > 0$ are constants. This way both invariants I_4 and I_5 are included independently, which is demonstrated in Section 4.2.1. The larger the value of A_S and A_C , the greater the fibres will resist being stretched and

compressed, respectively. This model is a simple prototype, but given the need, more complex models can be developed, such as ones that include the strong stiffening effect observed in collagen (Holzapfel et al. 2000).

One major challenge for anisotropic models is to be able to reliably determine the model's parameters from experiments. Even the protocol for simple tensile testing has not been completely established, as these tests induce shear forces and bending moments (Destrade et al. 2013). Having both anisotropic invariants further complicates matters; for example it is not possible to fully characterise such a material even with a full range of planar biaxial tests (Holzapfel and Ogden 2009).

A possible remedy is to use surface-wrinkling experiments to help characterise the material. We have noticed that varying the fibres' resistance to being stretched and compressed creates very distinct wrinkling patterns (Section 4.3). In essence, wrinkles appear to minimize the strain-energy. When the fibres are stiffer than the surrounding soft matrix, the wrinkles predominantly act to lengthen the fibres, if they resist compression, or shorten the fibres, if they resist extension. This is essentially why varying the contribution from I_4^C and I_4^S to W_A distinctly alters the wrinkling pattern. For a pictorial view of a surface-wrinkle see Figure 4.2 and Mora et al. (2011).

Although the theory behind calculating surface wrinkles is now well established, there is still a scarcity of work investigating this wrinkling of soft anisotropic solids. One notable work (Destrade et al. 2008) investigates the wrinkling of the classic reinforcement model $A_C = 0$ for simple shear. One major difficulty encountered in that search is how to avoid numerical instabilities. Following along the line of Destrade et al. (2008) we use a method based on the surface impedance matrix (Fu and Mielke 2002; Fu 2005). In Section 4.3.2 we present this robust numerical method and demonstrate how it can be reliably used for any choice of anisotropy with one family of fibres. With this method in hand we uncover a striking tendency: the angle between the fibres and the wrinkle orientation alternates between three or four quanta, shown in Figure 4.6.

Other than determining material parameters, understanding the formation of wrinkling has many technological applications. For instance, wrinkles are induced to develop functional coatings, such as diffractors or substrates for cellular growth (Li et al. 2012). On the other hand, when a material wrinkles it may have reached the limit of its performance (Genzer and Groenewold 2006). Most applications make use of predictions from linear elasticity, but in the presence of large strain or stress, the nonlinear theory may lead to significantly different outcomes (Gower et al. 2013). In this context, the process of wrinkling has contributed to understanding the morphogenesis and the origin of shapes in biological tissues (Ben Amar and Goriely 2005; Balbi and Ciarletta 2013).

Wrinkling as a measurement tool has been successfully developed by researchers at the US National Institute of Standards and Technology (Stafford et al. 2004). This new experimental technique measures the strain needed for thin films to wrinkle, and with this measure determines their elastic modulus. Given the right theoretical and numerical tools, the wrinkling of soft solids can also be used to

assist in characterising the fibre reinforcement, their orientation and the underlying isotropic matrix. For instance, there is a great interest for such a method to determine the fibres' orientation in human skin (Ciarletta et al. 2013).

The outline is as follows. We explain our choice of fibre reinforcement in Section 4.2.1, and then develop the relevant incremental equations and the basis for using the Riccati equation to calculate surface-wrinkles in Section 4.2.2. To exemplify the numerical method we present the shear-box deformation in Section 4.3.1. Using the shear-box as an illustration, the Riccati method for calculating surface-wrinkles is given in Section 4.3.2. With this method we predict the formation of wrinkles for the shear-box and investigate the results in Section 4.3.3. Based on the results we suggest asymptotic methods in Section 4.3.4. We summarise the important features of this paper in Section 4.4, and give a recap of the phenomena uncovered in the wrinkling pattern, together with directions for possible future work.

4.2 The Model

4.2.1 Theoretical Setup

Here we look at the material's response to a large deformation and justify our model, which consists of a single-family of fibres in a soft matrix. This model is essentially a transversely anisotropic medium. In Section 4.2.2 we move onto the formation of wrinkles. For more background on the subject of anisotropic nonlinear elasticity see Spencer (1984).

The behaviour of the material will be determined by our choice of the strain-energy density W . We assume that $W = W_I + W_A$, that is, the sum of an isotropic part and an anisotropic part. For W_I we use a compressible Mooney-Rivlin material,

$$W_I = C_1(I_3^{-1/3}I_1 - 3) + C_2(I_3^{-2/3}I_2 - 3) + \frac{\kappa}{2}(I_3 - 1)^2, \quad (4.2)$$

where $C_1 > 0$, $C_2 > 0$, $\kappa > 0$ are constants,

$$I_1 = \text{tr } \mathbf{C}, \quad I_2 = \frac{1}{2} [(\text{tr } \mathbf{C})^2 - \text{tr } (\mathbf{C}^2)], \quad I_3 = \det \mathbf{C} = J^2, \quad (4.3)$$

where $J = \det \mathbf{F}$ and $\mathbf{C} = \mathbf{F}^T \mathbf{F}$ is the right Cauchy-Green strain tensor. For the anisotropic contribution we consider a single family of fibres with their orientation in the reference configuration along the unit vector \mathbf{M} , which may vary within the material. We want a simple way to incorporate the fibres' resistance to both compression and extension, and we choose,

$$W_A = \frac{\mathbf{A}_S}{4}(I_4^S - 1)^2 + \frac{\mathbf{A}_C}{4}(I_4^C - 1)^2, \quad (4.4)$$

where

$$I_4^S = \mathbf{M}^T \mathbf{C} \mathbf{M}, \quad I_4^C = \mathbf{M}^T \mathbf{C}^{-1} \mathbf{M}, \quad (4.5)$$

and $A_S > 0$ and $A_C > 0$ are constants. The square in both the terms of W_A guarantees that W_A is positive, and that the material is stress-free when undeformed, i.e. when $\mathbf{C} = \mathbf{I}$, the Cauchy stress is zero. The invariant I_4^S measures how stretched the fibres are, while I_4^C measures their compression. To justify this statement we decompose \mathbf{F} along the principal directions to obtain

$$\mathbf{F} = \lambda_i \mathbf{v}^i \otimes \mathbf{V}^i, \quad (4.6)$$

where \mathbf{v}^i and \mathbf{V}^i are unit vectors. When deformed, the fibres' orientation and stretch are given by $\mathbf{m}^S = \mathbf{F}\mathbf{M}$ and $\|\mathbf{m}^S\|$ respectively. This can be written as $\mathbf{m}^S = \lambda_i (\mathbf{V}^i \cdot \mathbf{M}) \mathbf{v}^i$ and $\|\mathbf{m}^S\|^2 = \lambda_i^2 (\mathbf{V}^i \cdot \mathbf{M})^2 = \mathbf{M}^T \mathbf{C} \mathbf{M}$. Here the stretch ratio of the fibre is accounted for by the principal stretches λ_i 's. So a term such as $\lambda_i^{-2} (\mathbf{V}^i \cdot \mathbf{M})^2 = \mathbf{M}^T \mathbf{C}^{-1} \mathbf{M}$ would be appropriate to measure the compression ratio of the fibres. This measure is related to the vector $\mathbf{m}^C = \mathbf{F}^{-T} \mathbf{M} = \lambda_i^{-1} (\mathbf{V}^i \cdot \mathbf{M}) \mathbf{v}^i$ because $\|\mathbf{m}^C\|^2 = \mathbf{M}^T \mathbf{C}^{-1} \mathbf{M}$. Note that using $\mathbf{M}^T \mathbf{C}^{-1} \mathbf{M}$ rather than $1/(\mathbf{M}^T \mathbf{C} \mathbf{M})$ leads to simpler algebraic expressions.

For any model of anisotropy to reproduce a range of experiments, both the classical invariants, commonly named $I_4 = I_4^S$ and $I_5 = \mathbf{M}^T \mathbf{C}^2 \mathbf{M}$, must have an independent contribution to the strain-energy density W (Murphy 2013). This condition is respected for any strain energy that has an independent contribution from I_4^S and I_5^S , such as W_A . We show this statement by applying the Cayley–Hamilton theorem to \mathbf{C} to get

$$\mathbf{C}^3 - \mathbf{C}^2 I_1 + \mathbf{C} I_2 - I_3 = 0 \implies \mathbf{C}^2 - \mathbf{C} I_1 + I_2 - \mathbf{C}^{-1} I_3 = 0, \quad (4.7)$$

multiplying by \mathbf{M}^T on the left side and \mathbf{M} on the right side, and then rearranging, we reach

$$I_5 = I_5^S I_3 + I_4^S I_1 - I_2. \quad (4.8)$$

As $I_3 \neq 0$, both I_5 and I_4 are independently accounted for in W_A . The papers by Ciarletta et al. (2011, 2013) use the structural invariant $I_\alpha = I_4^S + I_4^C - 1$, and fixing $A_C = 0$ is known as the standard fibre reinforcement model (Destrade et al. 2013).

Now consider that the material is deformed by taking a material point initially at \mathbf{X} in the reference configuration to position $\mathbf{x} = \mathbf{x}(\mathbf{X})$ in the current configuration. Let (X_1, X_2, X_3) and (x_1, x_2, x_3) be fixed rectangular Cartesian coordinates of \mathbf{X} and \mathbf{x} , respectively. The Cauchy stress tensor $\boldsymbol{\sigma}$ is then given by the connection (Ogden 1997; Marsden and Hughes 1994)

$$\sigma_{ij} = J^{-1} \frac{\partial W}{\partial F_{ia}} F_{ja}, \quad (4.9)$$

where $F_{ij} = \partial x_i / \partial X_j$. Through our choice $W = W_I + W_A$ we can separate the stress into

$$\sigma_{ij} = \sigma_{ij}^I + \sigma_{ij}^A, \quad (4.10)$$

where

$$\sigma_{ij}^I = J^{-1} \frac{\partial W_I}{\partial F_{ia}} F_{ja} \quad \text{and} \quad \sigma_{ij}^A = J^{-1} \frac{\partial W_A}{\partial F_{ia}} F_{ja}. \quad (4.11)$$

Introducing $\mathbf{m}^C = \mathbf{F}^{-1}\mathbf{M}$ and $\mathbf{m}^S = \mathbf{F}\mathbf{M}$ we find that

$$\sigma_{ij}^A = J^{-1} (\mathbf{A}_S(I_4^S - 1)m_i^S m_j^S - \mathbf{A}_C(I_4^C - 1)m_i^C m_j^C), \quad (4.12)$$

and

$$\sigma_{ij}^I = -p\delta_{ij} + 2(C_2 I_1 + C_1) B_{ij} - 2C_2 B_{i\beta_1} B_{j\beta_1}, \quad (4.13)$$

for an incompressible solid, where p is a Lagrange multiplier due to the constraint $\det F = 1$ at all times. For a compressible solid we find

$$\begin{aligned} \sigma_{ij}^I = & - \left(\frac{2}{3} C_1 I_1 I_3^{-1/3} + \frac{4}{3} C_2 I_2 I_3^{-2/3} - 2\kappa(I_3 - 1)I_3 \right) \delta_{ij} \\ & + 2 \left(C_2 I_1 I_3^{-2/3} + C_1 I_3^{-1/3} \right) B_{ij} - 2C_2 I_3^{-2/3} B_{i\beta_1} B_{j\beta_1}. \end{aligned}$$

The compressible version of $\boldsymbol{\sigma}^I$ is more involved but also more general. The method we present in Section 4.2.2 is for compressible solids, though because we focus on almost incompressible solids, the simpler incompressible equations can be useful.

To see how this model of anisotropy influences the stress response, we take a uniaxial isochoric deformation parallel to the fibres $F_{ij} = \lambda M_i M_j + \lambda^{-1} M_i^\perp M_j^\perp$, with the unit vector \mathbf{M}^\perp perpendicular to \mathbf{M} , leading to

$$\sigma_{ij}^A = [\lambda^2 \mathbf{A}_S(\lambda^2 - 1) - \lambda^{-2} \mathbf{A}_C(\lambda^{-2} - 1)] M_i M_j.$$

To illustrate we plot several curves of $\sigma_m = \sigma_{ij}^A M_j M_i$ against λ , see Figure 4.1.

4.2.2 Incremental Equations

To reach the conditions for small amplitude surface-wrinkles to appear on top of a large elastic deformation, we need to first work through the incremental equations of stress and equilibrium. Then we must apply these equations to a surface-wrinkle. We do this in a simple setting where the material occupies the half-space $x_2 \geq 0$, and we take the boundary $x_2 = 0$ to be free of traction. A small-amplitude wrinkle in this material is described by the displacement field $\mathbf{u} = \mathbf{u}(\mathbf{x})$, satisfying in the cartesian coordinate system (x_1, x_2, x_3) the incremental equations of equilibrium (Ogden 1997),

$$s_{pj,p} = \mathcal{A}_{pjql} u_{\ell,pq} = 0 \quad \text{with} \quad \mathcal{A}_{pjql} = \frac{1}{J} F_{pa} F_{qb} \frac{\partial^2 W}{\partial F_{ja} \partial F_{lb}} = \mathcal{A}_{pjql}^I + \mathcal{A}_{pjql}^A, \quad (4.14)$$

where $s_{pi} = \mathcal{A}_{pijq} u_{j,q}$ are the components of the incremental nominal stress tensor, \mathcal{A}_{pjql}^I and \mathcal{A}_{pjql}^A are, respectively, the contribution to \mathcal{A}_{pjql} from W_I and W_A . We

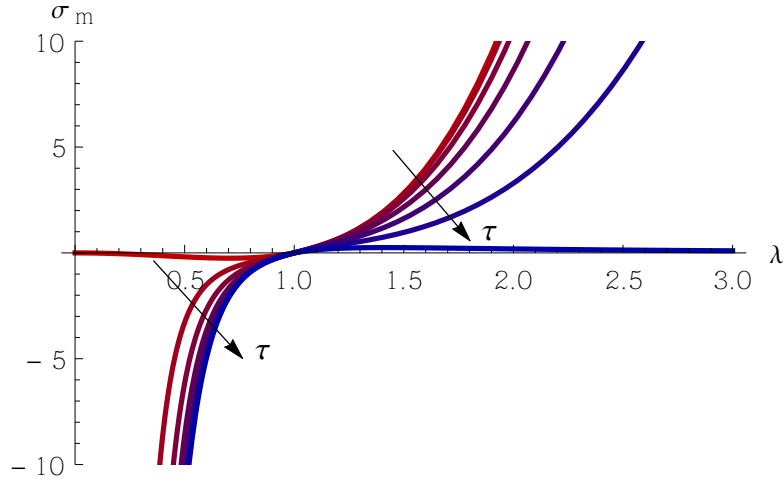


Figure 4.1: The ratio of uniaxial deformation λ against the stress σ_m , both taken along the fibre orientation \mathbf{M} . Each curve corresponds to a different value for τ where $\mathbf{A}_S = \cos \tau$ and $\mathbf{A}_C = \sin \tau$. As the curves shade from red to blue (indicated by the arrows), τ increases from 0 to $\pi/2$ by increments of $\pi/12$, and the material offers less resistance to extension and more resistance to compression.

assume that in the region of dead-load stability, see Ogden (1997), \mathcal{A} satisfies the *strong-convexity* condition (S-C)

$$\mathcal{A}_{ijkl}\xi_{ij}\xi_{kl} > 0 \quad \text{for all non-zero matrices } \boldsymbol{\xi}. \quad (4.15)$$

The *strong-ellipticity* condition reads

$$\mathcal{A}_{paqb}v_p v_q w_a w_b > 0 \quad \text{for all non-zero vectors } \mathbf{v} \text{ and } \mathbf{w}, \quad (4.16)$$

and is implied by strong-convexity. For an interpretation of strong-ellipticity see Walton and Wilber (2003); Merodio and Ogden (2003). Using W_A from equation (4.4) and (4.14)₂ we find that

$$\begin{aligned} \mathcal{A}_{ijkl}^A = \mathbf{A}_C & \left[(I_4^C - 1) (\delta_{jk} m_i^C m_\ell^C + \delta_{ik} m_j^C m_\ell^C + \delta_{i\ell} m_j^C m_k^C) + 2m_i^C m_j^C m_k^C m_\ell^C \right] \\ & + \mathbf{A}_S \left[(I_4^S - 1) \delta_{j\ell} m_i^S m_k^S + 2m_i^S m_j^S m_k^S m_\ell^S \right]. \end{aligned} \quad (4.17)$$

A wrinkle along the surface $x_2 = 0$ with wrinkle-front normal to the \mathbf{n} direction is of the form

$$\mathbf{u}(x_1, x_2, x_3) = \mathbf{U}(x_2) e^{ik\mathbf{x}\cdot\mathbf{n}}, \quad (4.18)$$

where the amplitude \mathbf{U} is a vector function of x_2 alone, k is the wavenumber and $\mathbf{n} = (\cos \theta, 0, \sin \theta)$. We can think of \mathbf{U} as the result of a Fourier transform in x_1 and x_3 , implying that solving \mathbf{U} for every θ will form a complete basis for first-order bifurcation. For \mathbf{u} to satisfy the equations of motion (4.14)₁ for every x_1 and x_3 we must have

$$\mathbf{T}\mathbf{U}''(x_2) + ik(\mathbf{R} + \mathbf{R}^T)\mathbf{U}'(x_2) - k^2\mathbf{Q}\mathbf{U}(x_2) = \mathbf{0}, \quad (4.19)$$

where the matrices $\mathbf{R}, \mathbf{Q}, \mathbf{T}$ are given by

$$\mathbf{T} = \mathbf{Q}^{\{2\}}, \quad \mathbf{R} = \mathbf{R}^{\{3\}} \cos \theta + \mathbf{R}^{\{1\}} \sin \theta, \quad (4.20)$$

$$\mathbf{Q} = \mathbf{Q}^{\{1\}} \cos^2 \theta + \mathbf{Q}^{\{3\}} \sin^2 \theta + (\mathbf{R}^{\{2\}} + \mathbf{R}^{\{2\}T}) \cos \theta \sin \theta, \quad (4.21)$$

which in turn are defined in terms of their components by

$$\begin{aligned} Q_{j\ell}^{\{1\}} &= \mathcal{A}_{1j1\ell}, & Q_{j\ell}^{\{2\}} &= \mathcal{A}_{2j2\ell}, & Q_{j\ell}^{\{3\}} &= \mathcal{A}_{3j3\ell}, \\ R_{j\ell}^{\{1\}} &= \mathcal{A}_{2j3\ell}, & R_{j\ell}^{\{2\}} &= \mathcal{A}_{3j1\ell}, & R_{j\ell}^{\{3\}} &= \mathcal{A}_{2j1\ell}, \\ Q_{j\ell} &= \mathcal{A}_{pjql} n_p n_q, & R_{j\ell} &= \mathcal{A}_{2jq\ell} n_q, \end{aligned} \quad (4.22)$$

where $Q_{ij}^{\{n\}} = Q_{ji}^{\{n\}}$ for $n = 1, 2$ and 3 . The matrices $\mathbf{Q}^{\{1\}}, \mathbf{Q}^{\{2\}}, \mathbf{Q}^{\{3\}}$ and \mathbf{Q} are positive definite due to strong-ellipticity (4.16).

A surface-wrinkle is simply a wrinkle that decays as x_2 increases, that is

$$\lim_{x_2 \rightarrow \infty} \mathbf{U}(x_2) = 0. \quad (4.23)$$

To satisfy this condition it is well established, see Ting (1996), that the general solution to the ODE (4.19) is of the form

$$\mathbf{U}(x_2) = e^{ik\mathbf{E}x_2} \mathbf{U}_0 \quad (4.24)$$

where \mathbf{U}_0 is a constant vector and \mathbf{E} is a constant 3×3 matrix (not to be confused with the Green strain) whose eigenvalues have a positive imaginary part, i.e. $\text{Im Spec } \mathbf{E} > 0$. Such an \mathbf{E} always exists if strong-ellipticity holds.

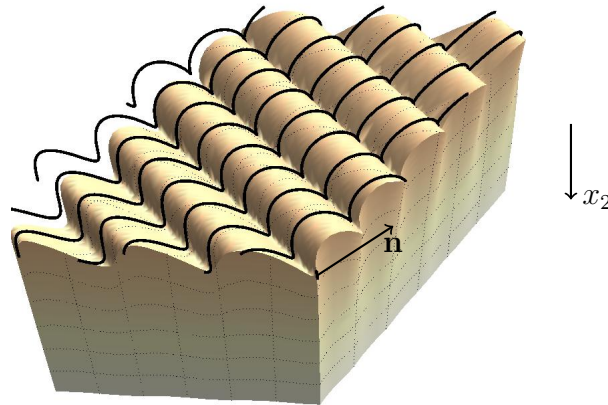


Figure 4.2: An illustration of a surface-wrinkle on a fibre reinforced material, with \mathbf{n} being normal to the wrinkle-front. The curvy black lines indicate the fibre angle. Note that the surface-wrinkle's amplitude decays as x_2 increases.

Figure 4.2 illustrates a surface wrinkle and how its amplitude decays when moving away from the surface (as x_2 increases).

The resulting incremental nominal traction $s_{pi} = \mathcal{A}_{piqj}u_{j,q}$ due to the wrinkle \mathbf{u} is

$$s_{2i} = ik(\mathbf{R}_{ij} + \mathbf{T}_{ia}\mathbf{E}_{aj})u_j. \quad (4.25)$$

For the surface $x_2 = 0$ to have zero traction, then $s_{2i} = 0$ for $i = 1, 2$ and 3 , which in turn implies that $\det(\mathbf{R} + \mathbf{TE}) = 0$. Now rather than solving for \mathbf{E} with $\text{Im Spec } \mathbf{E} > 0$, and that satisfies the above condition, a successful method is to solve directly for the *impedance matrix*

$$\mathbf{Z} = -i(\mathbf{R} + \mathbf{TE}), \quad \text{where} \quad s_{2i} = -k\mathbf{Z}_{ij}u_j. \quad (4.26)$$

The impedance matrix relates the incremental displacement to the incremental normal traction, as shown above, which leads to many useful properties (Fu and Mielke 2002; Gower et al. 2013; Norris and Shuvalov 2010). The decay condition $\text{Im Spec } \mathbf{E} > 0$ is equivalent to $\mathbf{Z} = \mathbf{Z}^\dagger$ together with $\mathbf{Z} > 0$, where the superscript \dagger denotes the Hermitian, both these properties can be shown through balance of virtual momentum (Gower et al. 2013). A traction free surface is guaranteed if $\det \mathbf{Z} = 0$. To solve for \mathbf{Z} we substitute $\mathbf{E} = i\mathbf{T}^{-1}(\mathbf{Z} + i\mathbf{R})$ and the form (4.24) into the ODE (4.19), to reach the algebraic Riccati equation

$$(\mathbf{R}^\mathbf{T} + i\mathbf{Z})\mathbf{T}^{-1}(\mathbf{R} - i\mathbf{Z}) - \mathbf{Q} = 0, \quad (4.27)$$

which has a unique solution for a positive definite \mathbf{Z} (i.e. $\mathbf{Z} > 0$). Because \mathbf{Z} is Hermitian we can rewrite the Riccati equation (4.27) as

$$(\mathbf{R}^\mathbf{T} + i\mathbf{Z})\mathbf{T}^{-1/2} \left[(\mathbf{R}^\mathbf{T} + i\mathbf{Z})\mathbf{T}^{-1/2} \right]^\dagger = \mathbf{Q}, \quad (4.28)$$

There are efficient numerical methods to solve the Riccati equation based on Schur decomposition (Laub 1979), Newton's method (Benner and Byers 1998) and more recently the matrix sign function (Norris et al. 2013).

In conclusion, a surface-wrinkle with zero surface traction corresponds to

$$\mathbf{Z} \geq 0 \text{ (positive semi-definite), } \mathbf{Z} = \mathbf{Z}^\dagger \text{ and } \det \mathbf{Z} = 0. \quad (4.29)$$

A similar use of the Riccati equation to find a zero-traction solution was originally developed for surface-waves (Mielke and Fu 2003). In Section 4.3.2 we describe how best to use the Riccati equation to locate a traction free surface-wrinkle.

4.3 Shear-Box Wrinkling

4.3.1 The Shear-box

To obtain a large homogeneous static deformation, we use the *shear-box deformation* (Stolz 2010), see Figure 4.3. Other experimental tests such as the finite bending test (Roccabianca et al. 2010) and simple tension experiments (Destrade et al. 2013) can become more involved when the experimental setup does not reflect the symmetries of the material. The shear-box deformation brings a point

with material coordinates (X_1, X_2, X_3) to the spatial position with coordinates (x_1, x_2, x_3) given by

$$x_1 = X_1 + X_3 \sin \phi, \quad x_2 = \lambda_2 X_2, \quad x_3 = X_3 \cos \phi, \quad (4.30)$$

where ϕ is the *tilting angle*: at $\phi = 0$, the box is rectangular; at $\phi = 90^\circ$, it is flattened. To achieve this deformation we imagine that the inner walls of the shear-box are lubricated so that the soft material placed within may slide. This way, when the box is tilted, the material can expand its height in the x_2 coordinate uniformly. To achieve a homogeneous deformation we also assume that the fibres are parallel to the free-surface $x_2 = 0$, a common occurrence in biological tissues. So we may write $\mathbf{M} = (\cos A, 0, \sin A)$. This in turn leads to the stress on the surface $x_2 = 0$, σ_{i2} , all being zero except for the normal component σ_{22} . So we

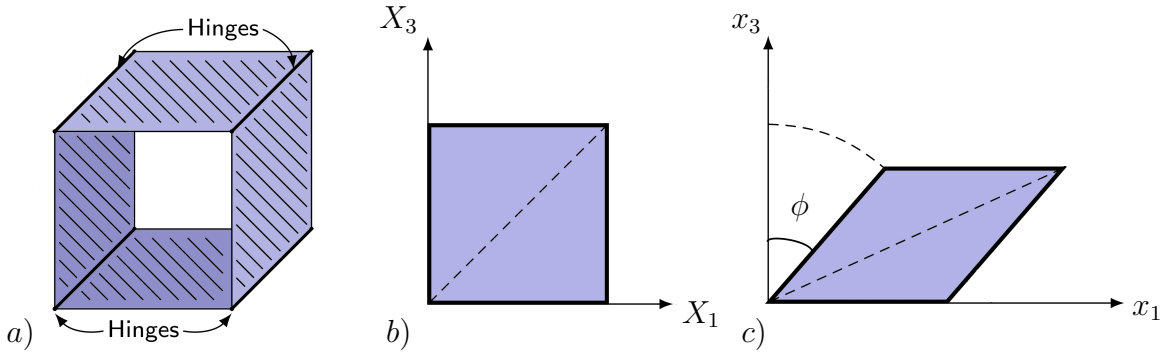


Figure 4.3: A schematic of the shear-box deformation.

determine the principal stretch λ_2 by solving $\sigma_{22} = 0$ in terms of ϕ , which leads to

$$C_1 (1 - \lambda_2^2) + C_2 (\lambda_2 \cos \phi)^{-2/3} (\cos^2 \phi - \lambda_2^2) + \frac{3}{2} \kappa (\lambda_2 \cos \phi)^{8/3} (1 - \lambda_2^2 \cos^2 \phi) = 0, \quad (4.31)$$

which must be solved numerically. For an incompressible material $\lambda_2 = (\cos \phi)^{-1}$, and for κ a hundred times larger than $C_1 + C_2$ for a compressible material, we find that $\lambda_2 \approx (\cos \phi)^{-1}$ with a maximum error of 1% for $\phi < 60^\circ$, which is within the range of our numerical experiments.

The shear-box is a simple example for it needs only the tilting angle ϕ to control the deformation, and it is viable to execute experimentally. In contrast, a biaxial test has many parameters and can be difficult to achieve in-plane for fibre reinforced solids (Holzapfel and Ogden 2009). With the shear-box deformation we will illustrate our method for calculating surface wrinkles and our asymptotic results.

4.3.2 The Riccati Method

The essence of the method is to deform the material step-by-step and check, at each step, whether the material can now sustain a surface-wrinkle. To describe

surface wrinkles we use the incremental framework developed in Section 4.2.2, and let the magnitude of the finite deformation be parametrized by ϕ , with $\phi = 0$ corresponding to no deformation (such as the tilt angle ϕ for the shear-box deformation).

To run the numerical method, the material constants C_1 , C_2 , κ , \mathbf{A}_S and \mathbf{A}_C in equations (4.2) and (4.4) must first be fixed. At this point the incremental moduli \mathcal{A}_{ijkl} , given in equations (4.14)₂, are a function of the magnitude of the deformation ϕ , the angle of the wrinkle-front θ , used in equation (4.18), and the angle of the fibres A . Note that $\mathbf{M} = (\cos A, 0, \sin A)$. So the matrices $\mathbf{T} = \mathbf{T}(\phi, \theta, A)$, $\mathbf{R} = \mathbf{R}(\phi, \theta, A)$ and $\mathbf{Q} = \mathbf{Q}(\phi, \theta, A)$ made up from the components of \mathcal{A}_{ijkl} are also functions of ϕ , θ and A . These matrices determine a unique positive definite \mathbf{Z} through the Riccati equation (4.27), so that \mathbf{Z} is also a function of ϕ , θ , and A . For there to exist an initial positive definite \mathbf{Z} for $\phi = 0$, the strong-convexity condition (4.15) must hold.

Below we calculate the first surface-wrinkle to appear. To do so, for each fibre angle A , we increase the deformation until we reach a critical amount $\phi = \phi^*(A)$, at which point $\det \mathbf{Z} = 0$, meaning that there exists a zero traction surface-wrinkle with $\theta = \theta^*(A)$. The method is detailed below.

The Riccati method

For each fibre orientation $A \in [0, \pi]$, set $\phi = 0$ then

1. Calculate for every $\theta \in [0, \pi]$ the positive semi-definite Hermitian \mathbf{Z} .
 2. If $\det \mathbf{Z} > tol$ for every $\theta \in [0, \pi]$, then increment ϕ and go back to 1.
 3. Find θ such that $\det \mathbf{Z}$ is a minimum, and set $\theta^*(A) = \theta$ and $\phi^*(A) = \phi$.
-

At the end of the process we have a curve $(\phi^*(A), \theta^*(A))$ giving the deformation magnitude and angle of the wrinkle-front as a function of the fibre angle A .

Methods based on looking for positive semi-definite solutions for \mathbf{Z} can be difficult to use. This is mainly due to the $\det \mathbf{Z}$ being very sensitive to small variations in ϕ , θ and A . So, at Step 2. the error tolerance tol would have to be much larger than the mesh size of ϕ and θ . Otherwise, at Step 1., after an increment in ϕ , we may step past the zero-traction solution and simply find no positive semi-definite solution for some θ . It is also possible not to find a positive semi-definite \mathbf{Z} because there is no surface-wrinkle for A . To distinguish between the two cases, it would be necessary to decrease ϕ very thinly to investigate which situation occurred.

This problem can be circumvented by using a method based on implicitly solving for \mathbf{Z} , without taking into consideration \mathbf{Z} being positive semi-definite. These implicit solutions should begin at the positive definite \mathbf{Z} for $\phi = 0$, but then as ϕ is increased one should seek solutions to \mathbf{Z} implicitly by using the Riccati equation (4.27), without explicitly looking for positive definiteness. The uniqueness of a positive semi-definite \mathbf{Z} means that the implicit solutions will be well defined, and that when $\det \mathbf{Z} < 0$, with Hermitian \mathbf{Z} , we are sure that a zero-traction surface-wrinkle exists, and is close by.

We note, however, that numerically for the model in question, a surface-wrinkle exists for every fiber orientation, within the parameters we explored. To verify the correctness of the algorithm, we also reproduced the results found in Ciarletta et al. (2013) and Destrade et al. (2013).

4.3.3 Predictions

For our simulations, we will set the material parameters in (4.2) to be $C_1 = 1$, $\kappa = 200$ (to make the material virtually incompressible), and will study the effect of varying C_2 and varying the fibres resistance to stretch A_S and to compression A_C in (4.4). To control the fibre strength and resistance to stretch/compression separately we set $(A_S, A_C) = (S \cos \tau, S \sin \tau)$, where S is a constant.

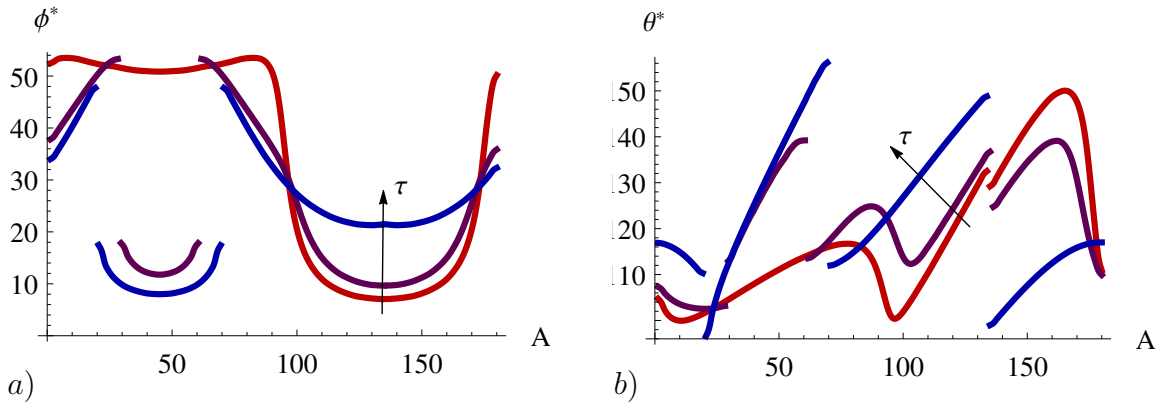


Figure 4.4: The graphs show the critical deformation ϕ^* and wrinkle-front angle θ^* for a surface-wrinkle to appear with fibre angle A degrees from the X_1 axes. The material parameters used were $S = 16$, $C_1 = 1$, $C_2 = 0$, $C_3 = 200$ and $\tau = 0^\circ$, 45° and 90° correspond to the red, purple and blue curves, respectively.

For the standard fibre reinforcement model, $A_C = 0$ and $C_2 = 0$, the ratio of the fibre strength has been estimated to be $S/C_1 = 20, 40, 80$ for several biological tissues (Destrade et al. 2008). So we will investigate the stability of fibre strength around the same order and take the values $S = 16, 32$, and 64 . For simplicity we begin by setting $C_2 = 0$, $C_1 = 1$. The wrinkling patterns for $S = 16$ are shown in Figure 4.4, with $\tau = 0^\circ$ (only resist extension), $\tau = 45^\circ$ (resist extension and compression equally) and $\tau = 90^\circ$ (only resist compression).

In Figure 4.5 we see how the stiffer the fibres (the larger S), the earlier the onset of surface-wrinkles. This same effect was noticed for simple shear (Destrade et al. 2008; Ciarletta et al. 2013). The dashed lines show when the fibres are along the direction of greatest stretch $A = 45^\circ$ and greatest compression $A = 90^\circ + 45^\circ$. We see that the most distinctive difference is that fibres that only resist extension wrinkle earlier when $A = 90^\circ + 45^\circ$, while in comparison the fibres that only resist compression wrinkle earlier when $A = 45^\circ$.

Figure 4.4b, showing A against θ^* , is harder to interpret. What relationship could one expect between the angle of the fibres before deformation A and the

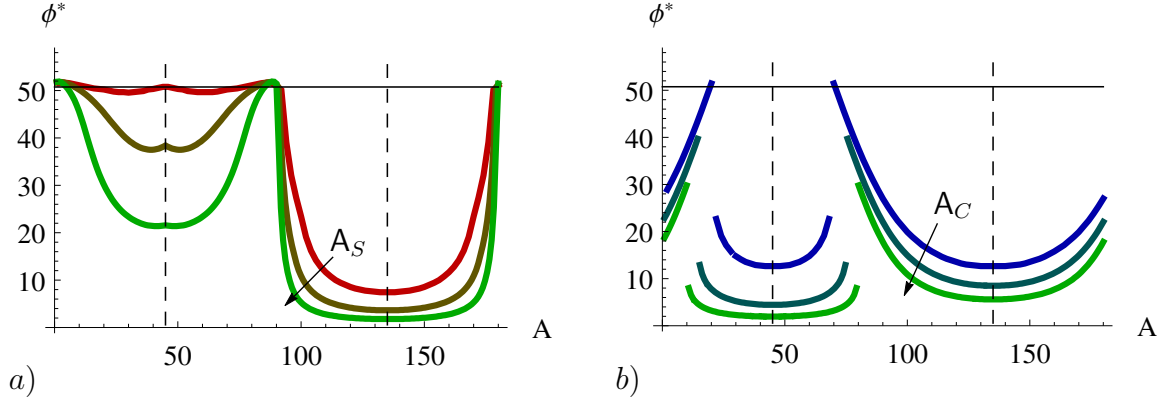


Figure 4.5: *a)* and *b)* are graphs of the onset of surface-wrinkles for fibres that only resist extension ($\tau = 0$) and compression ($\tau = \pi/2$), respectively. For both plots, as the curves shade towards green, \mathbf{S} takes the values 16, 32 and 64. The dashed lines show when the fibres are most stretched ($A = 45^\circ$) or most compressed ($A = 90^\circ + 45^\circ$). The solid black line $\phi^* = 50.75^\circ$ shows when a wrinkle would appear if there were no fibres.

angle of the wrinkle-front θ^* after deformation? We can make better sense of these results by using the current angle of the fibres α_S , and the compression counterpart α_C . To find these angles we need $\mathbf{F}_{ij} = \partial x_i / \partial X_j$, with x_i 's for the shear-box given by Equations (4.30). Then α_S and α_C are respectively the angles that $\mathbf{m}^S = \mathbf{F}\mathbf{M}$ and $\mathbf{m}^C = \mathbf{F}^{-T}\mathbf{M}$ make with x_1 axes,

$$\alpha_S = \tan^{-1} \left(\frac{\tan A \cos \phi}{\tan A \sin \phi + 1} \right) \quad \text{and} \quad \alpha_C = \tan^{-1} \left(\frac{\tan A - \sin \phi}{\cos \phi} \right). \quad (4.32)$$

Looking at \mathcal{A}_{ijkl}^A in equation (4.17) we can clearly see the importance of \mathbf{m}^S and \mathbf{m}^C . Their angles can be understood qualitatively through the maps $A \rightarrow \alpha_S(A, \phi)$ and $A \rightarrow \alpha_C(A, \phi)$, where we can imagine that ϕ is fixed. When the fibres are along the direction of greatest stretch in the reference configuration, $A = 45^\circ$, both these maps bring 45° to the angle of greatest stretch in the current configuration. The same applies to the direction of greatest compression, that is both α_S and α_C map $45^\circ + 90^\circ$ to the angle of least stretch in the current configuration. In general $A \rightarrow \alpha_S(A, \phi)$ takes points close to $A = 45^\circ$ and brings them even closer to $\alpha_S(45^\circ, \phi)$, while it takes points close to $A = 45^\circ + 90^\circ$ and repels them from $\alpha_S(45^\circ, \phi)$. The map $A \rightarrow \alpha_C(A, \phi)$ has the opposite effect.

Using these maps and the same parameter range in Figure 4.5 we produce two new plots: Figure 4.6*a* shows α_S against θ^* for fibres that resist extension and Figure 4.6*b* shows α_C against θ^* for fibres that resist compression. These graphs have multiple discontinuities and are even at times multivalued. From the theory there is no guarantee of a unique wrinkle-front angle θ^* and seemingly the stiffer the fibres, the more competing minima for θ^* appear. Figure 4.6 shows how the wrinkle-front angle θ^* changes as the fibres become stiffer (\mathbf{S} increases). These graphs show a clear trend. In Figure 4.6*a* the angle between α_S and θ^* alternates

between being close to the three quanta $\theta^* - \alpha_S = 90^\circ$, 33.3° and -33.3° . Similarly, in Figure 4.6b the angle between α_C and θ^* alternates between the three quanta $\theta^* - \alpha_C = 0^\circ$, 55° and -55° . In both cases the stiffer the fibres, the more closely $\theta^* - \alpha_S$ and $\theta^* - \alpha_C$ stay to their respective quanta. These same quanta, for both cases, seem not to change as C_2/C_1 is increased from 0% to 100%.

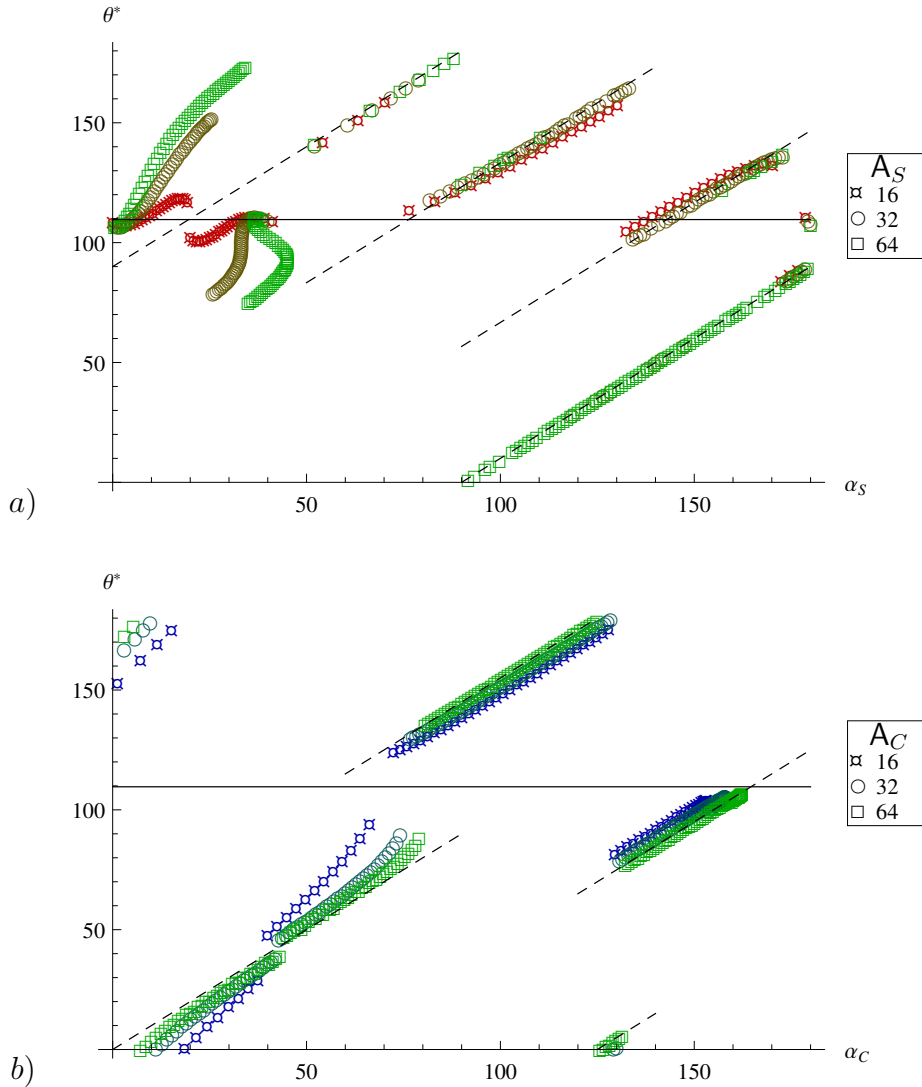


Figure 4.6: *a)* is a graph of the current fibre angle α_S against the wrinkle-front angle θ^* for a material with fibres that only resist extension. The dashed lines are either $\theta^* - \alpha_S = 90^\circ$, 33.3° or -33.3° . *b)* is a graph of the current compressive fibre angle α_C against the wrinkle-front angle θ^* for a material with fibres that only resist compression. The dashed lines are either $\theta^* - \alpha_C = 0^\circ$, 55° or -55° . In both cases the solid black line is given by $\theta^* = 109.6^\circ$ and is the wrinkle-front angle if there were no fibres.

The question that remains is how fibres with both $A_S \neq 0$ and $A_C \neq 0$ will behave. Figure 4.7 answers that question, where $A_S = A_C = 64 \cos 45^\circ$ and we

have varied the value of C_2 so as to illustrate that C_2 hardly affects the quanta. This time both the graphs (α_S, θ^*) and (α_C, θ^*) are similar, and both gravitate around the quanta $\theta^* - \alpha_C = 0^\circ, 55^\circ/2 + 33.3^\circ/2, 90^\circ$ and $-55^\circ/2 - 33.3^\circ/2$. For this reason Figure 4.7 only shows (α_C, θ^*) . Note that as C_2 decreases the fibres get comparatively stiffer than the isotropic matrix and again the curves get closer to the dashed lines. The values $55^\circ/2 + 33.3^\circ/2$ and $-55^\circ/2 - 33.3^\circ/2$ are half way between two of the quanta for $A_S = 0$ and two of the quanta for $A_C = 0$, which indicates that a simple rule relating A_S and A_C to the resulting quanta probably exists.

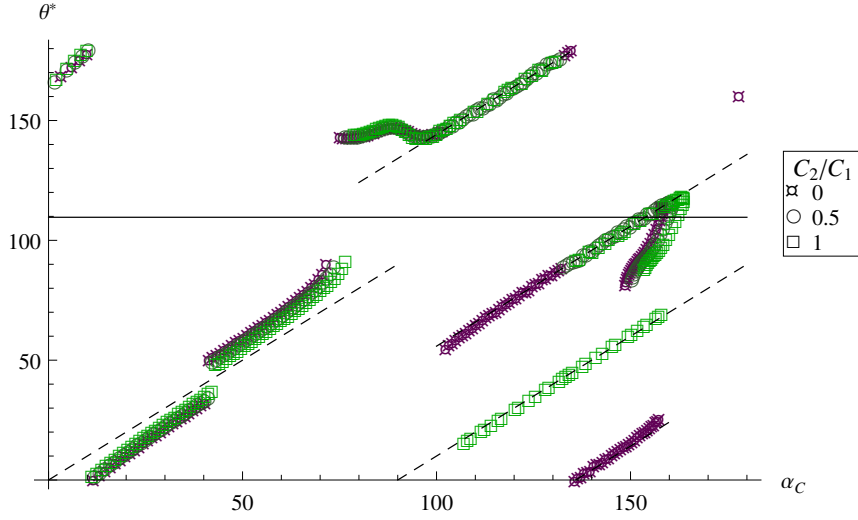


Figure 4.7: Shows a graph of (α_C, θ^*) for fibres with $A_S = A_C = 64 \cos 45^\circ$. The dashed lines are either $\theta^* - \alpha_C = 0^\circ, 90^\circ, 33.3^\circ/2 + 55^\circ/2$ or $-33.3^\circ/2 - 55^\circ/2$. The solid black line is given by $\theta^* = 109.6^\circ$ and is the wrinkle-front angle for $C_2 = 0$ and $C_1 = 1$ if there were no fibres.

4.3.4 Asymptotics

We have found that varying the fibres' resistance to compression and extension greatly changes the surface wrinkle-front angle. So it is possible to characterise the fibres through the formation of surface wrinkles, but the calculations to do so are quite demanding. If approximations could be developed to extract the key features in the wrinkling pattern, it might be enough to characterise the fibres without computing the complete wrinkling graphs.

Based on the numerical experiments of Section 4.3.3, an attractive choice is to approximate $\alpha_S - \theta$, or $\alpha_C - \theta$, defined by Equations (4.32), as being constant. A further simplification is to only investigate fibres that are approximately along the most and least stretched directions. For it is in these directions that a change in A_S and A_C most affects the critical deformation ϕ^* . Another reason to make this simplification is that for simple shear, α_S becomes asymptotic to the direction of greatest stretch (Ciarletta et al. 2013) when $\alpha_S - \theta \approx 90^\circ$.

Here we will only indicate how to formulate these approximations for a general homogeneous deformation. To simplify the calculations, we choose a coordinate system such that the deformation gradient \mathbf{F} is diagonalized, with $F_{ii} = \lambda_i$ for $i = 1, 2, 3$ and the λ_i 's are the principal stretches. Let $\lambda_3 > \lambda_1$ and let λ_2 correspond to a stretch which is orthogonal to the plane of the fibres, so that $\mathbf{M} = (\cos A, 0, \sin A)$. This way the current fibre angles α_S and α_C , measured from the x_1 axis, are

$$\alpha_S = \arctan\left(\frac{\lambda_3 \sin A}{\lambda_1 \cos A}\right) \quad \text{and} \quad \alpha_C = \arctan\left(\frac{\lambda_1 \sin A}{\lambda_3 \cos A}\right). \quad (4.33)$$

As an example, we will approximate α_C as being the angle of the direction of greatest stretch and approximate $\theta - \alpha_C = 0$, this would respectively translate to

$$\alpha_C = \pi/2 + \delta\alpha\pi \quad \text{and} \quad \alpha_C = \theta + \epsilon\pi, \quad (4.34)$$

for $\delta\alpha$ and ϵ small. Both these approximations hold true for a portion of every numerical experiment discussed in Section 4.3.3. From the first of these approximations we deduce that,

$$\cos A = \pm\delta\alpha\pi\frac{\lambda_1}{\lambda_3} + \mathcal{O}(\delta\alpha^3) \quad \text{and} \quad \sin A = 1 - \frac{\pi^2\delta\alpha^2}{2}\frac{\lambda_1^2}{\lambda_3^2} + \mathcal{O}(\delta\alpha^3). \quad (4.35)$$

From both approximations (4.34) we deduce that $\theta = \pi/2 + (\delta\alpha - \epsilon)\pi$, where we rename $\delta\alpha - \epsilon = \delta\theta$, resulting in

$$\cos\theta = -\delta\theta\pi + \mathcal{O}(\delta\theta^3) \quad \text{and} \quad \sin\theta = 1 - \frac{\delta\theta^2\pi^2}{2} + \mathcal{O}(\delta\theta^3). \quad (4.36)$$

Suppose that λ_1 , λ_2 and λ_3 are parametrized by some magnitude of deformation ϕ . These approximations can then be used in the incremental moduli \mathcal{A}_{ijkl} , from which we obtain the matrices $\mathbf{T} = \mathbf{T}(\delta\alpha, \delta\theta, \phi)$, $\mathbf{R} = \mathbf{R}(\delta\alpha, \delta\theta, \phi)$ and $\mathbf{Q} = \mathbf{Q}(\delta\alpha, \delta\theta, \phi)$ for the Riccati equation (4.27). Truncating the resulting Riccati equation for some order in $\delta\alpha$ and $\delta\theta$ may lead to analytic results, or at least greatly simplify the application of the Riccati method 4.3.2, as both $\delta\alpha$ and $\delta\theta$ need only have a small range.

4.4 Conclusion

There is a clear need for more complete models of fibre reinforced materials. Here we have pointed a way to include both anisotropic invariants in a simple physical way: through one invariant that measures fibre stretch I_4^S and another that measures fibre compression I_4^C . Giving a clear meaning to the anisotropic invariants makes it is easier to design specific models, and perhaps to fit parameters from experiments, as varying A_S and A_C dramatically changes the material's response. We also explained a method for using the Riccati equation to calculate surface wrinkles.

A striking phenomenon was revealed when studying the onset of surface-wrinkles: the difference between the current fibre orientation and the wrinkle orientation $\alpha_S - \theta^*$, and $\alpha_C - \theta^*$, tends to only occupy 3 or 4 possible discrete values, see Figure 4.7. This simple behaviour must have a simple underlying explanation. One possible avenue would be to develop asymptotic solutions, as suggested in Section 4.3.4. Explaining this quanta phenomenon could lead to a simple method for approximately calculating surface wrinkles for anisotropic materials, and therefore lead to an efficient way to characterise fibre reinforced soft solids by how they form surface-wrinkles.

Acknowledgements

The support of the Hardiman Foundation (NUI Galway) and of the Irish Research Council is gratefully acknowledged. I thank Konstantine Soldatos and Raymond Ogden for their support, and for organizing Euromech Colloquium 551: “Fibre-reinforced Materials: Theory and Applications”. I thank Michel Destrade for insightful discussions and support.

References

- Balbi, V. and Ciarletta, P. (2013). “Morpho-elasticity of intestinal villi”. In: *Journal of The Royal Society Interface* 10, 20130109.
- Ben Amar, M. and Goriely, A. (2005). “Growth and instability in elastic tissues”. In: *Journal of the Mechanics and Physics of Solids* 53, 2284–2319.
- Benner, P. and Byers, R. (1998). “An exact line search method for solving generalized continuous-time algebraic Riccati equations”. In: *Automatic Control, IEEE Transactions on* 43, 101–107.
- Brangwynne, C. P. et al. (2006). “Microtubules can bear enhanced compressive loads in living cells because of lateral reinforcement”. In: *The Journal of Cell Biology* 173, 733–741.
- Ciarletta, P., Destrade, M., and Gower, A. L. (2013). “Shear instability in skin tissue”. In: *The Quarterly Journal of Mechanics and Applied Mathematics* 2, 273–288.
- Ciarletta, P. et al. (2011). “Stiffening by fiber reinforcement in soft materials: a hyperelastic theory at large strains and its application”. In: *Journal of the mechanical behavior of biomedical materials* 4, 1359–1368.
- Criscione, J. C. et al. (1999). “Mechanical contribution of endocardium during finite extension and torsion experiments on papillary muscles”. In: *Annals of Biomedical Engineering* 27, 123–130.
- Destrade, M. et al. (2008). “Surface instability of sheared soft tissues.” In: *Journal of biomechanical engineering* 130, 061007.
- Destrade, M. et al. (2013). “At least three invariants are necessary to model the mechanical response of incompressible, transversely isotropic materials”. In: *Computational Mechanics* 52, 959–969.

- Donzelli, P. S. et al. (1999). “Contact analysis of biphasic transversely isotropic cartilage layers and correlations with tissue failure”. In: *Journal of Biomechanics* 32, 1037–1047.
- Fu, Y. (2005). “An integral representation of the surface-impedance tensor for incompressible elastic materials”. English. In: *Journal of Elasticity* 81, 75–90.
- Fu, Y. B. and Mielke, A. (2002). “A new identity for the surface-impedance matrix and its application to the determination of surface-wave speeds”. In: *Proceedings of the Royal Society of London A: Mathematical, Physical and Engineering Sciences* 458, 2523–2543.
- Genzer, J. and Groenewold, J. (2006). “Soft matter with hard skin: From skin wrinkles to templating and material characterization”. In: *Soft Matter* 2, 310–323.
- Gower, A. L., Destrade, M., and Ogden, R. (2013). “Counter-intuitive results in acousto-elasticity”. In: *Wave Motion* 50, 1218–1228.
- Holzappel, G. a. and Ogden, R. W. (2010). “Constitutive modelling of arteries”. In: *Proceedings of the Royal Society A: Mathematical, Physical and Engineering Sciences* 466, 1551–1597.
- Holzappel, G. A. and Ogden, R. W. (2009). “On planar biaxial tests for anisotropic nonlinearly elastic solids. A continuum mechanical framework”. In: *Mathematics and Mechanics of Solids* 14, 474–489.
- Holzappel, G., Gasser, T., and Ogden, R. (2000). “A New Constitutive Framework for Arterial Wall Mechanics and a Comparative Study of Material Models”. English. In: *Journal of Elasticity* 61, 1–48.
- Laub, A. J. (1979). “A Schur method for solving algebraic Riccati equations”. In: *Automatic Control, IEEE Transactions on* 24, 913–921.
- Li, B. et al. (2012). “Mechanics of morphological instabilities and surface wrinkling in soft materials: a review”. In: *Soft Matter* 8, 5728–5745.
- Lu, J. and Zhang, L. (2005). “Physically motivated invariant formulation for transversely isotropic hyperelasticity”. In: *International Journal of Solids and Structures* 42, 6015–6031.
- Marsden, J. E. and Hughes, T. J. R. (1994). *Mathematical Foundations of Elasticity*. Dover.
- Merodio, J. and Ogden, R. (2003). “Instabilities and loss of ellipticity in fiber-reinforced compressible non-linearly elastic solids under plane deformation”. In: *International Journal of Solids and Structures* 40, 4707–4727.
- Mielke, A. and Fu, Y. (2003). “A proof of uniqueness of surface waves that is independent of the Stroh Formalism”. In: *Mathematics and Mechanics of Solids* 9, 5–15.
- Mora, S. et al. (2011). “Surface instability of soft solids under strain”. In: *Soft Matter* 7, 10612.
- Murphy, J. (2013). “Transversely isotropic biological, soft tissue must be modelled using both anisotropic invariants”. In: *European Journal of Mechanics - A/Solids* 42, 90–96.

- Norris, A. and Shuvalov, A. (2010). “Wave impedance matrices for cylindrically anisotropic radially inhomogeneous elastic solids”. In: *The Quarterly Journal of Mechanics and Applied Mathematics* 63, 401–435.
- Norris, A., Shuvalov, A., and Kutsenko, a.a. (2013). “The matrix sign function for solving surface wave problems in homogeneous and laterally periodic elastic half-spaces”. In: *Wave Motion* 50, 1239–1250.
- Ogden, R. W. (1997). *Nonlinear Elastic Deformations*. Dover New York.
- Pucci, E. and Saccomandi, G. (2014). “On the use of universal relations in the modeling of transversely isotropic materials”. In: *International Journal of Solids and Structures* 51, 377–380.
- Roccabianca, S., Gei, M., and Bigoni, D. (2010). “Plane strain bifurcations of elastic layered structures subject to finite bending: theory versus experiments”. In: *IMA journal of applied mathematics* 75, 525–548.
- Spencer, A. (1984). *Constitutive theory for strongly anisotropic solids*. Springer-Verlag.
- Stafford, C. M. et al. (2004). “A buckling-based metrology for measuring the elastic moduli of polymeric thin films.” In: *Nature materials* 3, 545–50.
- Stolz, C. (2010). *Milieux Continus en Transformations Finies*. Palaiseau: Editions de l’Ecole Polytechnique.
- Ting, T. C. T. (1996). *Anisotropic elasticity: theory and Applications*. Press, Oxford University.
- Van Looche, M., Lyons, C., and Simms, C. (2006). “A validated model of passive muscle in compression”. In: *Journal of Biomechanics* 39, 2999–3009.
- Walton, J. R. and Wilber, J. P. (2003). “Sufficient conditions for strong ellipticity for a class of anisotropic materials”. In: *International Journal of Non-Linear Mechanics* 38, 441–455.

Conclusion

The chapters collected in this thesis raise many interesting questions. Chapter 1 predicts a new phenomenon: oblique wrinkles, which should appear in a large range of materials. Yet oblique wrinkles have not been seen experimentally so far on soft solids. Another issue raised was why are the predicted critical strains greater than the experimentally observed critical strains? We showed that this is likely due to a skin effect caused by dehydration (Steigmann and Ogden 1999).

In Chapter 2 the effects of a stiffer skin on an elastic substrate on surface wrinkles was initially studied, and therein we also studied the possibility of using surface wrinkles to characterise fibre reinforced materials.

The results from Chapter 3 show that measuring the propagation speed of surface waves only along the principal directions of deformation leads to many challenges in non-destructive evaluation of strain and stress, because these directions are not necessarily aligned with the directions of fastest and slowest propagation. However, the methods for calculating surface waves along any direction presented in that chapter are now sufficiently mature and robust to be able to use the full Rayleigh wave-field in order to characterise solids. There are now experiments in place that measure surface waves on tissue (Li et al. 2012b, Zhang and Greenleaf 2007), and a wide range of techniques to infer the surface elastic properties from these measurements for a range of materials (Every 2002). Yet, to date, surface wave measurements have not been adequately linked to the elastic properties of soft tissue, such as the residual stress or the reinforcing fibre properties.

Chapter 4 shows a surprisingly simple relationship between the angle of the surface wrinkle wave-front and the fibre orientation, a trend which becomes stronger the stiffer the fibres. Yet predicting how these wrinkles appear on soft fibre reinforced solids required a highly technical and involved numerical method. A promising alternative model is that of a soft tissue reinforced by fibres idealized to be infinitely stronger than the surrounding soft matrix. In that case, a constrained Stroh formulation for pre-stressed elastic material (Edmondson and Fu 2009) would provide an ideal framework.

Perhaps the most interesting feature of both incremental surface waves and static wrinkles is that they exhibit such a diverse range of behaviour. This diversity is due to the underlying anisotropy of the substrate. An exciting technological application would be to tune these soft solids to produce specific properties for the surface waves and wrinkles. For instance surface wrinkles are induced to develop functional coatings, such as diffractors or substrates for cellular growth (Li et al. 2012a). When generating elastic waves these materials are often called *acoustic*

metamaterials, which have many advantages over optical metamaterials. For instance, the combination of strong contrast and weak energy dissipation is easily achieved in acoustics and elastodynamics (Craster and Guenneau 2012). It is even theoretically possible to design materials that acoustically cloak objects embedded within them (Norris et al. 2014, Parnell and Shearer 2013).

Finally, we should not forget that all physical fields can interact with each other. Tuning an acoustic wave to interact with other waves can have amazing applications, such as producing an optical diode that allows light to pass in only one direction (Hafezi and Rabl 2012). Optical diodes are vital components to build optical processors. Hafezi and Rabl (2012) have tuned a membrane that generates acoustic waves when light passes through it. The interference between the acoustic waves and light is what breaks the symmetry and allows light to travel in only one direction. Another recent example is to use Brillouin scattering to control the group speed of light and even block the passage of light (Kim et al. 2015)

References

- Craster, R. V. and Guenneau, S. (2012). *Acoustic Metamaterials: Negative Refraction, Imaging, Lensing and Cloaking*. Vol. 166. Springer Science & Business Media.
- Edmondson, R. and Fu, Y. (2009). “Stroh formulation for a generally constrained and pre-stressed elastic material”. In: *International Journal of Non-Linear Mechanics* 44, 530–537.
- Every, A. (2002). “Measurement of the near-surface elastic properties of solids and thin supported films”. In: *Measurement Science and Technology* 13, R21.
- Hafezi, M. and Rabl, P. (2012). “Optomechanically induced non-reciprocity in microring resonators”. In: *Optics express* 20, 7672–7684.
- Kim, J. et al. (2015). “Non-reciprocal Brillouin scattering induced transparency”. In: *Nature Physics* 11, 275–280.
- Li, B. et al. (2012a). “Mechanics of morphological instabilities and surface wrinkling in soft materials: a review”. In: *Soft Matter* 8, 5728–5745.
- Li, C. et al. (2012b). “Determining elastic properties of skin by measuring surface waves from an impulse mechanical stimulus using phase-sensitive optical coherence tomography”. In: *Journal of The Royal Society Interface* 9, 831–841.
- Norris, A. N., Amirkulova, F. A., and Parnell, W. J. (2014). “Active elastodynamic cloaking”. In: *Mathematics and Mechanics of Solids* 19, 603–625.
- Parnell, W. J. and Shearer, T. (2013). “Antiplane elastic wave cloaking using metamaterials, homogenization and hyperelasticity”. In: *Wave Motion* 50, 1140–1152.
- Steigmann, D. and Ogden, R. (1999). “Elastic surface—substrate interactions”. In: *Proceedings of the Royal Society of London A: Mathematical, Physical and Engineering Sciences* 455, 437–474.
- Zhang, X. and Greenleaf, J. F. (2007). “Estimation of tissue’s elasticity with surface wave speed”. In: *The Journal of the Acoustical Society of America* 122, 2522–2525.